Erosion and Dilation of Edges in Dimensional X-ray Computed Tomography Images

By

Nathanael Turner

Doctoral Thesis

Submitted in partial fulfilment of the requirements for the award of Doctor of Engineering of Loughborough University

2020

Abstract

Dimensional X-ray Computed Tomography (CT) is a rapidly expanding field of research due to the numerous advantages this technique offers over conventional measurement technologies, most notably, the ability to measure internal features of a component. Tactile and optical Coordinate Measurement Machines (CMM), currently used in the manufacturing production industry, record points on the external surface of a workpiece by measuring the contact point of a physical probe or the reflection of projected light. X-ray CT has the ability to capture full volumetric data, since X-rays are transmitted through the entire object, revealing features which are otherwise invisible. Over the past five years, interest in this field has grown in the UK, with an increasing number of organisations in industry and research having access to X-ray CT machines and the wide range of manufacturers, offering new systems specifically designed for dimensional metrology applications.

Despite this, the complexity of data acquisition required for dimensional measurement using X-ray CT has made it difficult to estimate the measurement uncertainty. This has hindered the generation of standards and full-scale adoption of this technique in industry. Due to the nature of X-ray imaging, a number of non-linear influence factors exist which have the potential to cause dimensional measurement error. These influences must be better understood to reduce and ideally, compensate error.

In this doctoral thesis, the effects of the influence factors associated with CT data acquisition are studied, specifically, beam hardening and a finite X-ray source size. The effects these have on the quality of X-ray CT data are well understood; typically degrading the achievable contrast and spatial resolution of the CT image. However, the effects on dimensional measurement are less well understood due to the complexity of their interactions before reconstruction of the final image. These influences are modelled in a simulated CT acquisition to quantify any systematic effects on determination of edges in the CT image. The results are then validated by experimentally replicating the simulation set-up.

In this work, it is found that beam hardening and a finite source diameter can lead to systematic errors in the edge position within the CT image. Beam hardening generally leads to dilation of the edge; where the edge position moves in the direction of the surface vector. In contrast, a finite source diameter can lead to erosion of the edge; where the edge position moves in an opposing direction to the surface vector.

Preface

This thesis has been prepared as one of the requirements of the Engineering Doctorate degree with Loughborough University. This thesis was sponsored and part funded by the Manufacturing Technology Centre (MTC) based in Coventry, UK. This work was carried out from October 2013 to October 2018 under academic supervision from Professor Jeremy Coupland (Loughborough University) and industrial supervision from Dr Katy Milne (2013 - 2016) and Dr Nick Brierley (2016-2018). The vast majority of the work performed for this thesis was done at the MTC site in Ansty Park which houses two Nikon X-TEK micro-focus X-ray CT systems.

The scope of this research relates to commercially available, high energy, micro-focus, industrial X-ray CT systems. These systems typically operate in the range of 100 kV – 450 kV and achieve vendor specified source diameters in the range of 1 µm – 100 µm. This work will therefore focus on single material component applications with material densities ranging from plastics to Nickel and Iron based metal alloys and dimensions ranging from 5 mm x 5 mm x 5 mm to 300 mm x 300 mm x 300 mm envelopes.

Acknowledgements

I would firstly like to thank my academic supervisor Professor Jeremy Coupland for all of his support and patience with this work. I would also like to thank Dr Katy Milne and Dr Nick Brierley for their support as well as Professor Ken Young for facilitating the EngD sponsorship at the MTC. I would also like to thanks Jonathan Settle, Shaun Smith and David Chater at the MTC for their support and flexibility when using the X-ray CT equipment and other colleagues at the MTC that have helped support me during this work.

I would like to acknowledge the National Physical Laboratory (NPL) for providing the hole-plate artefact that was studied in Chapter 4 and the supporting material that benefitted this work such as the reference measurements, CAD model and measurement template for use in Volume Graphics (VG) software where the measurements were performed. The author would also like to thank NPL for the use of their X-ray CT system, their advice and hospitality during this time.

Finally I would like to thank my friends and family for their continued support throughout my life, helping to make this journey worthwhile.

Contents

List of Acronyms

AM – Additive Manufacturing

ASTM – American Section of the International Association for Testing Materials

BHC – Beam Hardening Correction

BSI – British Standards Institute

CMM – Coordinate Measurement Machine

COR – Centre Of Rotation

CT – Computed Tomography

EM – Electromagnetic

FBP – Filtered Back Projection

FOP – Fibre Optic Plate

FOV – Field Of View

FPD – Flat Panel Detector

FST – Fourier Slice Theorem

FWHM – Full Width at Half Maximum

GD&T – Geometric Dimensioning and Tolerancing

ISO – International Organisation for Standards

IQI – Image Quality Indicator

LSF – Line Spread Function

MPE – Maximum Permissible Error

MTC – Manufacturing Technology Centre

MTF – Modulation Transfer Function

NDT – Non Destructive Testing

NPL – National Physical Laboratories

OTF – Optical Transfer Function

PSF – Point Spread Function

PHSF – Phase Shift Function

PTB – Physikalisch-Technische Bundesanstalt

ROI – Region of Interest

SNR – Signal-to-Noise Ratio

VIM - International Vocabulary of basic and general terms in Metrology

Chapter 1: Introduction

This chapter will introduce the subject of dimensional metrology in industrial manufacturing and discuss the current state-of-the-art and challenges faced by existing dimensional measurement technologies. X-ray CT is presented as a potential new technique in the field of dimensional metrology for addressing current challenges posed by novel manufacturing processes such as additive layer manufacturing. The most relevant benefits and limitations of X-ray CT are outlined and finally the research goals of this work are presented.

1.1 Industrial Drivers for Novel Inspection Technologies

Metrology is the scientific field of measurement and plays a crucial role in modern society; from highly accurate measurements in GPS devices to baking biscuits at the optimal temperature [1], metrology is concerned with definition and traceability of the international system of units (S.I. units), allowing measurements to be comparable around the world [2][3]. Dimensional metrology is associated with measurement of length, form and position and is crucial in high value manufacturing. Since the introduction of mass production and components with interchangeable parts, it has been a necessity for dimensional measurements to be made comparable [4]. In the manufacturing industry a number of instruments and techniques are employed to make dimensional measurements. Over time, measurement standards and technologies have had to adapt to the demands of production driven industries. In the past 50 years, the invention of tactile Coordinate Measurement Machines (CMM) has allowed rapid, computer-controlled inspection of components with sub-micrometre accuracy (as shown in Figure 1). These machines are programmed to probe the surface of the part, contacting the surface many times and recording the three-dimensional surface points. This ‘point cloud’ can then be used to fit the desired measurement features and verify dimensional conformance.

Figure 1. Example of commercially available Coordinate Measurement Machine; Leitz Infinity by Hexagon Manufacturing Intelligence [5]**.**

Since then however, inspection technologies have faced further challenges as new manufacturing processes have arisen. In recent years, additive manufacturing (AM), also referred to as 3D printing, has promised to revolutionize the way products are manufactured. This new technique has gained much interest in the aerospace and automotive industries as components can be designed with optimised weight, shape and strength with minimal wasted material [6]. It has therefore received major investment through government and industrial programmes [7] to improve these processes for full scale production. Furthermore, the worldwide market for AM is expected to continue to grow significantly over the next few years (Figure 2).

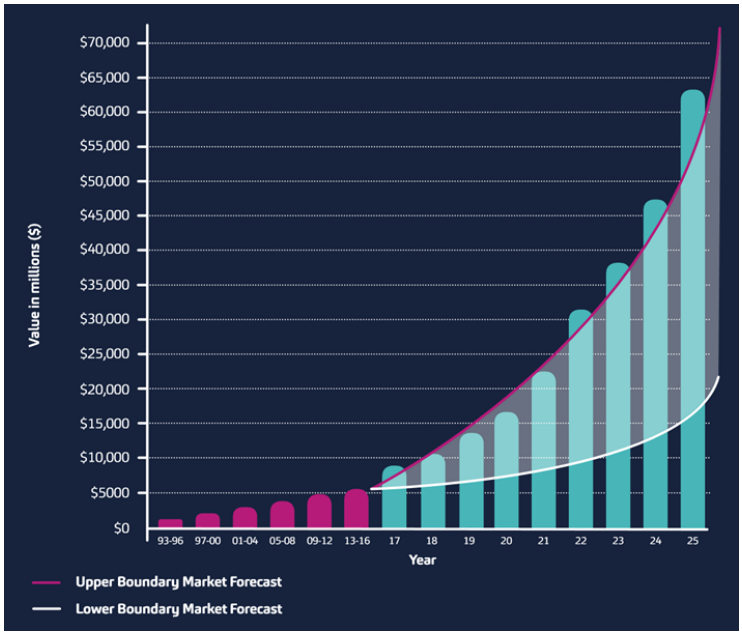

Figure 2. Forecasted growth in additive manufacturing global market until 2025. Image source: Additive Manufacturing UK [8]**.**

AM will create new challenges for component inspection; to validate dimensional conformance and part integrity. This is due to the unique ways in which components can be manufactured, allowing more complex geometries to be generated that would not be possible with other manufacturing techniques. Once built, the internal features often cannot be inspected by tactile or optical methods highlighting the need for novel inspection technologies. One of the technologies that is currently being employed for AM research is X-ray CT to check for defects such as pores, inclusions and trapped powder. This powerful technique can capture cross-sectional images through an object; revealing the interior structure. Since the component geometry can be obtained in this way, there exists the potential to apply X-ray CT for dimensional measurement purposes and it has therefore been widely endorsed as the next most disruptive technology in the field of metrology since the CMM.

1.2 Industrial X-ray Computed Tomography

Industrial X-ray CT is an imaging technique that can reconstruct a complete 3D model of an object's volume, as illustrated in Figure 3. The main components are an X-ray source, turntable and detector. Data is captured by rotating the workpiece, acquiring many X-ray images at varying angular views. X-ray images, or radiographs measure the absorption of the X-ray source which is mostly due to electron interaction within the

workpiece. These angular views or projection images are mathematically reconstructed into a digital voxel representation. The value (commonly referred to as a grey value) of each voxel represents the local relative X-ray absorption coefficient. A further step is then performed to define the edges of the workpiece in order to extract dimensional information from the data, this is known as the surface determination. There are many different modes and classifications of X-ray CT, however each follows these general principles. X-ray CT was initially invented for the purposes of medical imaging by Sir Godfrey Hounsfield [9]. It has since been used across a wide range of field for many applications [6]. Since the 1980's X-ray CT has been used in industrial Non-destructive Testing (NDT) for detection of inclusions/voids and defects in manufactured components.

Industrial X-ray CT has been cited as the most viable solution to overcome the inspection challenges brought by additively manufactured components [6]. X-ray CT has the ability to inspect internal or otherwise inaccessible features of a component and also shows promising potential as a metrology system [10]–[17]. Furthermore X-ray CT may be the only technique with the capability to inspect such components. Some of the key advantages of X-ray CT for metrology purposes are outlined below.

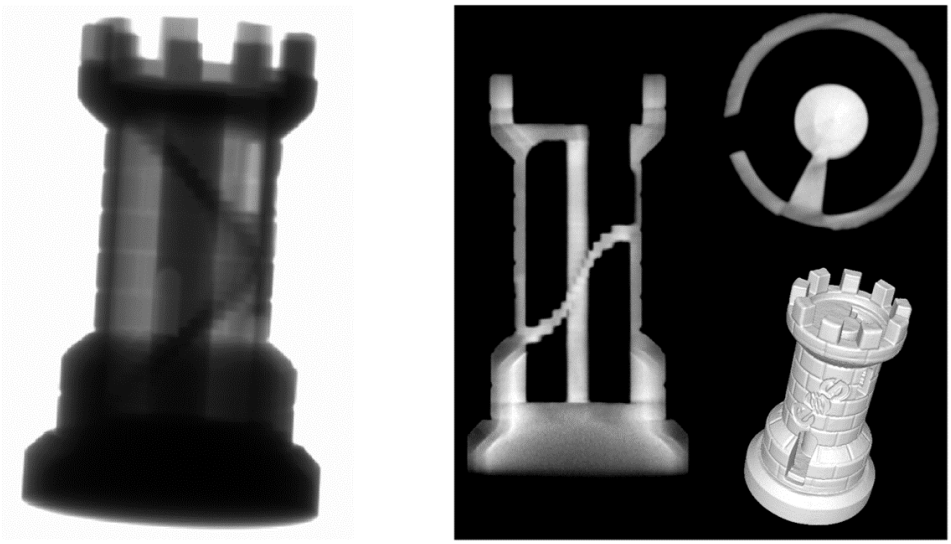

Figure 3. Left: 2D X-ray transmission image of ALM castle. Right: X-ray CT Images of 2D slices and 3D surface render. Image courtesy of the Manufacturing Technology Centre.

Short Wavelength Radiation

Industrial X-ray systems typically generate X-rays with wavelengths less than 0.1 nm (at >10 keV), which will be the approximate Abbe diffraction limit of the radiation. In other words the potential resolution of X-ray imaging is very high. Some commercially available systems claim CT data with spatial resolutions of down to 50 nm [18] although this is only achievable for samples of a few micrometres. For micro X-ray CT, achievable spatial resolutions will be of order a few hundred micrometres for objects that fit within a field of view in the order of 100 mm^3. Although the pixel size of these systems is limited, a geometric magnification of the X-ray image can be achieved using a divergent source, making the effective pixel size smaller than its physical dimensions. On the contrary, a magnification factor also reduces the effective field of view and requires a smaller source diameter size in order to maintain a sharp image. This is often the limiting factor in X-ray imaging.

Through Transmission

Since X-rays are transmitted through the entire object, information regarding the entire volume can be obtained as opposed to other techniques which only capture surface data. This is very advantageous for NDT but also for dimensional inspection as it allows interior or inaccessible features to be measured. Other NDT techniques such as Ultrasonic Testing (UT) may also be used for assessing a component internally however, the achievable resolution is vastly inferior to that of X-rays. This does however present a potential limitation of this technique as the component in question must be sufficiently penetrable to obtain useful data. High transmission requires higher energy X-rays to be generated which is more costly and can lead to other undesirable effects such as X-ray scatter.

Efficiency of Data Capture

One feature of X-ray CT is that it will capture data from the entire scan volume during a single scan, independent of the complexity of the workpiece geometry. Unlike tactile or optical CMM's where the scan time will usually be dependent on how complex the workpiece to be measured is. Therefore, the more features to be measured, the more

efficient it will be to use X-ray CT. One drawback of this is the large amount of data captured by X-ray CT inspection, this presents the challenge of big data storage and retrieval especially if such must be retained long-term for audit purposes such as in the aerospace sector.

Potential for Simultaneous Inspection

Another advantage of X-ray CT is that it could potentially be used to inspect dimensional conformance as well as the integrity of the workpiece, combining NDT & Metrology in a single process. This increases the value of performing dimensional measurement using X-ray CT as a check of integrity can be done simultaneously. X-ray CT has the potential for complete part qualification, including surface characterisation [19].

1.3 Limitations, Barriers and Solutions

Despite the numerous advantages of X-ray CT, there are still many limitations which prevent this technology being readily applied in industrial manufacturing. Some of the key limitations are discussed below.

Lack of International Standards

For tactile and optical CMM's, standards exist for performance verification (e.g. ISO 10360) and methods for following the GUM [20] for evaluation of task specific uncertainty. The ability to specify measurement uncertainty is crucial for providing a traceable route to the very definition of the meter. The only way for measurements around the world to agree is to have this unbroken measurement chain of traceability. This is of course critical in manufacturing as it is often the case that many different suppliers across many countries will contribute to the manufacture of final product from multiple components. Performance verification is a method that manufacturers and end-users can use to evaluate the measurement performance of the instrument in a universally accepted way. The measurement performance of a measurement system is typically given as a maximum permissible error (MPE) value for length measurement error or probing error, a graphical visualisation of this is shown in Figure 4. This evaluation characterises the measurement performance of a CMM within the entire measurement volume. The envelope of the MPE is usually dependent of the length of

the measurand and is therefore expressed in the form given in Figure 4. Verification tests are usually performed during the installation of the equipment and repeated periodically to ensure the instrument is still performing within the specified limits.

There are a number of general standards associated with X-ray CT and test methods for NDT, e.g. ISO 15708 [21], [22] or ASTM E1814 [23] however, X-ray CT for dimensional measurement is a relatively new field of research and therefore standardisation of best practice methods, performance verification and calibration have not yet been fully developed for use with this technique. Currently, manufacturers and users commonly refer to the series of German guidelines VDI/VDE 2630 [24]–[28]. These guidelines attempt to apply the ISO 10360 series of standards to 'CMMs with CT sensors'.

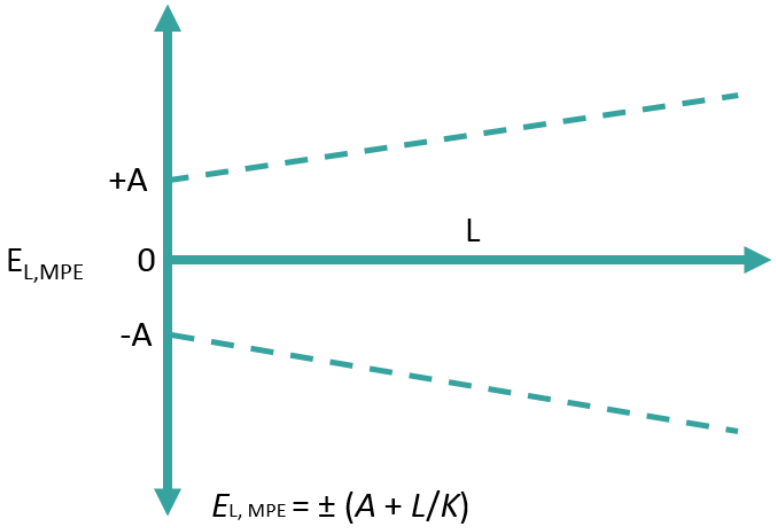

Figure 4. Schematic illustration of one possible representation of the Maximum Permissible Error (MPE) of length envelope where L is the measured size and A & K are dimensionless positive constants.

In 2002, the PTB (Physikalisch-Technische Bundesanstalt) in Germany developed a number of reference standards and procedures for improvements in measurement accuracy in X-ray CT [10]. There is currently an international draft guideline under development by the ISO TC 213 WG10, concerned with dimensional and geometrical product specification and verification of measurement equipment, with the intention to extend the ISO 10360 series to include CT measurement systems [29]. Verification tests such as the ISO 10360 do not consider the influence of single error components however and therefore only serve as a check that the measurement system is performing with

the specified range. For full traceability of measurements, the task specific uncertainty needs to be evaluated. In order to do this however, an uncertainty budget must be generated which quantifies the uncertainty components of each individual error source of which there are numerous.

Large Number of Influence Factors

To obtain dimensional measurements in X-ray CT, a number of steps have to be performed and at each stage, there are a number of influencing factors that potentially introduce systematic or random measurement error. Some of these factors are common to all measurement tasks e.g. thermal stability of the environment but most are specific to X-ray CT, e.g. scattering and therefore have an unknown influence on dimensional measurement. These influences will need to be better understood before measurement uncertainties can be calculated, which is vital to achieve traceability. A list of these potential influences have been developed and can be found in the VDI/VDE 2630 guideline part 1.2 [25]. Although the list is not exhaustive, it covers most of the components of the X-ray CT system. Some of the most important influence factors have been the subject of much research which is reviewed in detail in Chapter 3. More research into these influences is needed however to quantify the interaction of these factors with each other and the results of measurement. Many of these influences are due to instability and inaccuracy of the positioning and kinematics of industrial CT systems which initially weren't intended for the purposes of metrology.

Design Limitations

There are many applications for X-ray CT in industry [6], although some level of accuracy may be required for these tasks, most systems have not been designed for metrology therefore. In 2005 the first X-ray CT system designed for metrology was introduced [30] and a number of manufacturers have since produced their own versions of this. Designs have focussed on thermal stability of the enclosure, positional accuracy of the manipulator and stability of the source. Some examples of a dedicated X-ray CT metrology systems are given in Figure 5. Despite this development in X-ray CT hardware and software, it will still take time before standards are generated and complete control

over the measurement process can be obtained. Even with state-of-the-art systems, many limitations exist for dimensional measurement.

Figure 5. Example of a Metrology CT systems by a number of manufacturers. Clockwise from top left: Nanotom from GE [31]**, CT-Precision from YXLON** [32]**, Metrotom from Carl Zeiss** [33] **and MCT 225 from Nikon Metrology** [34]**.**

Physical Limitations

Although there are examples of the high resolutions that can be achieved with X-ray CT, the quality of data is workpiece specific and physical limitations exist to the size and or density of the workpiece that can be scanned. Generally speaking, the larger or more dense the workpiece, the harder it is to achieve high quality or resolution data. In order to justify the time and cost of using X-ray CT for inspection, the workpieces of interest are therefore high value or highly critical. As a result potential applications will often pose difficult geometries and materials for inspection which drives the need for systems with higher power, resolution and accuracy. There are however physical limitations to what can be achieved with these 'off-the-shelf' systems – often there is a trade-off between power and resolution or speed and quality. The main limiting factors that arise from the practical implementation of X-ray CT are highlighted in Chapter 2. The most relevant to this work are those associated with the X-ray source, namely the finite source size and broad energy spectrum.

1.4 Research Goals & Methodology

This chapter has outlined the needs, benefits and limitations of industrial X-ray CT for dimensional metrology. The main goal of this doctoral research is to identify gaps in the current understanding of this field of research and contribute to the existing knowledge.

This doctoral work was partly sponsored by the Manufacturing Technology Centre (MTC) and the majority of the work was carried out at the MTC using the state-of-the-art hardware available. The original aim of this project was to work with the NPL towards calibration of X-ray CT and the author was initially tasked with understanding and quantifying the influences factors associated with the X-ray acquisition workflow from generation of the X-ray beam, interactions with the workpiece and detection. It was soon found however that there were a large number of complex interactions associated with this workflow.

The first deliverable of this research was therefore to create a list of these influence factors and determine which of these had the greatest potential to contribute to dimensional measurement error. This was done mostly by conducting a literature review to gain an extensive understanding of the X-ray CT technique, the dimensional measurement workflow and the key process variables and influence factors. An initial experimental study was also performed on a calibrated reference artefact to quantify the measurement error observed simply by changing the orientation and position of the workpiece. This piece of work highlighted a number of systematic errors in the surface position that seemed to depend on the scan configuration of the artefact. It was hypothesised that these effects were due to a number of interdependent influence factors associated with the X-ray beam.

The second deliverable of this research was to better quantify the effect of these influences on dimensional measurements. This was done by simulating the acquisition of X-ray CT images and modelling these influence factors. By doing this it was possible to directly quantify the effect each influence had on measurement results.

The final piece of this work was to validate the effect of these influences experimentally by scanning a real workpiece and comparing the results to the predictions of the simulation.

The novelty of this work relates to the quantification of a number factors in X-ray computed tomography and their effect on dimensional measurements, namely, the X-ray source size, energy spectrum and the effective pixel or voxel size.

1.5 Structure of Thesis

A brief description of each of the remaining chapters of this thesis are given below:

Chapter 2 will give an overview of the fundamental principles of X-ray CT most relevant to the rest of this work. This chapter is split into three main sections; the first presents an introduction the theory of X-ray and radiographic imaging. The second focuses specifically on the mathematic foundation of tomographic imaging and also serves as an overview of the reconstruction methodology which is utilised in the simulation work found in the later chapters of this thesis. The third section describes some of the practical limitations of X-ray CT imaging and the influence these have on the final result.

Chapter 3 introduces the topic of dimensional X-ray CT, starting with a brief introduction of dimensional metrology. The typical workflow used to extract dimensional measurements from CT data is outlined and the main influence factors are discussed. Finally the current state of dimensional X-ray CT is reviewed, highlighting the biggest challenges in this field.

In Chapter 4, the initial experimental work is documented; a study performed using a calibrated hole-plate reference artefact. This artefact was scanned on a number of different X-ray CT systems under differing configurations. A number of systematic effects are observed which are seemingly related to the position and orientation of the hole-plate during the scan. Furthermore these effects are observed on all CT systems and are not compensated by the increased accuracy and stability of a metrology specific system.

In Chapter 5, the errors observed in the previous chapter are studied in more detail. The influences of the X-ray source due to the finite size and polychromatic energy range are modelled within a simulated X-ray CT acquisition. The systematic effects of these variables on the surface determination step are quantified for a simple workpiece. It is found that these X-ray source attributes can lead to both dilation and erosion of edges. The results of the simulation are also tested experimentally and are shown to be in good agreement. The results of the hole-plate experimentation are revisited and discussed in light of the new findings of this chapter. Potential correction methods for these X-ray source influences are discussed and finally the limitations of this thesis are highlighted and recommendations for future work are given.

Finally in Chapter 6, the key findings of each of the chapters are summarised and a number of key conclusions are drawn with an emphasis on the recommended further work that could be performed to expand on this thesis. The novel contributions of this work are outlined and the specific outcomes that have resulted from this work are discussed.

Chapter 2: Theory of X-ray and Tomographic Imaging

The aim of this chapter is to present the relevant theory and fundamental principles of X-ray imaging and tomography that is later used throughout the rest of this work. The final section of this chapter ties the theoretical model to the practical application of tomography, presenting the limitations and the influence of these on experimental results.

2.1 X-ray and Radiography

Since the discovery of X-rays in 1895 by Wilhelm Röntgen, they have been utilised extensively for a number of applications in scientific, industrial and medical fields. Probably the most popular use of X-ray radiation is for radiographic imaging due to the unique ability to see into otherwise opaque objects. Although the discovery of X-rays is credited mostly to Rontgen, there were earlier reports of strange phenomena from scientists who were experimenting with discharge tubes [35]. Rontgen was the first to systematically study their effects and produced some of the first X-ray images such as that of his wife's hand [36]. He is also credited with giving them the enigmatic prefix 'X' [37]. Since this time, research into X-ray radiation exploded and they quickly found their application in medical imaging [38]. Unfortunately the ionizing effects of this high energy radiation was not understood until much later which often resulted in skin burns, radiation sickness and even death [39]. Today, health and safety regulations employ stricter regulations in the presence of X-ray radiation, requiring X-ray sources to be sufficiently shielded to prevent overexposure of radiation [40]. This mandatory protection makes X-ray imaging more expensive and far less accessible than other imaging techniques and is one of the key disadvantages of radiographic techniques.

It is now understood that X-ray radiation is a form of light or electromagnetic (EM) radiation and are therefore characterised by their wavelength, frequency or energy. X-ray are often split into two categories; 'soft' X-ray in the energy range 100 eV – 10 keV and 'hard' X-ray in the energy range 10 keV – 100 keV. It should be noted that these characterisations are for convenience and the ranges are not well defined and typically overlap as shown in Figure 6 – in other words there is no physical difference between a soft or hard X-ray.

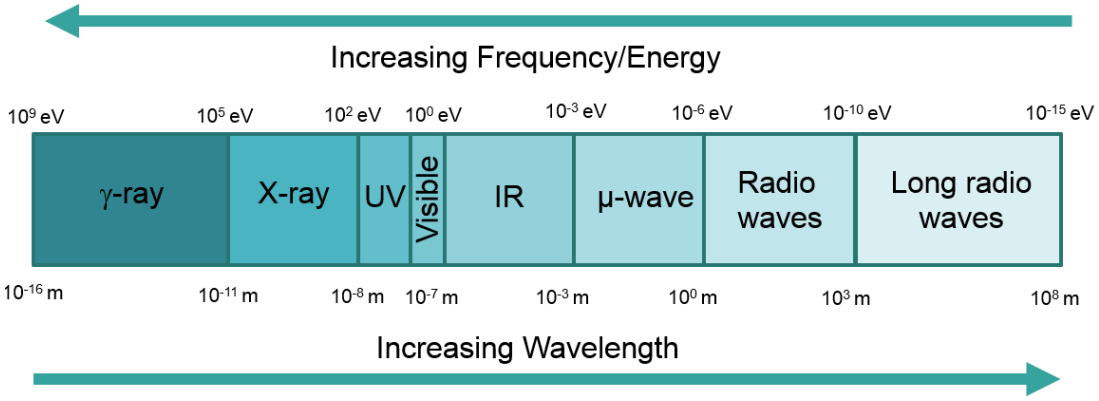

Figure 6. The electromagnetic (EM) spectrum of light which classifies the various wavelengths of light based mainly on the mainstream applications.

Some important properties of light are that it travels at a constant speed (in a homogeneous medium) equal to 299,792,458 ms^{-1} in a vacuum, light rays travel in straight lines and have no electric charge i.e. not deflected by the presence of a magnetic field. Light can interact however with matter in many different ways however, but generally speaking, the likelihood of any such interactions is inversely proportional to the wave energy. In other words the higher the energy of light the more transparent an object is to that particular wavelength. For light in the visible spectrum penetrating dense material such as metals, most of the light is attenuated at the surface. This is the reason most everyday objects appear solid to the naked eye. As the energy of the radiation increases, matter becomes more transparent and eventually a significant fraction of light will be transmitted as shown in Figure 7. By imaging with X-rays the internal features can be viewed with the clarity and detail akin to a conventional photograph. The practice of X-ray imaging relies on partial absorption of an X-ray source such that changes in intensity due to varying path length or a different absorbing medium are detectable.

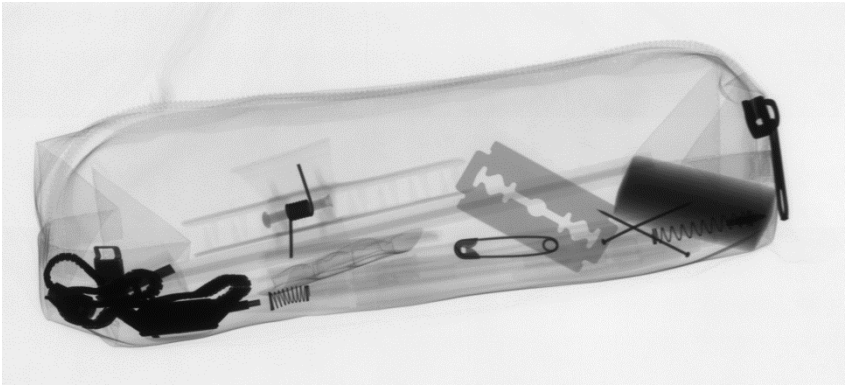

Figure 7. An example of a digital X-ray radiograph of items in baggage. Taken from [41]**.**

2.1.1 Generation of X-ray

The most common way of generating X-rays for imaging purposes are X-ray tubes [42] however linear accelerators and synchrotrons are also used [43]. The fundamental mechanism for generation of X-ray is through the acceleration of charged particles such as electrons [9]. The X-ray tube and linear accelerator achieve this in the same way; through bombardment of high energy electrons into a metal target. A synchrotron is a circular particle accelerator which uses magnetic fields to steer the direction of high speed electrons and therefore constantly changing the linear velocity. This results in the generation of "bremsstrahlung" radiation, the energy is dependent upon the circular velocity and radius of particle path. For industrial imaging purposes the most commercially available source types are based on the X-ray tube design. The reason for this is both practicality and cost; synchrotrons require a lot of specialist infrastructure and physical space. Linear accelerators on the other hand typically possess a larger source size than desired for high resolution applications.

The earliest X-ray tubes were Crooks tubes – although these were not originally designed for the generation of X-ray radiation, they were inadvertently produced as a side effect however, prompting their discovery. A partially evacuated glass chamber housed the components of this device as depicted in Figure 8. The creation of a potential difference between an anode and cathode and interactions of ionized gas molecules caused the liberation of so called cathode rays (electrons) from the surface which are subsequently accelerated towards the anode and mostly end up colliding into the glass walls of the tube – causing light at a range of energies to be emitted including that of X-ray radiation.

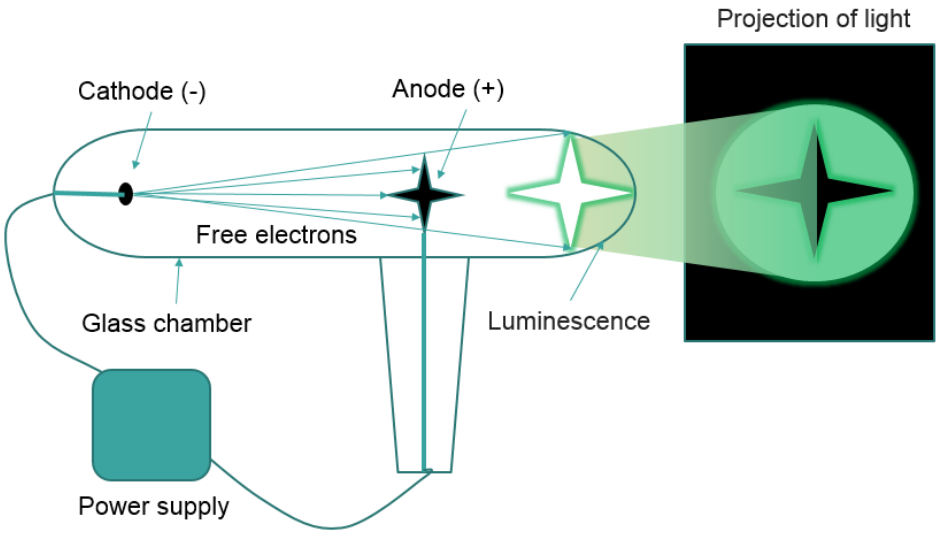

Figure 8. Demonstration of Crooks tube. Free electrons in the gas chamber are accelerated towards the anode, some of which reach the glass walls at the end of the tube and radiate visible light and X-rays.

The next generation of X-ray tube, sometimes referred to as the Coolidge tube, was designed for the purposes of X-ray generation and therefore produced the desired radiation more efficiently. Most modern X-ray tubes are now based on this design [9], shown in Figure 9.

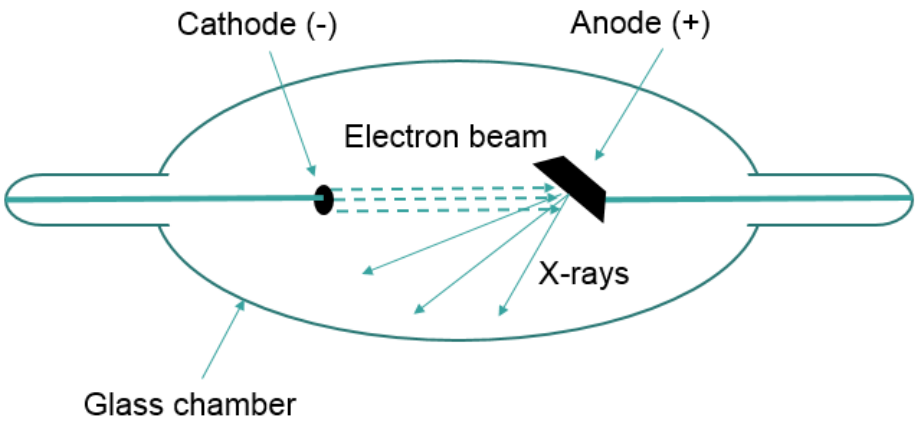

Figure 9. Schematic of the more recent Coolidge tube design. Electron are accelerated in a vacuum towards a metal anode, releasing X-rays radiation during rapid deceleration.

It includes a heated filament which more readily releases electrons in a process called thermionic emission, this omitted the need for any gases to be present in the tube, allowing electrons to travel more freely through the vacuum. The electrons were also

targeted at the anode rather than being allowed to interact with the walls of the vessel. Quickly this design began to encounter limitations due to significant heat generation as a result of the electron interaction with the target [9]. It is suggested that 99% of the kinetic energy of the electrons is converted to heat and less than 1% to X-ray radiation [17]. In order to combat this, target materials with a high melting point were used, e.g. tungsten and copper heat sinks were often added [9]. Later on, more advanced cooling methods were employed such as water cooling and rotating targets. Heat dissipation in the target still remains one of the biggest limiting factors when generating X-ray, especially for micro X-ray CT as these systems can focus the electron beam to only a few micrometres in diameter. Modern 'open' tube designs are also more common, this allows them to be opened and resealed for maintenance or replacement of the filament.

A typical X-ray tube spectrum is shown in Figure 10; X-rays are produced in these tubes via two main methods, namely characteristic and bremsstrahlung radiation.

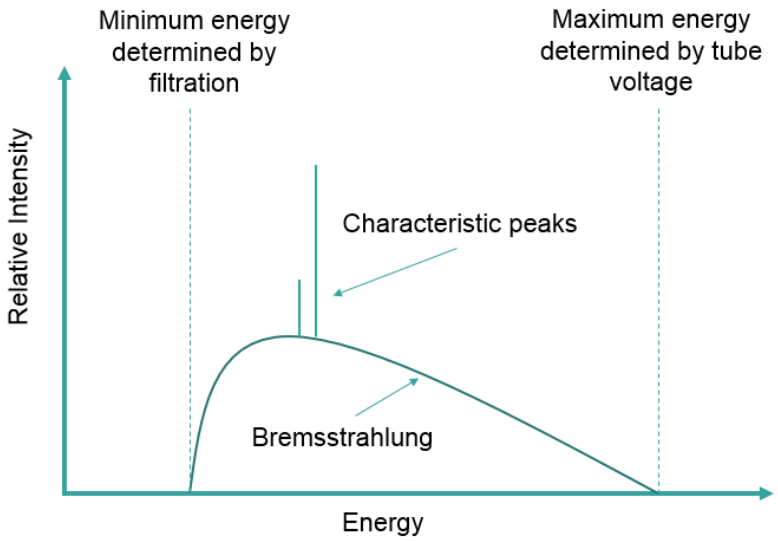

Figure 10.Schematic of a typical X-ray tube spectrum. The board underlying curve is produced via the bremsstrahlung mechanism and the sharp peaks are characteristic of the target material.

As electrons approach the target they begin to interact with the atoms within the material. The electrons can be deflected by the positive charge of the atomic nuclei or slowed by bound electrons, causing them to loose kinetic energy, and as a result emit Bremsstrahlung radiation. The characteristic X-ray are generated as bound electrons in the inner shells of atomic nuclei are ejected from their orbitals due to interaction with

the incoming electrons – as a result, outer shell electrons occupy the new states, releasing EM radiation of a specific wavelength, determined by the 'characteristic' energy states of the electron orbitals in question.

The characteristics of the X-ray radiation that is generated from these tubes depends on a number of physical factors, such as the target type, target material and filtration window material. Two main parameters are used to control the energy and intensity of the source, these are the acceleration voltage and the filament current. The effect of these two parameters on the source spectrum is illustrated in Figure 11. The current increases the intensity of the beam at all energies. The voltage controls the mean X-ray energy and the maximum energy of X-rays produced, it also increases the X-ray intensity over all energy ranges up to the maximum energy.

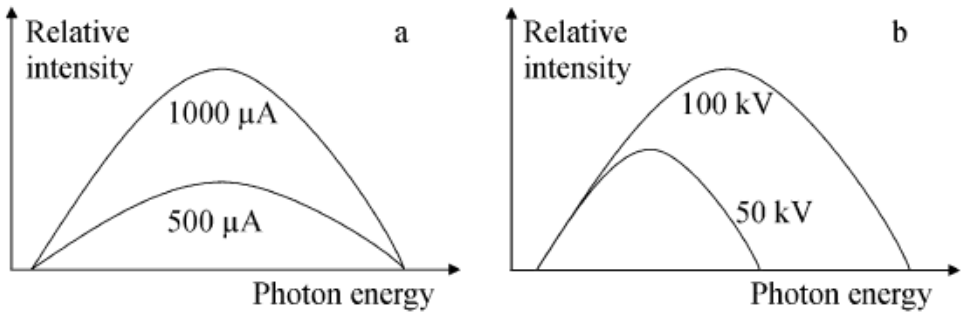

Figure 11. Effect of source current (a) and voltage (b) on energy spectrum. Taken from [17]**.**

2.1.2 X-ray interactions

X-rays can interact with atomic matter in a number of different ways, however, there are only three possible outcomes; either the X-ray photon is completely absorbed, scattered elastically or scattered inelastically. All three interactions are observed over the typical X-ray energies ranges used in industrial X-ray CT [44]. As previously mentioned the interaction cross-section is dependent on the energy of the radiation however there are a number of other factors which influence the likelihood of any such interaction occurring. Figure 12 demonstrates the relative occurrence of these interactions across the energy ranges achieved by common X-ray systems. Each of these interaction mechanisms is briefly explained below.

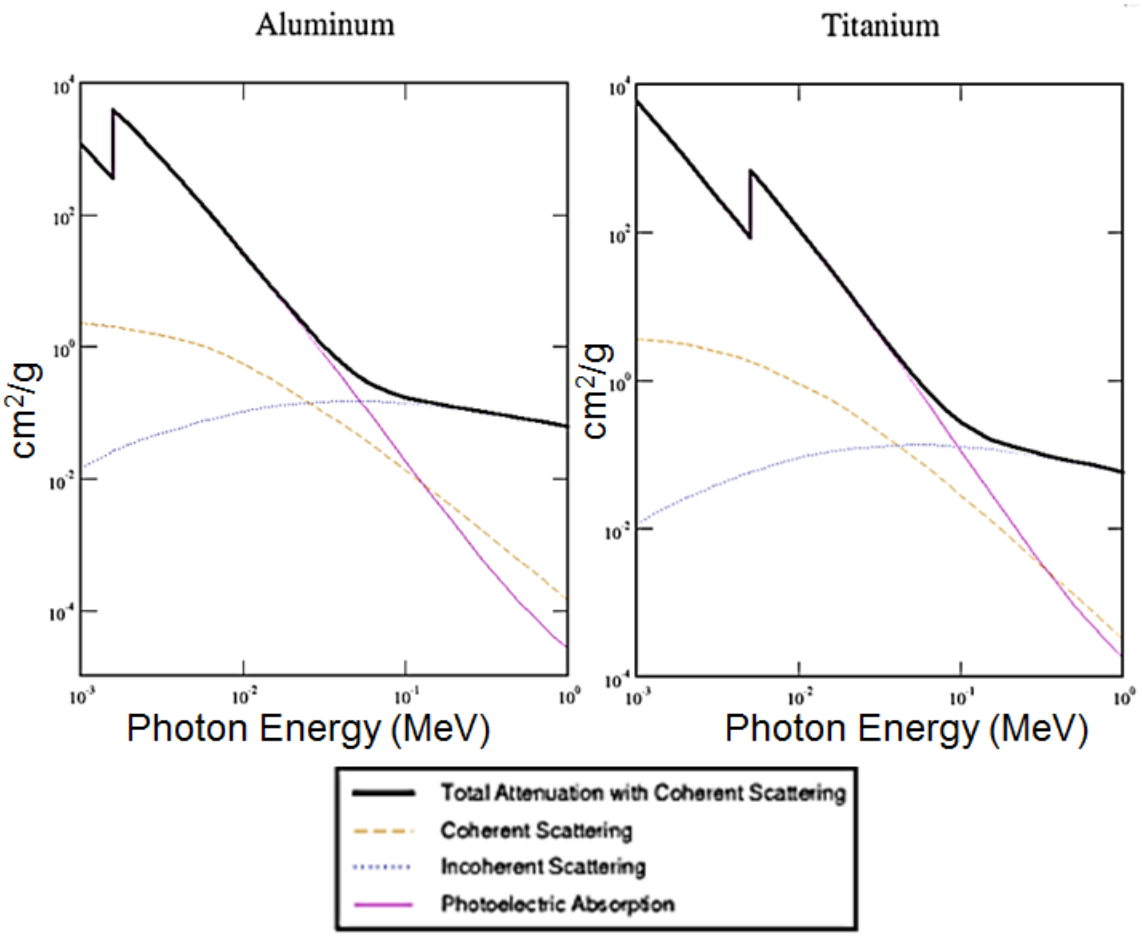

Figure 12. Comparison of X-ray attenuation due to the three most dominant processes; coherent scattering; incoherent scattering and photoelectric absorption for Aluminium and Titanium. Data from [45].

Photoelectric Absorption

Photoelectric absorption occurs when an incident photon is completely absorbed by a loosely bound electron. This occurs when the energy of the incoming photon exceeds the binding energy of the electron – liberating it from the atom, any remaining energy is converted into the kinetic energy of the electron. As the energy of the incident photon increases more tightly bound electrons can be ejected from the atom. Discontinuities in the interaction cross section are observed periodically, this is an indication that the incident photon energy equals that of a new energy orbital. Photoelectric absorption is most dominant at lower energies, up to about 100 keV. The overall interaction cross section has a decreasing trend however, as interaction become less likely the higher the X-ray energy.

Coherent Scatter

Scattering is the process by which light is deflected from its incident path through interaction with matter. Scatter can be split into two categories; coherent and incoherent. Coherent, also known as classical or elastic scattering, is observed when the wavelength of the scattered radiation is unchanged by the scattering process. The most dominant form of coherent scatter over the energy ranges of interest is Rayleigh scatter. This effect occurs as a result of the polarizability of atoms due to the positively charged nuclei and negatively charged electrons. Incident radiation will create an oscillating electric dipole which will emit scattered light of the same frequency with reduced intensity.

Incoherent Scatter

Incoherent scattering is observed when the wavelength of incident light differs from the scattered photons, incoherent scattering of light from free or quasi free electrons (electron binding energy is much less than photon energy) is known as Compton scatter. Compton scattering becomes more dominant than coherent scatter and photoelectric absorption at higher energies (Figure 12). The change in wavelength, $\Delta\lambda$, is related the scattering angle as in Equation 1.

$$\Delta\lambda = \frac{h}{m_e c}(1 - cos(\theta))$$

Equation 1

Where h is Planck's constant, c is the speed of light, m_e is the mass of the electron and θ is the scattering angle. The energy loss of the incident photon is transferred to the electron, in some cases it is enough to eject the electron from the atom as shown in Figure 13.

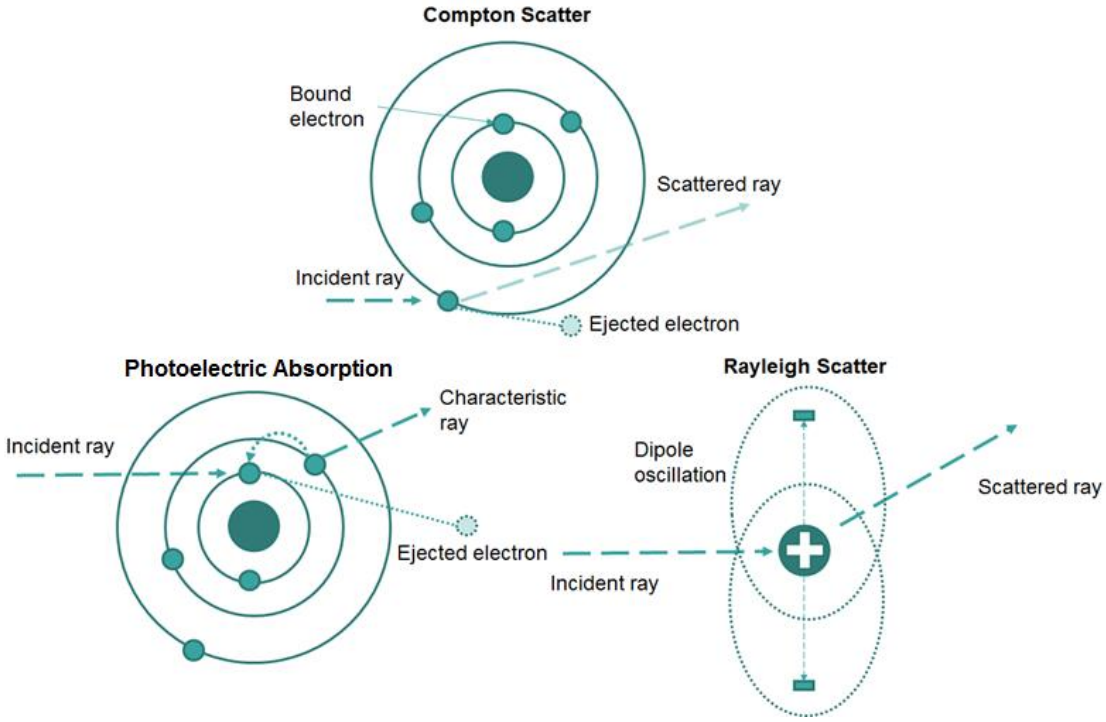

Figure 13. Schematic of dominant X-ray-matter interactions typically observed in industrial X-ray CT.

The Lambert-Beer law describes how the intensity of light decreases as it traverses through an absorbing medium. By considering the intensity, I, of a monochromatic light source before and after passing through a material of length x, Equation 2 can be derived as in [9].

$$I(x) = I_0 e^{-\mu x}$$

Equation 2

Where I_0 is the intensity of light at $x = 0$, and μ is known as the attenuation coefficient which describes the attenuation properties of the material. The total attenuation can be defined such that it is linearly proportional to the propagation length;

$$Attenuation = -ln(\frac{I(x)}{I_0}) = \mu x$$

Equation 3

This is a useful measurement as it is directly proportional to the thickness of the material, it should be noted that this relation is usually only valid for a monochromatic

light source and the energy dependence of μ should be considered for a polychromatic light source.

2.1.3 Detection of X-ray

Detection of X-ray is the final step for obtaining a radiographic image. The earliest ways of detecting X-ray was on photographic film which is still used widely today. A more recent method of detecting X-ray radiation is with a digital detector – there are three main types of digital detector; ionization, scintillation, semiconductor [46]. The most commonly used in industrial CT is the scintillator and Charge Coupled Device (CCD) and thus discussion about other types will be omitted from this work. The scintillator converts the incoming X-ray photons into light in the visible wavelength which can then be detected by the CCD. As such, this method is often cited as indirect detection, this is important as these detectors cannot resolve the energy of the detected photons. The CCD is used in most modern digital cameras which converts light into electrical charge which is then stored digitally. For the detection of X-ray above 10 keV with a CCD, a scintillator must be added to convert the incoming radiation into lower energy light that can be detected by the CCD. This process is illustrated in Figure 14.

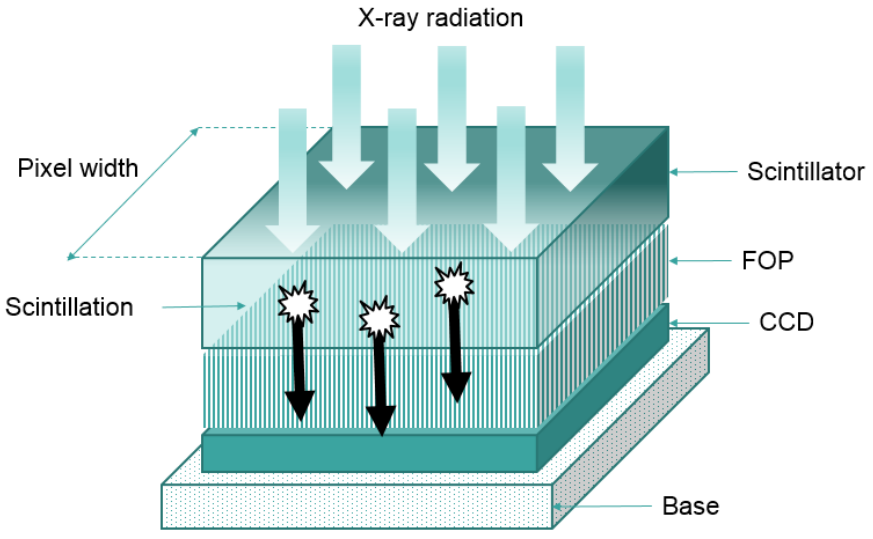

Figure 14. A schematic of the scintillator and CCD set up in a typical digital X-ray detector. The scintillator material converts the incoming X-ray radiation to light in the visible range, which is converted to an electronic signal through the CCD.

Typically a Fibre Optic Plate (FOP) is added which separates the scintillator from the CCD layer as this can influence the signal and also serves to protect the CCD which can be damaged over time due to exposure to the X-ray (as not all will be converted by the scintillator). The efficiency of the scintillator is dependent on the thickness of this layer, the material and the energy of incoming X-ray. Thicker scintillators tend to reduce the resolution however. More about the detector limitations is given in 2.3.4. Other options for recording X-ray data is to use a computed radiography which uses film plate that can be scanned by a laser and store the information digitally.

2.1.4 Key Principles of Radiography

The goal of radiography is to image the internal features of an object by propagating high energy radiation through it. By measuring the intensity of the source after it has been transmitted through the object of interest, differences in the absorption along the ray paths can be distinguished. However there are a number of factors that limit how effectively real features can be detailed. The main factors that are used to quantify the quality of a radiograph are the spatial resolution, contrast and noise.

Spatial Resolution

Spatial resolution is a measure of the resolving power of the image. It should not be confused with the pixel resolution of an image. The spatial resolution is usually parametrised by the Point Spread Function (PSF) which described how the imaging system responds to a point object, or the Modulation Transfer Function (MTF) which describes how the imaging system responds to spatial frequencies. The spatial resolution in radiography depends on a number of factors including the pixel or grain size of the projected image but it will also include the X-ray source size and the magnification factor of the image.

Contrast

The contrast is a measure of how well a feature can be distinguished from its background as shown in Figure 15. A number of factors will affect the image contrast, including the dynamic range of the detector, the energy of the X-ray source and the difference in X-

ray absorption between two features. The contrast of small features can also be affected by the spatial resolution as they approach the resolution limit.

Noise

An X-ray detector is essentially a counting machine and due to the random nature of the absorption and detection process, a large enough sample of X-ray needs to be detected before the information contained in the signal can be distinguished from the background noise, as such the intensity of the source and length of exposure time will directly influence the noise level. An example of this is shown in Figure 15.

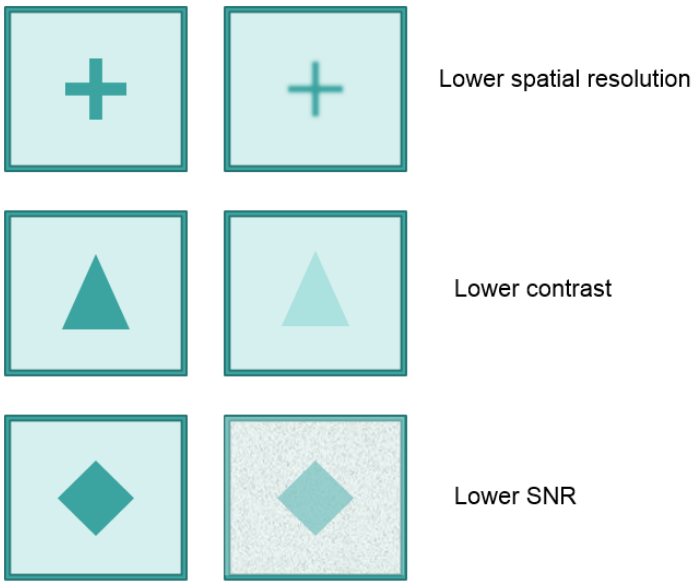

Figure 15. Schematic of image quality parameters, spatial resolution, contrast and noise. An example of the influence of these qualities on the resulting image is demonstrated.

Noise is inherent in any stochastic process but there are other influences that can increase the noise level such as scattering, detector fluctuations and detector efficiency. The signal-to-noise ratio (SNR) is typically used to quantify the noise level. To increase the SNR of the image, the exposure time can be increased.

2.2 Theory of Tomographic Imaging

The previous section has introduced the main principles of radiographic imaging and its wide range of uses. One of the biggest limitations of conventional radiography is that the depth information of the projected image is not preserved which can reduce the

effectiveness of this technique. This issue can partially be overcome simply by taking multiple images at different angular views as shown in Figure 16 revealing more depth information.

Figure 16. X-ray projections of baggage at multiple angles. Taken from [41]**.**

By taking multiple angular projections of an object and combining it with a reconstructive method, the complete 3D information of the object can be restored as shown in Figure 17. This is the basis of tomographic imaging which will be explained in detail in this section. To gain an understanding of the following, the author has mainly used the book on this subject matter by Kak and Slaney [47] reference should therefore be made to this material and others, [9], for a more rigorous derivation of the principles in this section.

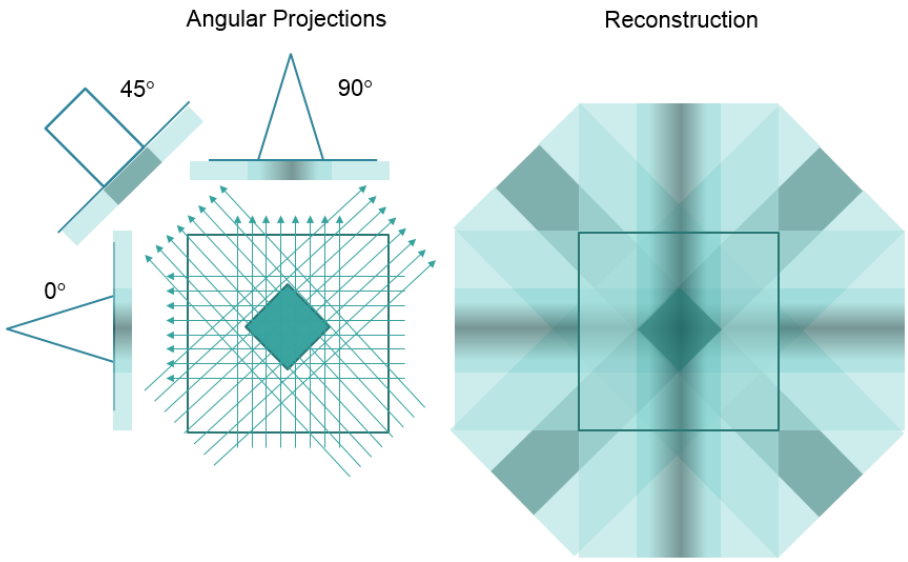

Figure 17. Illustration of back projection process. Each angular view is smeared across the image space, adding to the image.

2.2.1 Line Integrals

The concept of line integrals and projections are first introduced in this section. Tomography is the process of obtaining a cross-sectional image from its projection data. The projections of an image are the sum of image coefficients along linear paths through the image plane in a given direction specified by an angle which can be thought of as the viewing angle Figure 18.

The case of parallel ray projections will be presented first, followed by projections from fan beam rays. Mathematically these are represented by a set of line integrals parallel to s,

$$P_\theta(t) = \int \mu(x,y)ds$$

Equation 4

Where $P_\theta(t)$ is the value of the projection image at point t for the angle, θ.

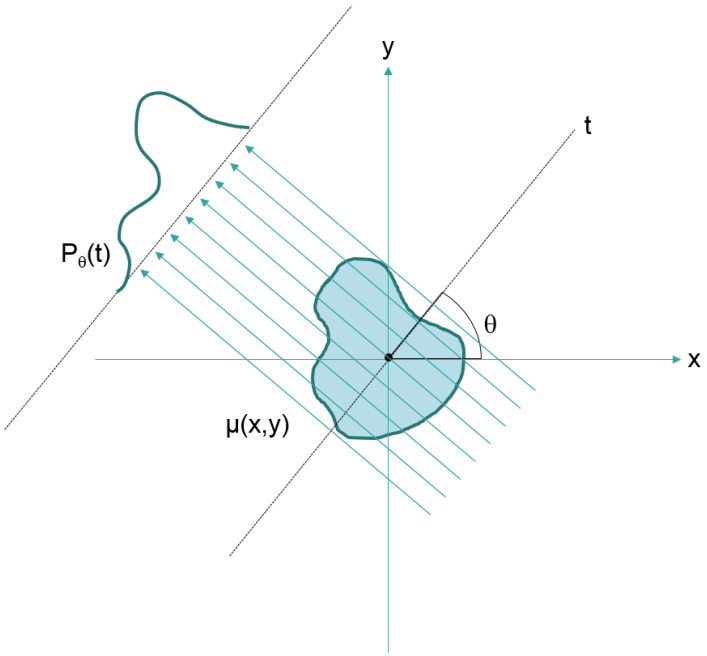

Figure 18. Parallel projection of image plane. Each ray that passes through the image is parallel to the next.

The value of the projection at each angle is then evaluated along the line, t, where,

$$t = xcos(\theta) + ysin(\theta)$$

Equation 5

Which is perpendicular to s, in that case it is clear that s and t are just the rotational transformation of the (x, y) coordinate system and therefore,

$$s = ycos(\theta) - xsin(\theta)$$

Equation 6

Which can be rewritten in terms of the image coordinates x, y:

$$P_\theta(t) = \int_{-\infty}^{\infty} \int_{-\infty}^{\infty} \mu(x,y)\delta(xcos(\theta) + ysin(\theta) - t)dxdy$$

Equation 7

This mathematic definition of the projection is known as the Radon transform, named after Johann Radon who first developed the mathematics used for tomography. As mentioned the goal is to reconstruct the image function from a set of projection images,

in the next section it is shown how this is possible through the Fourier Slice Theorem (FST), also known as the central or projection slice theorem.

2.2.2 The Fourier Slice Theorem

The Fourier slice theorem is the fundamental principle in Tomography as it provides the mathematical link between the projection images and the reconstructed image. In short the theorem states that the 1-dimensional Fourier transform of the projection image is equivalent a line in the 2-dimensional Fourier transform of the image function. To demonstrate this, the Fourier transform of a projection is first considered. The definition of the 1D Fourier transform of the projection image is,

$$S_\theta(\omega) = \int_{-\infty}^{\infty} P_\theta(t) e^{-i2\pi\omega t} dt$$

Equation 8

And, the definition of the 2D Fourier transform of the image function is,

$$F(u,v) = \int_{-\infty}^{\infty} \int_{-\infty}^{\infty} \mu(x,y) e^{-i2\pi(ux+vy)} dx\, dy$$

Equation 9

If we consider a projection at $\theta = 0$, it follows from Equation 7:

$$P_{\theta=0}(x) = \int_{-\infty}^{\infty} \mu(x,y) dy$$

Equation 10

And noting that at $\theta = 0$, $t = x$, from Equation 8,

$$S_{\theta=0}(\omega) = \int_{-\infty}^{\infty} P_{\theta=0}(x) e^{-i2\pi\omega x} dx$$

Equation 11

By substituting Equation 10, Equation 11 becomes,

$$S_{\theta=0}(\omega) = \int_{-\infty}^{\infty} \int_{-\infty}^{\infty} \mu(x,y) e^{-i2\pi\omega x} dx\, dy$$

Equation 12

By comparing Equation 12 with Equation 9 it is clear that this is equivalent to the 2D Fourier transform of the image function evaluated along the line $u = \omega$ and $v = 0$ is

$$F(\omega, 0) = \int_{-\infty}^{\infty} \int_{-\infty}^{\infty} \mu(x,y) e^{-i2\pi\omega x} dxdy = S_{\theta=0}(\omega)$$

Equation 13

More generally;

$$F(u = \omega cos(\theta), v = \omega sin(\theta)) = S_{\theta}(\omega)$$

Equation 14

Equation 14 is the basis of the Fourier Slice Theorem. Another implication of this is that each projection of the image plane corresponds to a radial line in the Fourier domain as shown in Figure 19. It is noted that the entire frequency space can be filled by taking only the projections in a 180° range.

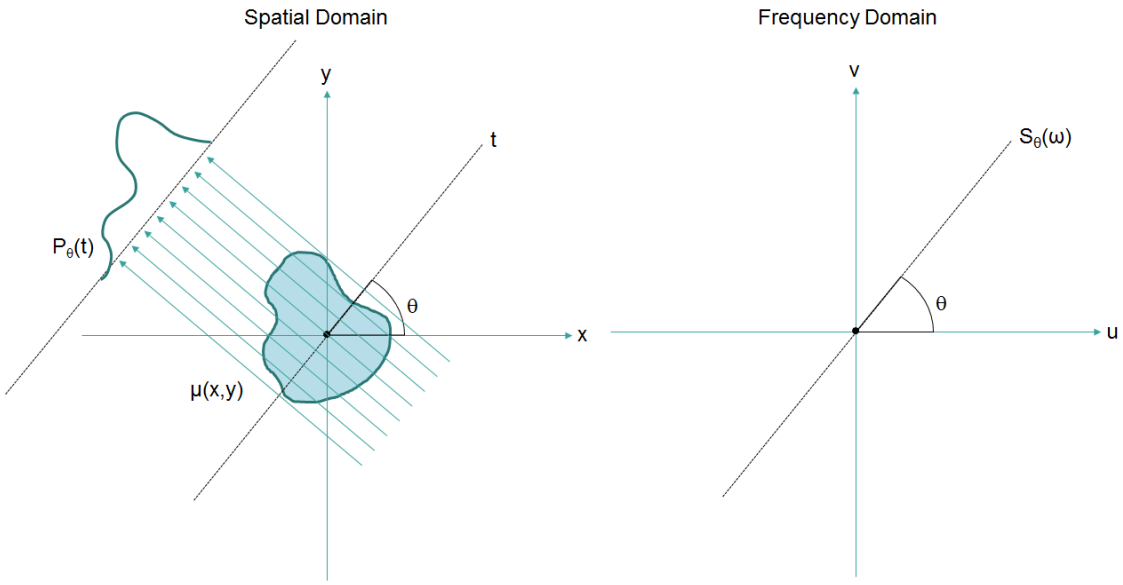

Figure 19. Spatial and frequency representations of a projection. Adapted from [47]**.**

2.2.3 Image Reconstruction

The Fourier Slice Theorem (FST) gives the mathematical relationship between the image projections and the image function through the Fourier transform. This section will demonstrate how the image function can be reconstructed from a finite set of projections.

Tomographic reconstruction can be split between analytical reconstruction, based on the FST, and iterative reconstruction methods such as the algebraic reconstruction technique (ART) which attempts to solve the full set of linear equations associated with the summation of the image attenuation co-efficient along each ray path. This section will focus on the filtered back projection algorithm as this is more commonly used in industrial X-ray CT due to the superior efficiency of this technique over others.

The task of reconstructing the image can be performed using a back projection algorithm, which involves 'smearing' each projection across the image plane at the corresponding angle, this process is repeated at every angle, summing each time. If this is performed for a set of 180 projections at 1° intervals, the reconstructed image is obtained as shown in Figure 20 b). This image is a rather blurred version of the original image (Figure 20 a)) and the reason for this is clear when considering Figure 21. As each projection only gives radial lines in the Fourier domain, if there is only a finite number of projections then missing data can be observed between each 'spoke', furthermore the sampling density decreases at higher frequencies, which explains why the image formed appears blurred. The 1D Fourier Transform of the projection image is performing a low pass filtering operation on the data and therefore higher frequency information is not preserved in the reconstruction.

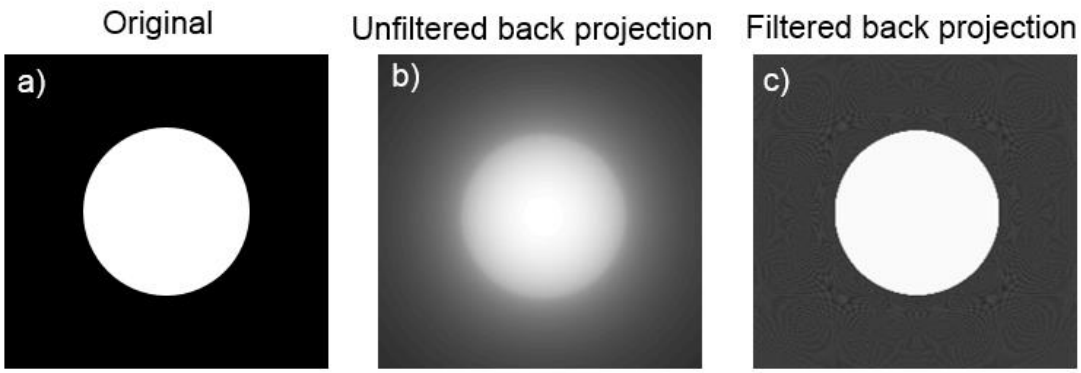

Figure 20. a) Original Image. b) Reconstructed image using unfiltered back projection. c) Reconstructed image using filtered back projection. Figures created in MATLAB ver. R2019a.

One way to combat this is to apply a weighted filter to the projection within Fourier space and then perform the usual back projection. This process is known as filtered back projection (FBP) reconstruction. This simple step can make a significant difference to the reconstructed image as shown in Figure 20 c).

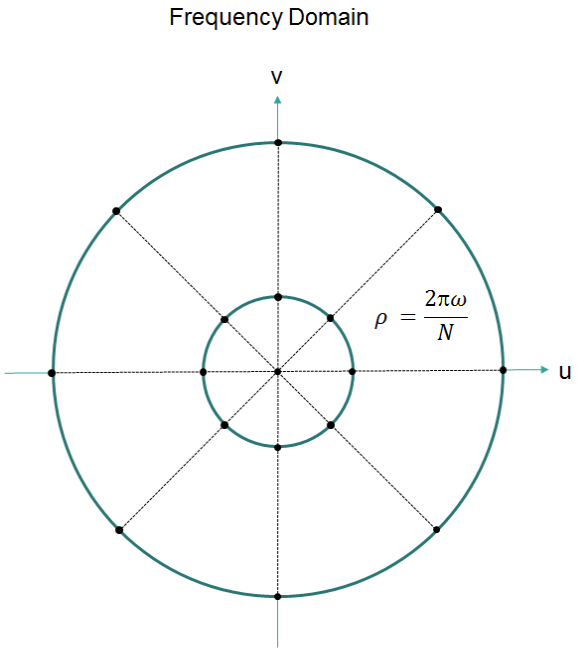

Figure 21. Fourier representation of each image projection. Adapted from [47]**.**

The number of samples per unit area depends on the absolute value of ω, and the spacing between projections, if projections are equally spaced and there are N projections over 360° then the angle between neighbouring projections is

$$d\theta = \frac{2\pi}{N}$$

Equation 15

And thus the width of the gap is

$$a = |\omega| d\theta = |\omega| \frac{2\pi}{N}$$

Equation 16

It is then possible to filter each projection by a ramp like filter in the frequency domain, shown in Figure 22.

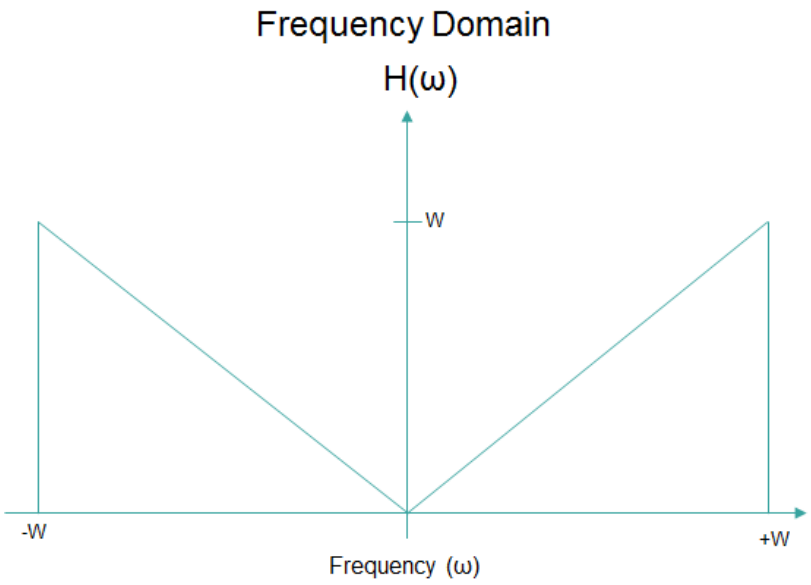

Figure 22. Ramp filter used in frequency domain to boost high frequency signals. Adapted from [47]**.**

From the Fourier slice theorem, the image function can be recovered using the 2D inverse Fourier transform:

$$\mu(x, y) = \int_{-\infty}^{\infty} \int_{-\infty}^{\infty} F(u, v) e^{i2\pi(ux+vy)} du dv$$

Equation 17

Changing to polar coordinates to obtain:

$$\mu(x,y) = \int_0^{2\pi} \int_0^{\infty} F(\omega,\theta) e^{i2\pi\omega(xcos(\theta)+ysin(\theta))} \omega \, d\omega \, d\theta$$

Equation 18

Which can be split to consider the range of 0° - 180° and 180° to 360° to obtain:

$$\mu(x,y) = \int_0^{\pi} \int_0^{\infty} F(\omega,\theta) e^{i2\pi\omega(xcos(\theta)+ysin(\theta))} \omega \, d\omega \, d\theta$$
$$+ \int_0^{\pi} \int_0^{\infty} F(\omega,\theta+180°) e^{i2\pi\omega(xcos(\theta+180°)+ysin(\theta+180°))} \omega \, d\omega \, d\theta$$

Equation 19

Using the fact that $F(\omega,\theta+180°) = F(-\omega,\theta)$ gives:

$$\mu(x,y) = \int_0^{\pi} \int_{-\infty}^{\infty} F(\omega,\theta)|\omega| e^{i2\pi\omega t} d\omega \, d\theta$$

Equation 20

And from Equation 14, substituting into Equation 20 gives:

$$\mu(x,y) = \int_0^{\pi} \int_{-\infty}^{\infty} S_\theta(\omega)|\omega| e^{i2\pi\omega t} d\omega \, d\theta$$

Equation 21

Equation 21 shows that the image function can be recovered by a filtered version of the 1D FT of the projections or;

$$\mu(x,y) = \int_0^{\pi} Q_\theta(xcos(\theta) + ysin(\theta)) d\theta$$

Equation 22

Where in Equation 22, Q_θ represents the filtered projection,

$$Q_\theta(t) = \int_{-\infty}^{\infty} S_\theta(\omega)|\omega| e^{i2\pi\omega t} d\omega = \int_{-\infty}^{\infty} P_\theta(t) h(xcos(\theta) + ysin(\theta) - t) dt$$

Equation 23

It should be noted that the value of $Q_\theta$is constant at each angle for a line t =$xcos(\theta) + ysin(\theta)$ in the image plane. Equation 23 shows that the filtering operation can be done in either the frequency or spatial domain – by performing the filtering in the spatial domain it turns out to be much more efficient than transforming the projections to the Fourier domain and back again – the filtered projections can then be back projected in the image space. Filtered back projection is the most common method of tomographic image reconstruction due to the improved computational efficiency over algebraic techniques [9].

2.2.4 Fan beam Sources

It has been shown how an approximation of the image function can be reconstructed from a set of parallel projection images using the filtered back projection method. As mentioned previously, the projections do not necessarily have to be formed from a set of parallel line integrals. This is useful as radiation sources naturally diverge and the assumption of parallel rays may only be made at large distances from the source. This section will demonstrate how this can be achieved for one of two cases of fan beam projections as shown in Figure 23, these are know either as equidistance or equiangular depending on the spacing between the rays.

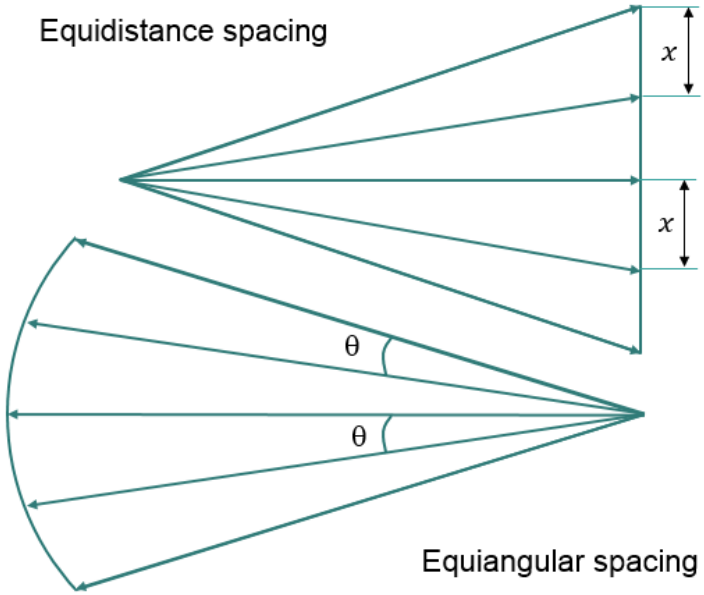

Figure 23. Two different fan beam configurations. For equidistance spacing the detector elements are spaced equally along a line. For equiangular spacing, detector elements are spaced at equal angles on an arc.

Equidistance Rays

In this case the detector elements form a straight line, perpendicular to the central ray as illustrated in Figure 24. Rays converge at the source point S, at a distance D from the rotation centre, O. The orientation of the central ray in the coordinate system is denoted by angle, β. Each ray corresponds to a detector element at a distance, d, from the central ray. The detector is imagined to be at the orientation of the coordinate system for convenience. An arbitrary ray is denoted along line SF at an angle γ to the central ray.

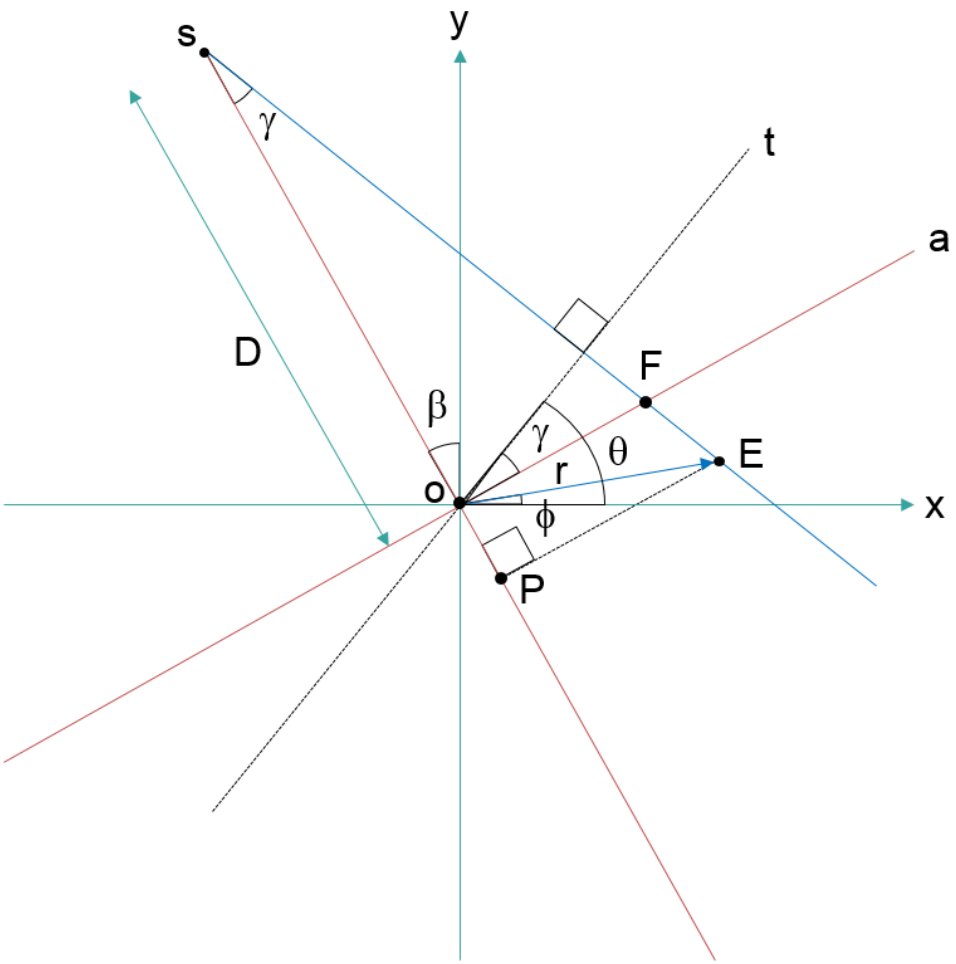

Figure 24. Outline of the fan beam coordinate system.

Starting with the expression for the image function in Equation 22 and Equation 23 and integrating over 2π radians to obtain,

$$\mu(x,y) = \frac{1}{2}\int_0^{2\pi} \int_{-\infty}^{\infty} P_\theta(t)h(xcos(\theta) + ysin(\theta) - t)dtd\theta$$

Equation 24

Any point in the image (x, y) can also be expressed in polar coordinates,(r, ϕ), as in Figure 24. Substituting in Equation 24 gives:

$$\mu(r,\phi) = \frac{1}{2}\int_0^{2\pi} \int_{-\infty}^{\infty} P_\theta(t)h(rcos(\theta - \phi) - t)dtd\theta$$

Equation 25

Equating t and θ from the parallel case to the fan beam parameters and Figure 24 gives Equation 26 to Equation 29:

$$\theta = \beta + \gamma$$

Equation 26

$$\theta = \beta + tan^{-1}\left(\frac{a}{D}\right)$$

Equation 27

$$t = acos(\gamma)$$

Equation 28

$$t = \frac{aD}{\sqrt{D^2 + a^2}}$$

Equation 29

Substituting these into Equation 25 to obtain,

$$\mu(r,\phi) = \frac{1}{2}\int_{-tan^{-1}(\frac{a}{D})}^{2\pi - tan^{-1}(\frac{a}{D})} \int_{-\frac{L}{2}}^{\frac{L}{2}} P_{\beta+\gamma}(\frac{aD}{\sqrt{D^2 + a^2}})h(rcos(\beta + tan^{-1}(\frac{a}{D}) - \phi) - \frac{aD}{\sqrt{D^2 + a}})\frac{D^3}{(D^2 + a)^{3/2}}dad\beta$$

Equation 30

Replacing $P_{\beta+\gamma}$ with $R_\beta(d)$ in Equation 30 gives,

$$\mu(r,\phi) = \frac{1}{2}\int_0^{2\pi} \int_{-\frac{L}{2}}^{\frac{L}{2}} R_\beta(a) h(rcos(\beta + tan^{-1}(\frac{a}{D}) - \phi) - \frac{aD}{\sqrt{D^2 + a^2}}) \frac{D^3}{(D^2 + a^2)^{3/2}} dad\beta$$

Equation 31

And writing the argument of h as:

$$rcos(\beta + tan^{-1}(\frac{a}{D}) - \phi) - \frac{aD}{\sqrt{D^2 + a^2}}$$
$$= rcos(\beta - \phi)\frac{D}{\sqrt{D^2 + a^2}} - (D + rsin(\beta - \phi))\frac{a}{\sqrt{D^2 + a^2}}$$

Equation 32

By using the identity:

$$cos(A + B) = cos(A)cos(B) - sin(A)sin(B)$$

Equation 33

And;

$$cos(tan^{-1}(A)) = \frac{1}{\sqrt{1 - A^2}}$$

Equation 34

And;

$$sin(tan^{-1}(A)) = \frac{A}{\sqrt{1 - A^2}}$$

Equation 35

U and s, are introduced such that Equation 32 can be expressed in terms of these two variables. U is the ratio of the distance $\overline{SP}$ to the distance D and s is the distance $\overline{OF}$.

$$U = \frac{\overline{SO} + \overline{OP}}{D} = \frac{D + rsin(\beta - \phi)}{D}$$

Equation 36

And by the triangular ratios it is clear that:

$$\frac{\overline{OF}}{\overline{SO}} = \frac{\overline{EP}}{\overline{SP}}$$

Equation 37

This gives:

$$s = D\frac{rcos(\beta - \phi)}{D + rsin(\beta - \phi)}$$

Equation 38

Which allows Equation 32 to be rewritten as:

$$\frac{sUD}{\sqrt{D^2 + a^2}} - \frac{aUD}{\sqrt{D^2 + a^2}} = (s - a)\frac{UD}{\sqrt{D^2 + a^2}}$$

Equation 39

Which can be substituted into Equation 31 to obtain:

$$\mu(r, \phi) = \frac{1}{2}\int_0^{2\pi} \int_{-\frac{L}{2}}^{\frac{L}{2}} R_\beta(a)h((s - a)\frac{UD}{\sqrt{D^2 + a^2}})\frac{D^3}{(D^2 + a^2)^{3/2}}dad\beta$$

Equation 40

From Equation 23 , $h(t)$ in the Fourier domain is expressed as:

$$h(t) = \int_{-\infty}^{\infty} |\omega| e^{2\pi i\omega t} d\omega$$

Equation 41

Therefore,

$$h[(s-a)\frac{UD}{\sqrt{D^2+a^2}}] = \int_{-\infty}^{\infty} |\,\omega| e^{2\pi i\omega(s-a)(\sqrt{D^2+a^2})} d\omega$$

Equation 42

Defining;

$$\omega' = \omega \frac{UD}{\sqrt{D^2+a^2}}$$

Equation 43

And substituting into Equation 42 to obtain:

$$h[(s-a)\frac{UD}{\sqrt{D^2+a^2}}] = \frac{D^2+a^2}{U^2D^2}\int_{-\infty}^{\infty} |\,\omega'| e^{2\pi i\omega'(s-a)} d\omega' = \frac{D^2+a^2}{U^2D^2} h(s-a)$$

Equation 44

And finally substituting this into Equation 40:

$$\mu(r,\phi) = \frac{1}{2}\int_0^{2\pi} \frac{1}{U^2}\int_{-\frac{L}{2}}^{\frac{L}{2}} R_\beta(a) h(s-a) \frac{D}{\sqrt{(D^2+a^2)}} da d\beta$$

Equation 45

Equation 45 can be simplified further to get:

$$\mu(r,\phi) = \int_0^{2\pi} \frac{1}{U^2} Q_\beta(a) d\beta$$

Equation 46

Where:

$$Q_\beta(a) = \frac{D}{\sqrt{D^2+a^2}} R_\beta(a) * \frac{1}{2} h(a)$$

Equation 47

This looks similar to Equation 22 for the case of parallel projections. The image function can therefore be reconstructed by back projecting the filtered projections along the

equidistant ray paths and weighting the projection by the factor of $\frac{1}{U^2}$. In Figure 25 it is shown how a single weighted fan projection looks like when back projected in this manner. This weighting accounts for the divergence of the ray paths. The task of fan beam reconstruction can be summarised as follows:

i. Modify each projection, $R_\beta(a)$, by factor: $\frac{D}{\sqrt{D^2+a^2}}$

ii. Convolve the modified projection, $R'_\beta(a)$, with $\frac{1}{2}h(a)$

iii. Weight each filtered projection by the factor $\frac{1}{U^2}$ and back project, summing for each angle of β.

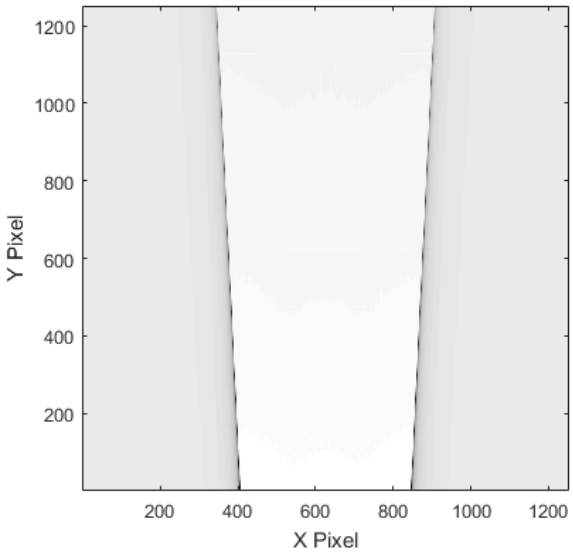

Figure 25. Weighted back projection of single fan beam projection. The weighting accounts for the divergence of the ray paths, which is not observed in parallel beam acquisition. Figure created in MATLAB ver. R2019a.

2.2.5 3D Reconstruction

The previous sections have covered filtered back projection (FBP) in 2D for the case of parallel and fan beam sources. FBP can be extended to 3D acquisition of data too, often named cone beam CT. The reconstruction algorithm is another step in the process chain where errors can be generated, leading to image artefacts. The most common artefact associated with the reconstruction algorithm are Feldkamp artefacts, named after the Feldkamp algorithm used for cone beam reconstruction [48]. This type of artefact is only observed in this mode and is due to incomplete data collection from circular cone beam

CT [49]. To acquire exact data the so called Tuy condition must be met which states that all planes that intersect a point in the reconstruction must also intersect the source trajectory [49], this is illustrated in Figure 26.

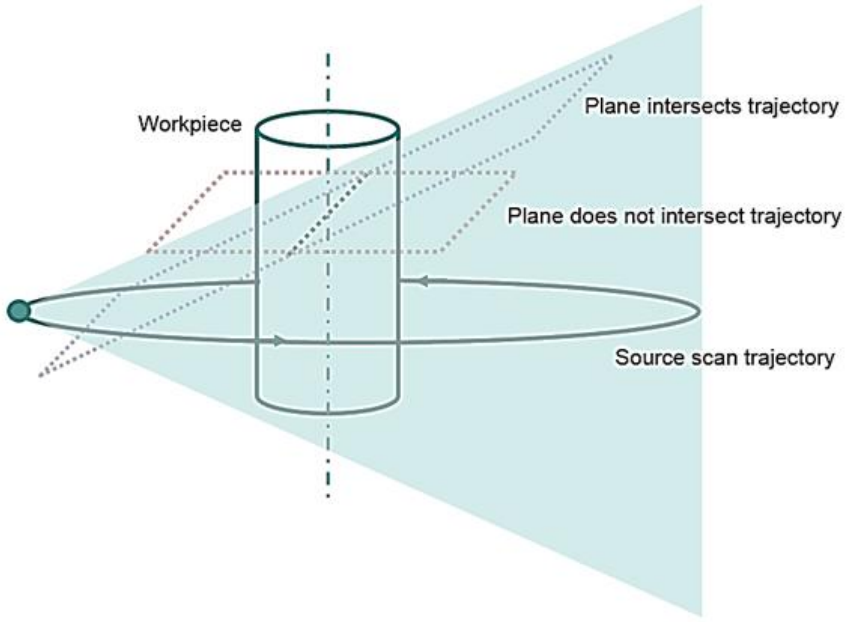

Figure 26. Schematic of source scan trajectory showing example of a plane that meets the Tuy condition and one that does not.

For a circular cone beam CT trajectory it is clear that only the central plane meets this condition and that this point moves further away from the central plane, more planes exist that do not meet the condition. This leads to a streaking effect which is more prominent at larger cone beam angles in the vertical direction as illustrated in Figure 27. There are many other trajectories that can be performed that ensure the Tuy condition is met for all points in the reconstruction, a common example is helical CT.

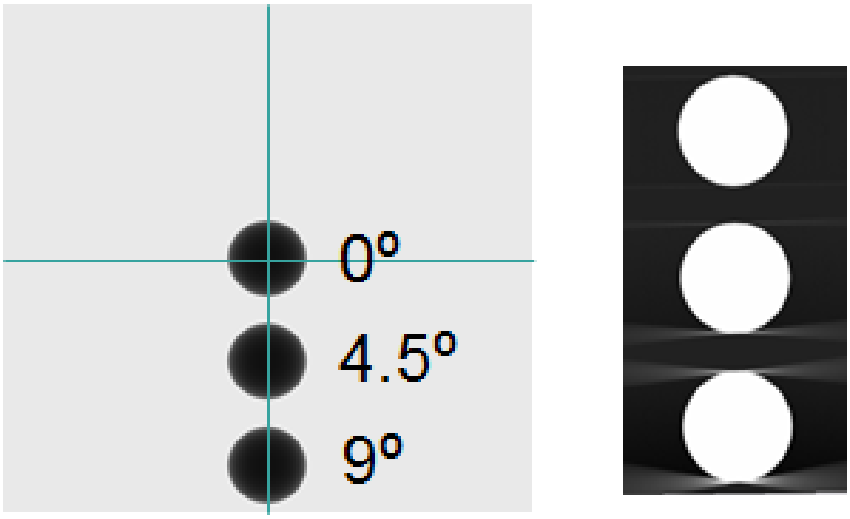

Figure 27. Example of Feldkamp artefacts in simulated CT data. Each sphere was placed at a different cone angle in the projection image, the greater the angle the harsher the artefacts.

2.3 X-ray CT in Practice

This section will explore how the mathematical theory of tomography is applied in practice. Ultimately it is not possible to perfectly reproduce the true values, in reality there are imperfections of experiment equipment, approximations, numerical error and influences beyond reasonable control. This section will show how the theory and practice deviate and what consequences this has on the results. The repeatable inconsistencies that are observed in the reconstructed data are often termed image artefacts, some of the most relevant of these are highlighted in this section.

In practice, radiographs measure the intensity of X-ray radiation or a measure of the power density which is related to both the number and energy of X-rays detected. It has been demonstrated that for tomography there is a need to integrate some function along the projected lines. In X-ray CT the function to be reconstructed is the attenuation coefficient, $\mu(x, y)$. The attenuation coefficient is a measure of the how strongly a material attenuates an X-ray source and is proportional to the mass density. Each element in the projection image will therefore be a line integral of this function giving the total attenuation along that ray path. To perform the reconstruction of this function there is therefore a need to first calculate the X-ray attenuation. This is an easy calculation in practice, using Equation 3 relating the X-ray intensity to the attenuation.

2.3.1 Modes of X-ray CT

X-ray CT typically consists of a source of X-ray radiation, an X-ray detector and a rotation stage to acquire different angular views of an object. There are a number of ways in which these components can be configured for different applications, for example in medical X-ray CT the patient remains stationary whilst the source and detector is moved around them. An explanation of the different modes of CT scanning most commonly used in industrial X-ray CT systems is presented below.

Fan Beam CT

Fan beam or 2D CT typically uses a linear detector, in either a flat or curved geometry as illustrated in Figure 28. The source is also collimated into a single plane. Each full rotation in fan beam CT corresponds to a single slice in the reconstruction, as such the workpiece undergoes many rotations with a vertical translation step in-between to move the next slice into the beam plane. This mode of scanning is therefore relatively inefficient but there are some key advantages that result from this. Firstly this mode effectively eliminates the scatter signal as any scattered photons will likely fall out of the beam plane (Figure 28). Secondly, this scanning mode will not be subject to 3D or Feldkamp artefacts as observed in cone beam CT.

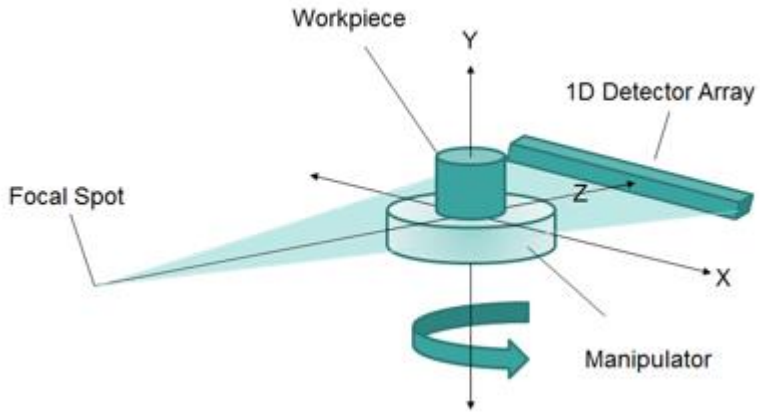

Figure 28. Schematic of the fan beam CT set up. Collimator plates are often used to create a single plane of X-rays that are detected using a linear or curvy linear array detector.

Cone Beam CT

Cone beam or 3D CT utilises an area detector to capture a 2D radiograph per angular view, as shown in Figure 29. A 3D volume can then be reconstructed after a single rotation of the workpiece. This mode of scanning is much more efficient than fan beam CT however, it is more prone to X-ray scatter and Feldkamp artefacts.

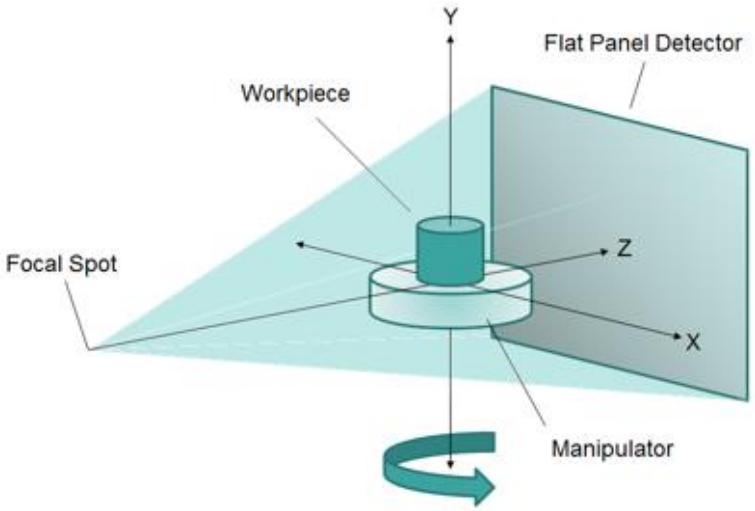

Figure 29. Schematic of the cone beam CT set up. A cone of X-ray radiation is produced and a flat panel detector used to record the resulting intensity images.

Other Scan Modes

More complex scan modes are also commonly used in industry to improve image quality or enable larger, more awkward objects to be scanned. Helical scanning is illustrated in Figure 30, this mode simultaneously rotates and translates the workpiece continuously. The main advantage of this is that Feldkamp artefacts can be eliminated, it also increases the effective size of the beam angle along the rotation axis. Scan times are typically longer however and high precision manipulation is required for accurately translating the workpiece during the scan.

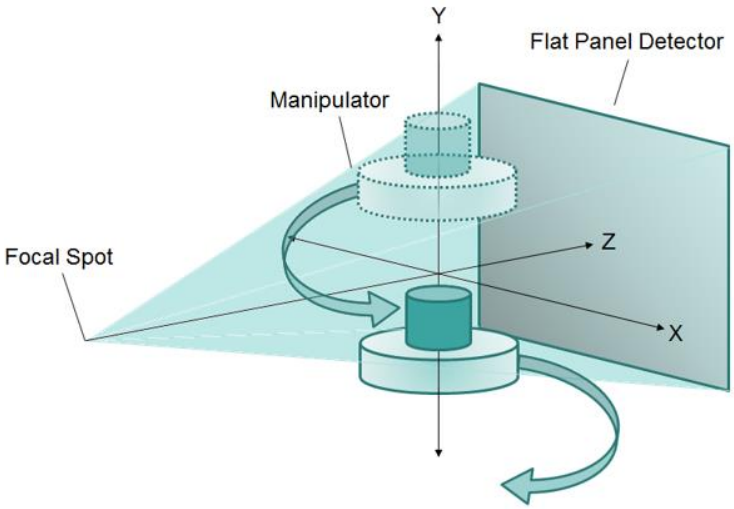

Figure 30. Schematic of the helical CT set up. This mode is similar to cone beam except that the workpiece is also translated parallel to the rotation axis during acquisition.

Region of interest (ROI) scanning can be used to increase the voxel resolution in a sub volume of the part as in Figure 31. Often the physical dimensions of the workpiece is a limiting factor when performing a CT scan; conventionally it must fit within the beam envelope at all angles. However a secondary scan may be performed at a higher magnification where a smaller ROI is scanned. These can be stitched together providing higher detail in key areas. This clearly increases the overall scan time and can introduce additional error when stitching the images.

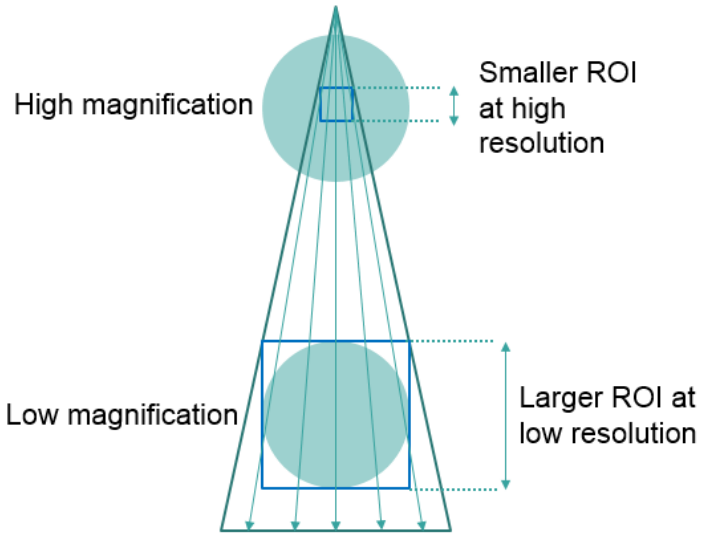

Figure 31. Illustration of ROI scanning. A higher resolution can be achieved in a small region of a large workpiece by allowing some of the object to fall out of the field of view.

2.3.2 X-ray Source

For the purposes of CT reconstruction it is assumed that the X-ray source is a monochromatic point source, however in practice the source spectrum consists of a wide range of energies and is generated over a finite area. These properties influence the quality of the reconstructed image, micro X-ray CT achieves source diameter sizes of less than 100 µm, allowing higher resolution images to be taken. Magnetic coils are used to focus the beam onto a very small area of the metal target as shown in Figure 32. Target materials usually require a very high melting point to withstand the heat generated by the bombardment of high energy electrons. This heat generation is even more crucial as the source diameter gets smaller as the power per unit area increases.

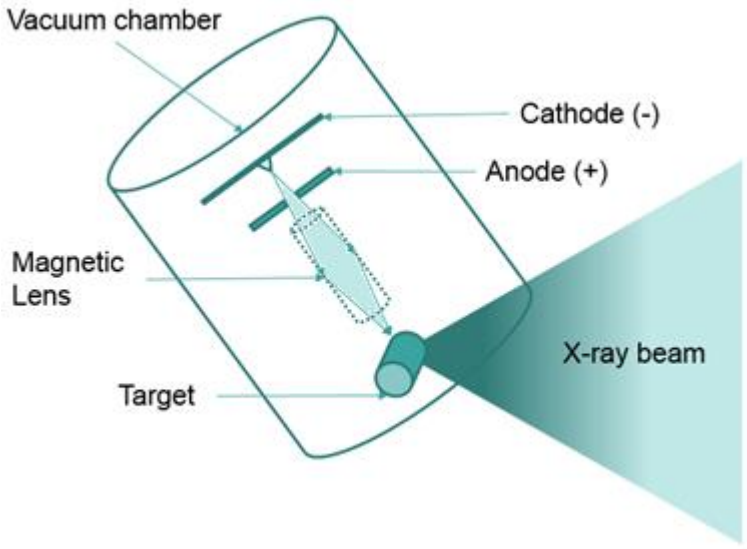

Figure 32. Schematic of micro X-ray CT reflection tube. A high energy electron beam is focussed with magnetic lenses towards the target material where X-rays are generated.

Finite Source Diameter

The source diameter is a measure of the largest width of the X-ray source. The smaller the source diameter, the sharper the radiographic images will be, as illustrated in Figure 33. The blur caused by the finite source is known as the penumbra, the size of this is also related to the relative distance of the imaged object to the source and detector, which can also be expressed in terms of the magnification factor. The source diameter can usually be inferred by measuring the resulting blur when imaging a sharp edge or resolution charts consisting of finely spaced line patterns. The source diameter will

influence the spatial resolution of X-ray CT images, the influence of this on dimensional measurements will be discussed in Chapter 5 in more detail.

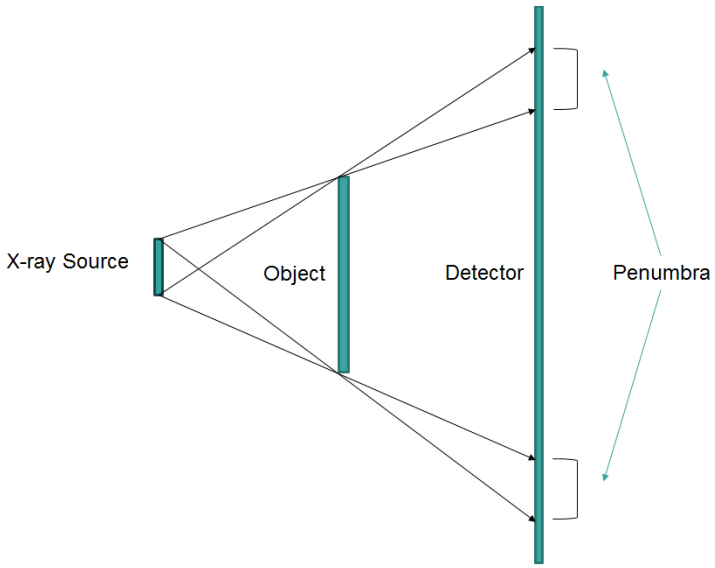

Figure 33. Demonstration of the effect of source diameter size on image sharpness. The size of the penumbra is proportional to the source size and the image magnification factor.

Polychromatic Spectrum

Another property of industrial X-ray CT tube sources is the wide band of X-ray energies that they generate. One consequence of this is the occurrence of a phenomena known as beam hardening. This effect describes the process of an increase in mean X-ray energy as the beam passes through a homogeneous material. The reason for this 'hardening' of the source is due to the energy dependency of the attenuation coefficient, μ, as plotted in Figure 34.

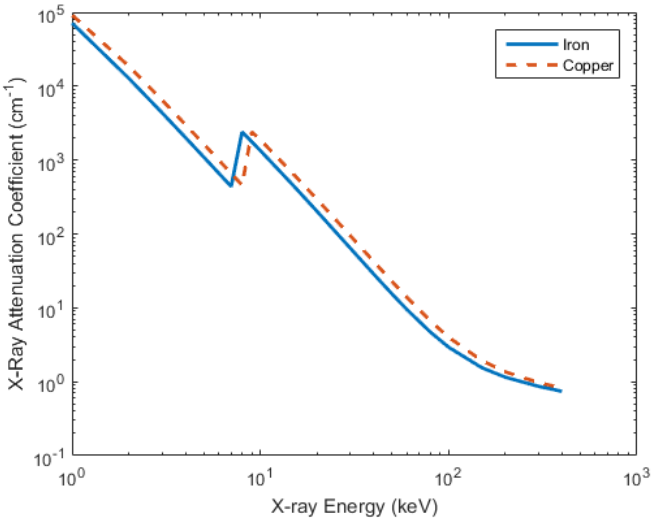

Figure 34. X-ray attenuation coefficient of iron and copper for X-ray energies from 1 keV to 400 keV. Data from [50]**. Figure created in MATLAB ver. R2019a.**

As a result, lower energy X-rays are attenuated more readily than those of a higher energy, causing the beam hardening effect [51]. The outcome of this effect on the reconstructed CT image is known as cupping, an example of this is shown in Figure 35.

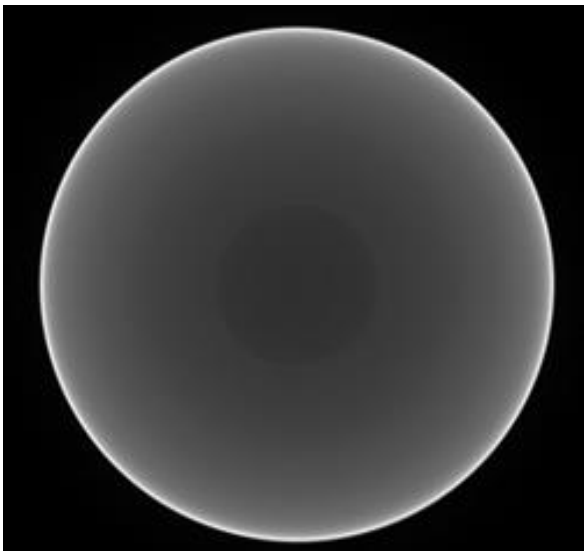

Figure 35. Example of a cupping artefact. Bright edges and reduced internal contrast is indicative of cupping, most often as a result of beam hardening.

The reconstructed grey-scale values at the edges of an object appear brighter, indicating a higher attenuation coefficient at that point. In reality the attenuation coefficient should be homogeneous but the beam hardening effect means the attenuation is much higher at the surface of the workpiece. Beam hardening is known to reduce the image

contrast making detection of features more difficult, Chapter 3 will discuss how beam hardening can lead to systematic measurement errors in dimensional X-ray CT.

2.3.3 Manipulating and Positioning of Workpiece

The manipulation system in an X-ray CT system is used to fixture the workpiece, position it within the beam and perform the necessary movements to capture the data during the acquisition process. High precision, of the order of a few micrometres is therefore required to place the workpiece at the correct orientation for each projection image. Inaccuracies in this system can lead to artefacts in the reconstructed image, some of the most common associated with the manipulation system are explained here.

Position of Rotation Axis

The position and orientation of the rotation axis is required for successful reconstruction of the projection data. Any deviations from the true position can lead to image artefacts such as those shown in Figure 36. Correction algorithms are usually built into the reconstruction software to reduce the influence of these artefacts. This can also occur due to misalignment of the detector.

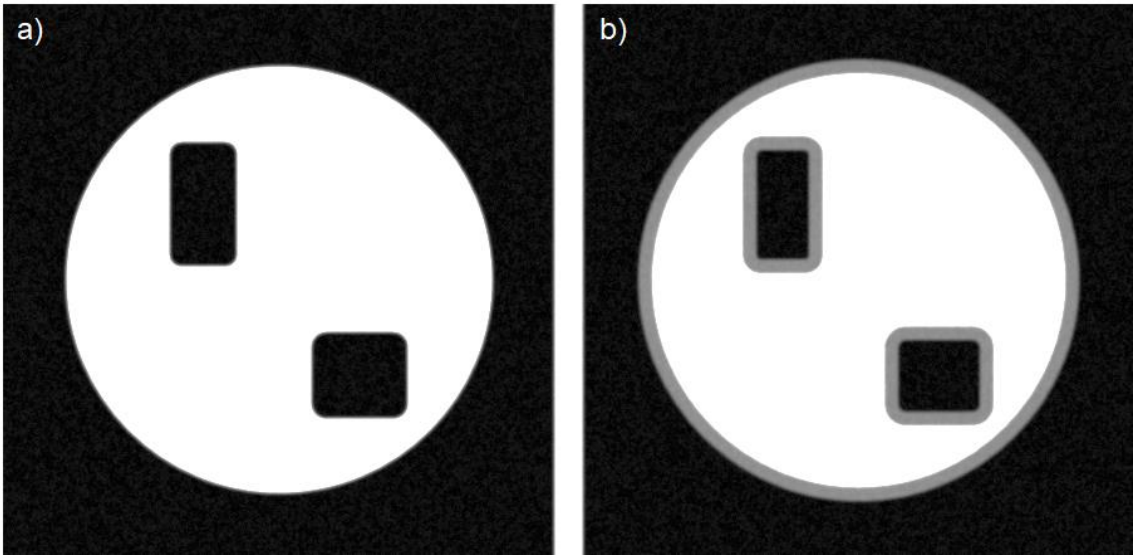

Figure 36. Example of artefacts due to misalignment of the true position of the rotation axis through the plane of the image. a) Image reconstructed with no centre of rotation offset. b) Image reconstructed with significant centre of rotation offset.

Scale Factor

Due to the image magnification effect of having a diverging X-ray source, the effective pixel size is reduced as demonstrated in Figure 33. The geometric magnification depends on the relative positions of the source diameter, the workpiece and the detector. The magnification factor is then used to scale the effective voxel size in the CT image. Positional errors will therefore directly contribute to error in the scale length.

Misalignment of Source, Detector and Rotation Axis

In cone beam CT it is important that the detector is aligned such that the Y-axis is perpendicular to the rotation axis and the Z and X axis are aligned orthogonally to this and the detector. The influence of misalignment of the detector was investigated in [52] where the authors quantified the magnitude of misalignments before significant image artefacts were observed, an example of the influence of detector tilt is shown in Figure 37. It is possible to quantify and correct for these misalignment errors, this is discussed further in 3.3.1.

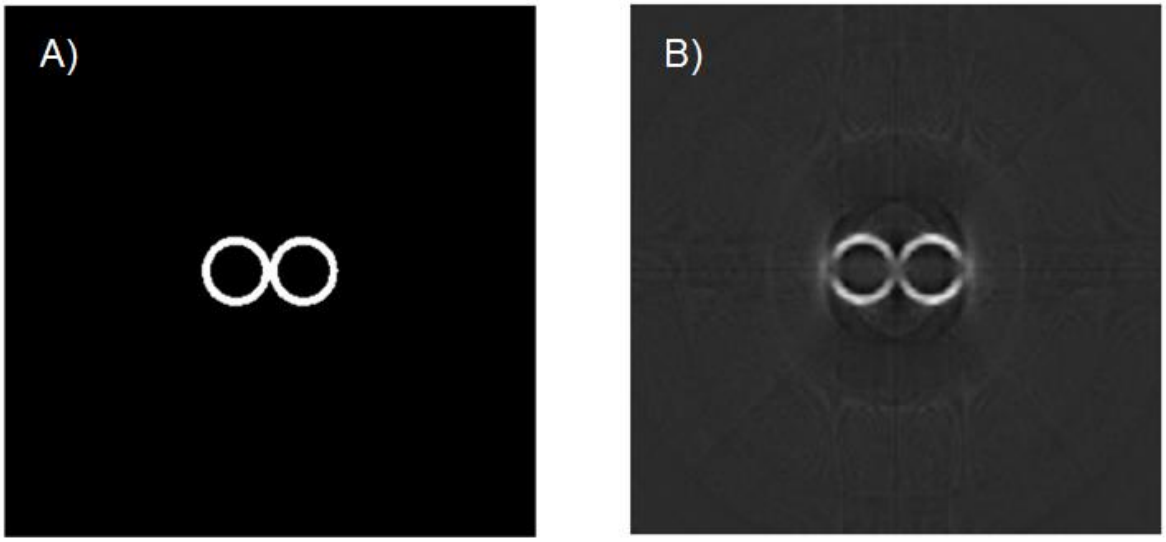

Figure 37. Example of the influence of detector tilt on reconstructed image. A) Original image. B) Simulated image with detector tilt about the x-axis of $\pi/10$ radians. Taken from [52]**.**

Workpiece Stability

The workpiece must be sufficiently fixed and turned by the rotation stage however it is subject to mechanical vibration and temperature variations which may change its

positioning over time. Furthermore suitable fixturing can be hard to achieve in X-ray CT as it can influence the quality of the scan, soft fixturing like foam are often used as an alternative but this can compromise the stability of the workpiece. Movement of the workpiece during the scan can lead to blurring artefacts in the reconstruction which can lead to poor surface determination.

2.3.4 Detector Characteristics

The scintillator and CCD type detector was described in 2.1.3. The quality of the image captured by the detector is limited by how well it can convert the incoming radiation into a digital signal. A number of characteristics associated with this detector type are described in the following.

Pixel Size

The pixel size is the area of each detector element and is therefore related to the resolution of the image, more pixels per area allows higher detail to be obtained. Image magnification can be achieved by using a diverging (fan or cone beam) X-ray source, which can reduce the effective resolution of the pixel. A smaller pixel size also directly influences scan time; halving the pixel size will require four times the exposure value to achieve the same pixel signal.

Quantum Efficiency

The quantum efficiency of the detector refers to how efficiently the detector can convert the incoming radiation into electrical signal. This is energy dependent; meaning that the detector may be biased to some X-ray energies, usually dependent on the scintillator material. The beam hardening effect described in 2.3.2 is therefore not only dependent on the X-ray beam spectrum but also on the spectral response of the detector.

Afterglow

Afterglow describes an effect in X-ray detectors where the intensity signal is recorded after the X-ray radiation have been switched off. This phenomena is associated with the scintillation material of the detector, which converts X-ray into lower energy light. Once an X-ray has been absorbed in the material, it can take some time before the converted

light is released. This effect has potential significance on the quality of X-ray images and dimensional measurement however, little research has been found on this topic.

Cross-Talk

Pixels in the detector do not behave like isolated detectors and the signal can 'leak' across the pixels, either during the conversion to light in the scintillator or charge leakage in the CCD. This phenomena increases the unsharpness of the image beyond the pixel resolution.

Dynamic Range

The dynamic range of the detector describes the range of input signal detectable to the detector. Typically the detector will only behave linearly over a limited input range. When the input single is low, the recorded intensity will often be dominated by the inherent noise of the detector. Conversely, when the input signal is too high the detector output signal will no longer increase linearly with the input signal due to saturation of the detector.

Detector Uniformity

The uniformity of the detector describes how the pixel sensitivity varies across the detector. Variation in the pixel sensitivity leads to ring artefacts, as shown in Figure 38. As this effect is systematic, it can be compensated by performing a shading correction, also known as a flat fielding correction. This also removes other effects such as the angular distribution of the source.

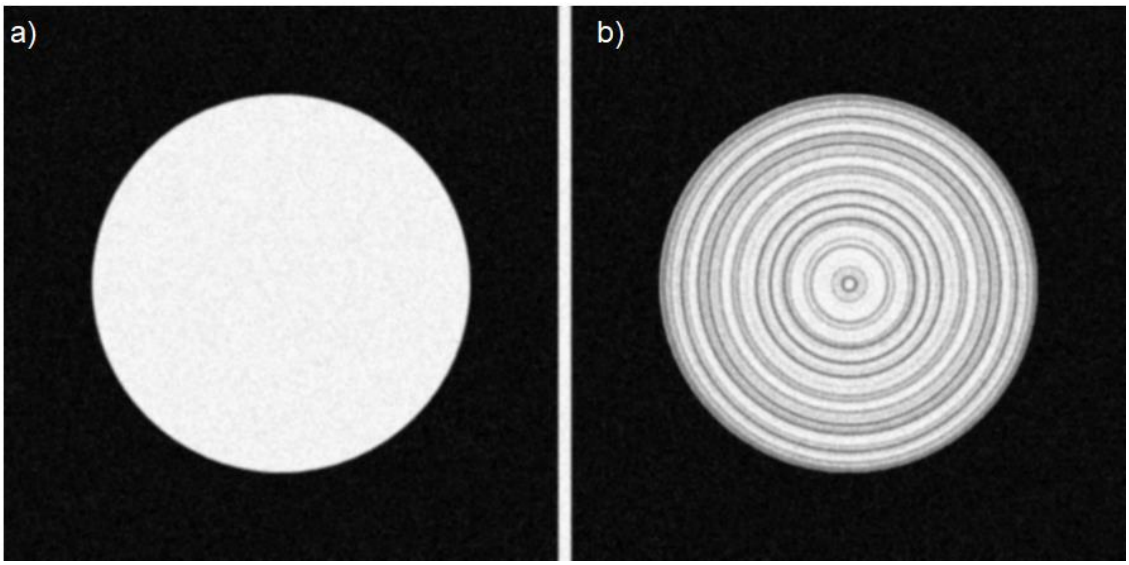

Figure 38. Example of ring artefacts. a) Image reconstructed in absence of ring artefacts. b) Image reconstructed with ring artefacts.

2.4 Chapter Summary

This chapter has introduced the key principles of radiographic and tomographic imaging. The relevant methods of X-ray generation and detection were covered and the main X-ray interaction mechanisms were presented. The fundamental theory of tomographic imaging was explained and how image reconstruction can be achieved through the filtered back projection method. This chapter also touched on how X-ray CT can be achieved in a practical sense and the systematic effects that result from deviation from the mathematic theory. This chapter has therefore given a substantial overview of the tomographic principles which are relevant to the following chapters. Understanding these fundamental concepts will aid in the characterisation of dimensional measurement influences and how they manifest as measurement error.

Chapter 3: Introduction to Dimensional X-ray CT

This chapter is intended to introduce the subject of dimensional X-ray Computed Tomography. A brief history of this field is given, outlining the main drivers towards this novel technology transfer and the existing limitations. An overview of the importance of measurement uncertainty and traceability is given with an explanation of the practical implementation of measurement uncertainty estimation. The measurement workflow for dimensional X-ray CT is then presented and each step is explained in detail. The most common influences on dimensional measurements, as cited in current scientific research, are discussed, highlighting the gaps in current understanding. Lastly the current state of dimensional X-ray CT is reviewed.

3.1 Industrial X-ray CT for Dimensional Metrology

In the previous chapter, the fundamental principles of X-ray CT were explained from the basic theory to how a 3D model is obtained in practice. Although X-ray CT is rooted in the field of medicine, it has expanded into many scientific disciplines and industrial applications over the last few decades [9][53]. One of the latest applications of this technology is in the field of dimensional metrology as a new generation of Coordinate Measurement Machine (CMM) following tactile and optical CMMs [11], [12], [16], [17], [54]. Extracting dimensional information from X-ray CT data requires only a few additional steps; determination of surfaces, fitting of geometric primitives, generating measurands and assigning a physical scale to the image voxels [10]. Furthermore, the measurement of internal features is completely unique to X-ray CT, giving it a special advantage over existing techniques. The main barrier that must be overcome however is ensuring measurements are traceable to measurement standards by estimating the task specific measurement uncertainty [55], as will be explained in the following section. This is considered to be a difficult task in X-ray CT due to the many influence factors associated with the measurement procedures [55]. Previous studies have shown that attempts to estimate measurement uncertainty are unreliable, even amongst expert users [56]. It is expected that by increasing the current understanding of this technology, that uncertainty estimation can be performed more reliably in the future.

3.1.1 History of Dimensional X-ray CT

X-ray CT was first applied in the medical field since the invention by Hounsfield in the late 1960's, it has since expanded into industry for non-destructive testing purposes and eventually for dimensional measurement in the early 1990's [6]. The measurement accuracy of such systems was limited which can in part be attributed to metrology not being the main design intent [17]. Since this time dedicated metrology systems have been introduced by a number of CT vendors [30]–[34], [57]. In the absence of any published standards for dimensional measurement using X-ray CT systems, the Association of German Engineers or Verein Deutscher Ingenieure (VDI) developed guidelines for these purposes which are widely used by a number of CT vendors and serve as the sole documentation for citing metrological performance for X-ray CT systems [24]–[28].

3.1.2 Novel Capabilities of X-ray CT

Since X-ray CT is capable of reconstructing a 3D model of an object, it follows that dimensional information can be readily extracted from the data. The final result of a CT scan is a grey-scale image, representative of the X-ray attenuation [47]. With this image, a point cloud of the surface can be generated, comparable to the output of a conventional tactile CMM but typically containing several million co-ordinate points [16]. Furthermore, each material interface can be identified including internal surfaces. It should also be noted that the number of points captured is independent of the scan time. It is these properties that give X-ray CT some unique measurement capabilities [58][59]:

Wall Thickness Analysis

As internal features can be measured in X-ray CT, wall thickness measurements can be generated at any or all locations on the workpiece, from this pass/fail reports can easily be generated to quickly assess if a part is within the specified tolerances.

Nominal/Actual Comparison

This is useful for assessing the overall deviation of the real part against the CAD model. It can also be used to assess the deviation of two different parts against each other.

Simultaneous Inspection

The cost of X-ray CT inspection is relatively high compared with other techniques, therefore, performing simultaneous inspection can offset the cost of these inspection steps by using the data for multiple tasks such as integrity inspection and dimensional measurement. Industrial CT is also increasingly being used for surface texture measurement, providing further scope for combining inspection tasks. It is these unique capabilities that has led to the industrial interest in X-ray CT for dimensional measurement.

3.1.3 Measurement Uncertainty and Traceability

The International Vocabulary of basic and general terms in Metrology (VIM) [60] defines measurement uncertainty as:

"Parameter that characterizes the dispersion of the quantity values that are being attributed to a measurand, based on the information use."

It is regarded as a quantification of the level of doubt surrounding a measurement, which is only considered complete when accompanied by an expression of uncertainty [61]. An expression of uncertainty therefore allows measurements to be compared and evaluated in a universal and independent manner. In manufacturing, a measurement without a statement of uncertainty is insufficient for decisions to be made about whether a component lies within or outside of the specified design tolerances. No measurement is perfect, which means a level of uncertainty surrounding the measurement must exist. All measurement results are therefore expressed as:

$$Y = y \pm U$$

Equation 48

Where y is the mean value of the measurement and U quantifies the associated measurement uncertainty. Measurement uncertainty allows traceability to the definition of the meter. Traceability is defined in VIM as:

"Property of a measurement result relating the result to a stated metrological reference through an unbroken chain of calibrations of a measuring system or comparisons, each contributing to the stated measurement uncertainty." [60].

This allows two measurements on different systems to be properly compared provided they each have an unbroken chain of uncertainty evaluation. Measurement traceability is a requirement of international standards e.g. ISO 9001 [62] and is therefore crucial in high value manufacturing.

Every measurement is prone to sources of error. These error sources may be numerous depending on the measurement instrument or measurement task. For instance almost all measurements are subject to measurement error deriving from thermal effects, i.e. the length of a 1 m steel bar will increase by approximately 60 µm if it is heated from 20°C to 25°C. Temperature affects not only the measurement instrument but the workpiece as well. For this reason, international guidelines state that all measurements must be performed at 20°C and any temperature variation from this value must be corrected for accordingly [63]. In order to find the true value of a measurement therefore, the value of workpiece and instrument temperature must be known. In reality this temperature measurement will have an associated uncertainty which will propagate through to an uncertainty in length measurement. At first measurement uncertainties seem problematic, however if one accepts that uncertainty is part of measurement and takes steps to analyse each of the sources of error involved in the measurement, the uncertainty can be estimated through construction of an uncertainty budget. This is one method for calculating the uncertainty, however measurement uncertainty evaluation is generally done by one of four methods:

i. Uncertainty budget calculation from model equations as described in the Guide to Expression of Uncertainty in Measurement (GUM) [20];
ii. Procedure for Uncertainty Management (PUMA) method [64];
iii. Substitution method using calibrated workpieces;
iv. Simulation of measurement process.

A combination of these methods is also acceptable. The GUM is regarded as the most important document relating to the estimation of measurement uncertainty, for a complete handling of the measurement uncertainty the methods outlined in the GUM should be used [65]. The goal of the GUM method is to calculate the measurement uncertainty analytically through model equations that relate the influencing factors to the measurand [66],

$$Y = f(a, b \ldots z)$$

Equation 49

Where Y is the measurand, a, b and z are the factors that influence the measurement. The uncertainty of each of these will then propagate through to the final uncertainty. The uncertainties of the input values can be determined statistically, known as a type A uncertainty, or by prior knowledge or expert experience, known as a type B uncertainty. A simplified version of this for a more practical approach for use in industry is known as the Procedure for Uncertainty Management (PUMA) as described in ISO 14253-2 [64]. Even using the PUMA method, knowledge of the main influence factors involved in the measurement are still required. The main difference between the GUM and the PUMA method is that the PUMA method is applied iteratively and optimised based on cost considerations, it is therefore more suitable for industry applications.

The substitution method allows the measurement uncertainty to be estimated experimentally by performing repeated measurements on calibrated workpieces that are representative of the measurements performed on the workpiece, the calculated uncertainties can then be transferred to the workpiece measurements as described in [67]. The advantage of this methods is it does not require knowledge of all the influence factors involved as the uncertainty and bias is measured using the reference standard and directly transferred to the workpiece. This method does however require a large number of repeated measurements to be performed which can be time consuming.

According to [67] measurement uncertainty is typically broken up into four components:

$$U = k\sqrt{u_p^2 + u_w^2 + u_{cal}^2 + u_b^2}$$

Equation 50

Where u_p is the uncertainty associated with the measurement procedure, u_w is the uncertainty associated with the workpiece, u_{cal} is the uncertainty associated with the calibration of the system and u_b is the measurement bias.

Simulation methods of uncertainty estimation can be advantageous for reducing the effort and cost of repeated measurements, but often use simplified models or assumptions and require experimental validation [68]. Uncertainty evaluation using simulation is covered in ISO 15530-4 [69].

3.1.4 Calibration and Verification

Calibration and verification are two kinds of checks that are performed which can indicate the metrological performance of a measurement system. These terms are often confused and it is important to point out the difference. Verification is defined as,

"Confirmation through examination of a given item and provision of objective evidence that it fulfils specified requirements." [60].

Verification is a standardised test that either confirms or rejects that an instrument is performing within given specifications, usually the maximum permissible error [70]. If the instrument fails the test then the performance specifications need to be changed to agree with the test results. This check is usually repeated on a periodic basis to ensure it is performing correctly.

Calibration is defined as,

"*Operation establishing the relation between quantity values provided by measurement standards and the corresponding indications of a measuring system, carried out under specified conditions and including evaluation of measurement uncertainty."* [60].

Calibration therefore establishes traceability of the measurement to international standards. In the context of a CMM system, a verification statement regarding system performance is used (as defined in ISO 10360) as a route to traceability, since a manufacturer cannot guarantee a task specific measurement uncertainty with their system. Currently no standards exist for verification or calibration procedures for dimensional X-ray CT systems although a new part of the verification series ISO 10360 is under development specifically for CMMs with CT sensors [29], more information on this is given in 3.4. For CMMs, calibration involves mapping the individual kinematical error sources of the system [66], this is much more complex for X-ray CT systems as error can arise from a large number of sources other than those associated with the kinematics [71]. The following section will outline the main processes for obtaining dimensional measurements with X-ray CT.

3.2 Dimensional X-ray CT Workflow

In order to identify the key influencing factors, the typical X-ray CT workflow for extracting dimensional measurements is presented in Figure 39. These are the main steps that are performed during a typical X-ray CT scan, each of these is also explained in this section. This section will also highlight the differences between the conventional CMMs widely used in industry and CMMs based on the tomographic method.

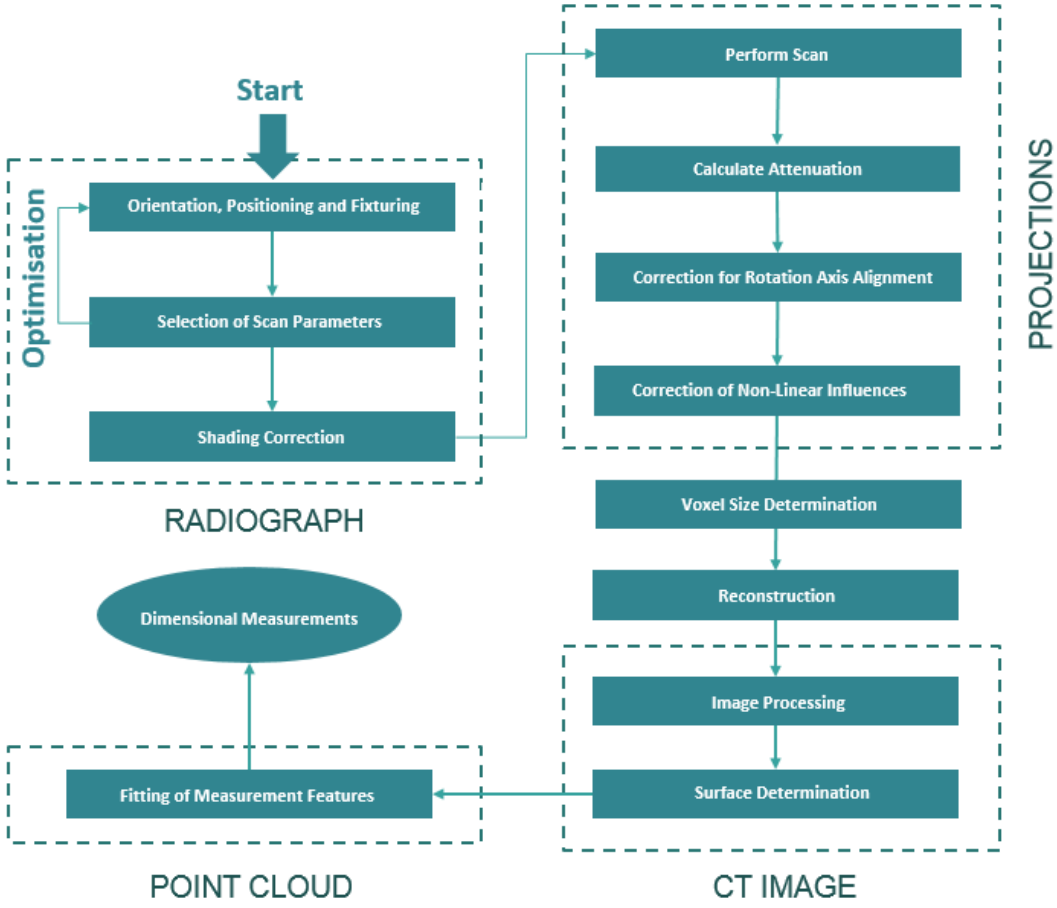

Figure 39. The typical process flow for dimensional X-ray CT tasks.

Orientation and Positioning

The first step in a CT scan is to position the workpiece in the X-ray beam, this requires selecting the orientation of the part and position within the X-ray beam. When choosing the orientation of the workpiece the operator will usually orientate it such that it reduces the maximum path length for X-ray penetration [72]; larger path lengths will require a higher X-ray energy to achieve the same transmission value. Other considerations may include avoidance of large cone angles in the vertical direction – to minimise the angular subtend of the object along the rotation axis to reduce the influence of Feldkamp artefacts [73] as discussed in 2.2. The magnification of the part is also selected. By increasing the magnification factor the image can be spread over more pixels, making the effective dimensions smaller and increasing the resolution of the image. The limit of the achievable resolution is usually dictated by the source diameter size as it becomes comparable to the effective pixel size [74]. A higher magnification

factor also occupies more space on the detector and to avoid image artefacts it is necessary to capture the shadow of the entire workpiece in the detector at all angles. The chosen orientation and position of the part will ultimately depend on the workpiece geometry and the requirements of the inspection task and some geometries may be more suited to less conventional scanning modes such as a helical scan acquisition or even computed laminography; which is well suited for planar geometries with very high aspect ratios.

Selection of Scan Parameters

There are a number of user defined parameters that are selected before each scan. These parameters are usually for control of the X-ray source (voltage, current, and filtration), the detector (exposure time, gain) and the data acquisition (number of projections). These parameters can affect measures of the image quality; the spatial resolution, contrast and signal-to-noise or the scan time and there is usually a trade-off between these factors when selecting the parameters [21]. The selection is typically left to the judgement of the operator to decide on the best combination of parameters for 'optimal' results. This step of the process is therefore heavily user dependent and a potential source of measurement uncertainty [75].

Flat Field Correction

The shading or flat field correction compensates for the non-uniformity of the X-ray source and detector pixel sensitivity [76]. The correction scales the individual output of each pixel such that when the X-ray source is on and no object is present the pixel value is uniform over the entire detector field. Insufficient correction can lead to so called ring artefacts as described in 2.3.4. The flat field correction captures two reference images; a flat field, F, and a dark field, D. The flat field is a frame or mean of many frames captured during constant tube output and no obstacles between the source and detector. The dark field is captured in the absence of radiation; a measure of the systematic offset of the detector output. The corrected image, C, is then obtained from Equation 51 where P is the uncorrected image.

$$C(x,y) = \frac{(P(x,y) - D(x,y))}{(F(x,y) - D(x,y))}$$

Equation 51

Each reference image must be obtained for each new set of parameters and ideally for every scan as the X-ray source and detector characteristics vary temporally.

Data Acquisition

During the data acquisition step, projections are captured by the detector as the workpiece is rotated by the manipulator. The positioning of the workpiece is susceptible to errors arising from thermal expansion of the scanner components, mechanical vibration and alignment of coordinate axes [77].

Correction of Rotation Axis Position and Alignment

This is a standard software correction to compensate any differences in the assumed position and the true position of the axis, it can also compensate for misalignment of the axis [76]. If uncorrected, it can lead to image artefacts as described in 2.3.3 and potentially influence measurement results. Several automated methods exist, some assessing the variation between pairs of opposite angular projections [78], others iteratively determine the rotation centre through optimisation of reconstruction image quality parameters [79].

Correction of Non-Linear Effects

The principal non-linear effects in X-ray CT are beam hardening and scattering as discussed in 2.1.2 and 2.3.2. The effect of these influences are well documented in X-ray CT, leading to cupping artefacts, streaking and loss of contrast [51][80]. For correction of beam hardening in single material objects, common methods involve linearization to correct for the influence of beam hardening by directly measuring the attenuation curve through the use of stepped wedges [81] or estimation using simulation or iterative techniques [16] [82]. For multi-material objects, beam hardening correction is more complex but can be performed by scanning the object using multiple energy sources [83]. The beam hardening effect can also be reduced using hardware filters such as

metal plates to pre-harden the X-ray source spectrum. Deconvolution methods [84], [85] can be used for the correction of scatter or this can be directly measured using scatter grids or hole-plates [86] or simulated through Monte-Carlo methods [87].The influence of beam hardening and scattering on dimensional measurement is reviewed in more detail in 3.3.2.

Voxel Size Determination

The individual elements that make up the reconstructed CT image are commonly referred to as voxels. To extract dimensional information from this data, each voxel must be assigned a physical size, this can be done through Equation 52 as defined in [88].

$$V_s = \frac{nd}{mN_v}$$

Equation 52

Where n is the number of detector pixels perpendicular to the rotation axis, d is the detector pixel size, m is the geometric image magnification factor, equal to:

$$m = \frac{Source - to - Object\ Distance\ (SOD)}{Source - to - Detector\ Distance\ (SDD)}$$

Equation 53

and N_v represents the number of voxels to which the data is mapped which is arbitrary but is usually set such that it is equal to n. For accurate voxel size determination, SOD, SDD and the pixel size must be calibrated as error in these quantities will propagate to errors in the voxel size determination. It is typical to perform a calibration of the scale axis by scanning a reference object of known dimensions to correct for any systematic errors in the scale. This check is usually performed periodically to verify that the scale error is below some specified value, similar to the verification test for CMMs. Rescaling may also be done during the scan by scanning the workpiece and reference object simultaneously or consecutively without moving the position along the magnification axis. A number of reference objects have been suggested for this task but it is important that the calibrated reference length is independent of the surface

determination step as this could influence the result [88]. Centre-to-centre distance of holes, spheres or hemispheres are therefore appropriate for this task.

Reconstruction

The mathematical theory of reconstruction that was presented in 2.2 covered the Fourier based reconstruction method implemented via filtered back projection (FBP). FBP reconstruction is more commonly used over algebraic or statistical reconstruction methods as it is more computationally efficient [9] allowing for shorter reconstruction times. For cone beam CT however, exact reconstruction with FBP is not possible for circular scan trajectories and Feldkamp artefacts occur as a result as described in 2.2.5. These artefacts have been shown to influence dimensional measurement data in a number of studies [89][90].

Post Processing

Any post processing of the data is included in this step which typically includes image filters such as Gaussian or Median filters to reduce noise or post reconstruction artefact correction. These filters are typically applied to improve the data quality, however the influence of these filters on dimensional measurement are in general not well understood and may contribute to measurement uncertainty. Common post-processing steps will therefore be analysed in the experimental trials in Chapter 4.

Surface Determination

Edge determination is a crucial step for obtaining dimensional measurements from X-ray CT data [17]. This process involves estimating points in the image that correspond to the interfaces between materials, where particular features or the entire surface geometry of an object can generated and dimensions can then be extracted [12]. In X-ray CT images, material edges correspond to a change in the local grey-scale value. Ideally these changes are sharp, reducing ambiguity in the edge position and making estimation of the edges fairly trivial. In reality the CT grey-scale values transition from one material to another over a number of voxels, furthermore the presence of image noise and artefacts can influence this process [91]. There are a number of methods of surface determination which are not exclusively used for X-ray CT data, and can be

roughly grouped into two categories; local and global methods. Local methods define the edge based on the immediate vicinity of the edge using for example the edge gradient to determine the edge position. Global methods typically use the entire image statistics to compute a single threshold value that is used to separate one material from another. The most commonly used methods of surface determination in X-ray CT are the ISO-50, Otsu and Canny methods. Each of these is briefly described in the following sections.

ISO-50

The ISO-50 method is a global surface determination commonly used to segment single material X-ray CT data. The threshold is determined by analysing the grey-scale histogram, a typical example is shown in Figure 40. The grey-scale histogram records the occurrence of each grey-scale value in the data. To determine the threshold value, firstly, peaks in the histogram are identified, these correspond to the mean grey-scale of a material if the profile of the peaks are symmetric. The ISO-50 threshold between any two material peaks is defined as 50% of the difference in grey-scale value between the two peak values. For the example shown in Figure 40 the material peak occurs at 121.795 and the background peak at 0.509, the ISO-50 threshold is therefore 61.152.

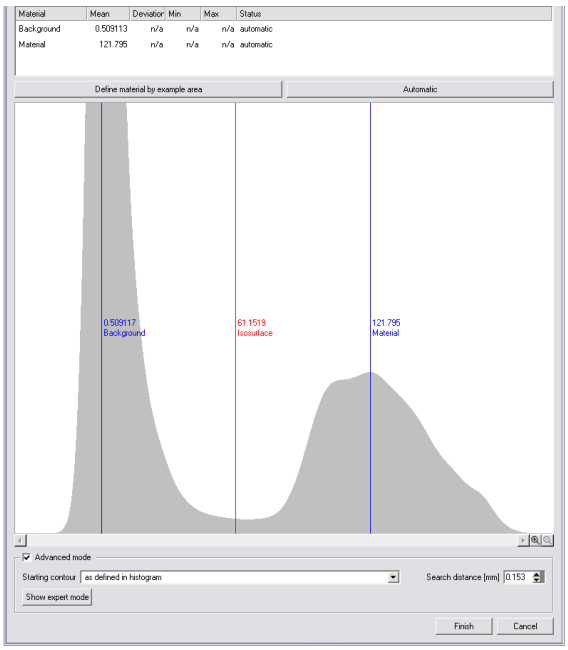

Figure 40. Example of ISO-50 thresholding. The ISO 50 threshold grey-value is taken as half-way between the material and background peaks.

The main advantage of the ISO-50 method is that it is can be calculated very quickly. The ISO-50 does not typically select the optimal threshold value however, for measurement this usually results in systematic error [59]. Furthermore, local variation in the grey-scale values can limit the effectiveness of global thresholding.

Otsu

The Otsu surface determination method is also threshold based. This method also relies on the grey-scale histogram statistics to calculate a threshold value. This is done by selecting the threshold value that minimises the within-class variance, σ_W^2, defined in Equation 54, as

$$\sigma_W^2 = W_b\sigma_b^2 + W_f\sigma_f^2$$

Equation 54

Where W_b and W_f are the fraction of background and foreground pixels to the total number of pixels and σ_b^2 and σ_f^2 are the variances of the background and foreground pixels. The within-class variance is therefore calculated for each threshold value and the Otsu threshold is that which returns the smallest value of σ_W^2. A more efficient way of calculating the Otsu threshold value is described in the original publication [92]. The advantage of the Otsu method is that it can determine a more optimal threshold value as it considers the variance of the histogram values, not just the peak values. The Otsu method requires performing more calculations than the ISO-50 method and can therefore be time consuming especially for large data sets. Like the ISO-50 method it relies on bimodal data and can be unreliable when the area of the material is much smaller than the background and vice versa. The Otsu method is another example of global thresholding and therefore retains many of the limitations of the ISO-50 method.

Canny Edge Detection

The Canny edge detection algorithm was developed by John Canny for finding edges in images with a low error rate [93]. The Canny edge detection method consists of 5 primary steps:

- Smoothing operation to reduce image noise;

- Gradient operation to identify changes in pixel values which indicate edges;
- Non-Maximum Suppression to thin edges by finding the local maxima;
- Segmentation of strong and weak edges by setting two thresholds;
- Suppression of weak edges unconnected to strong edges through hysteresis.

The simplicity and accuracy of the Canny method has made it one of the most popular methods for automatic image edge detection. It is inherently successful at avoiding false edges and is less affected by variation and noise. This method can be classed as local as it considers the neighbouring region when performing steps 3 and 5. The influence of these three methods and others on dimensional measurement has been investigated in a number of studies, which have universally found that global thresholding methods are less accurate than localised determination [17], [59], [91], [94]. Although the Otsu method is generally considered more accurate than the ISO-50 method, it was found to exhibit a large bias in the presence of image artefacts [95]. It is recommended therefore that when using a thresholding method such as ISO-50 or Otsu that the global threshold be adapted based on the local grey-scales [91]. One study compared such a local adaptive technique against a Canny edge detector, finding that the Canny method to have a much reduced uncertainty [96]. After considering the surface determination methods above it is clear that the preferred method for metrology purposes is a local edge gradient based method. Other studies such as [91] have considered testing multiple surface determination methods in their work, however, since gradient based methods have consistently outperformed threshold based methods for dimensional measurements, it is therefore considered little value to include these in this work.

Resolution and Unsharpness

In General, the resolution of an image relates to how well two distinct features can be distinguished from each other. Definitions of these two concepts have been found in [97] with resolution defined as;

"The ability of an imaging system to register separate images of two closely situated objects."

And unsharpness as;

"The ability of an imaging system to reproduce a sharp edge."

The unsharpness will therefore influence the resolution of the image, along with a number of other factors, namely noise and contrast.

Classically, spatial resolution has been defined using the Rayleigh or Sparrow criteria [98]. Since these criteria relate the resolution to whether or not two objects can be distinguished, physical structures are typically used to determine the limits of resolution of a system. These artefacts generally use patterns of line structures with varying spacing between them. Determining the resolution in this way can be subjective since it usually requires some amount of human judgement.

These line patterns can be useful for 2D radiographic imaging however since it can be easy to include these patterns with the image. So called Image Quality Indicators (IQIs) are used in industrial 2D radiographic inspection to provide a traceable measure of the image resolution [99]. It is more complicated however to give a measure of resolution in 3D X-ray CT due to the dependence on a large number of factors, although artefacts have been developed for these purposes – it is much more difficult/impossible to scan these simultaneously with the object. Since the resolution will depend on the position within the scan volume, scan settings, object material and materials path, it is almost impossible to practically quantify the scanner resolution since such an artefacts would also need to be scanned in many positions under many different settings.

Other, more objective, ways of assessing the performance of an imaging system use either the Point-Spread Function (PSF) or the Optical Transfer Function (OTF) [100]. The PSF describes the ability of an imaging system to reproduce a single point [101], the OTF describes the ability of an imaging system to reproduce a sinusoidal function across a range of spatial frequencies. In this way the PSF can be thought of a measure of unsharpness and the OTF a measure of the resolution. These two functions are related to each other mathematically; with the OTF being the Fourier transform of the PSF,

$$OTF = \mathcal{F}[PSF]$$

Equation 55

The OTF itself is comprised of two other function describing the contrast and phase components of the OTF named the Modulation Transfer Function (MTF) and the Phase Transfer Function (PTF) respectively,

$$OTF(\omega) = MTF(\omega)exp[iPTF(\omega)]$$

Equation 56

It follows therefore that the MTF is equal to the modulus of the OTF and for this reason the MTF is typically measured in place of the OTF. Through the relationship defined in Equation 55, the MTF can be derived from the PSF and vice-versa. It is often more practical however to measure the 1-dimensional Line Spread Function (LSF). The LSF can be obtained by measuring the response to a line object in one direction which is equivalent to a circularly symmetric PSF. The MTF can then be obtained by taking the Fourier transform.

Fitting Geometric Features

Once the surface points have been determined, geometric features can then be fitted such as planes and spheres. The fitting algorithms and fitting parameters can influence the measurement results similarly to other CMM point cloud data as generated from tactile or optical systems for example. One advantage of X-ray CT is the large number of surface points that can be extracted from a single scan, allowing significantly greater coverage than a tactile system with comparable acquisition times (in the order of tens of minutes); reducing the influence of random error.

Dimensional Measurement

Once measurement features have been fitted to the data, dimensional measurands can be extracted. It is also possible to extract Geometric Dimensioning and Tolerancing (GD&T) features, perform CAD/Nominal comparisons and wall thickness analyses. Recent research has also demonstrated the feasibility of using micro X-ray CT to measure surface roughness of AM components [102]–[104]; not only does this allow characterisation of internal surfaces but can provide more information than conventional techniques as it allows sub-surface and re-entrant features to be

extracted. The final and arguably the most important step is measurement uncertainty evaluation which is discussed in Chapter 5.

3.3 Influence Factors

As previously discussed, dimensional measurements in X-ray CT involve an edge determination step, this usually involves finding regions where the image grey-scale values have the largest change, represented mathematically by the gradient. The determination of edges is susceptible to systematic error which can bias the edge position in a given direction. It is important to note however that not all types of measurement will be directly influenced by a systematic edge offset, for example the position of hole centres will not be affected by a global edge offset, shown in Figure 41.

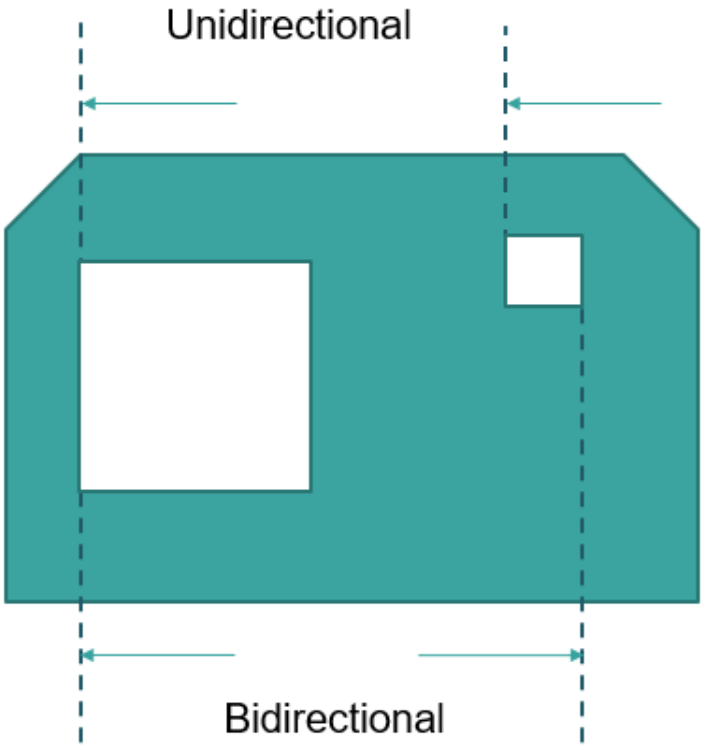

Figure 41. Schematic illustration of unidirectional and bidirectional length measurements.

It is useful therefore to split X-ray CT measurements into two categories, known as unidirectional and bidirectional measurements. These terms refers to the direction of probing as would be the case for tactile CMMs; unidirectional being from the same direction and bidirectional from opposing directions (Figure 41). Within the German guideline series VDI/VDE 2630 there contains a list of potential influencing variables

[25]. The following sections discuss some of the most common influences studied in the scientific literature. These influences can largely be separated into two categories; those that influence the voxel size determination step (unidirectional) and those that influence the surface determination step (bidirectional).

3.3.1 Unidirectional Error

The main source of unidirectional error in X-ray CT is cited as global scale error [88] by incorrect voxel size determination. From Equation 52 and Equation 53 it is shown that the voxel size is directly influenced by the Source-to-Detector Distance (SDD) and the Source-to-Object Distance (SOD). The uncertainty in the calibration of these distances will therefore propagate through to an uncertainty in the voxel size. This relationship also assumes perfect alignment of the linear and rotational axes; some studies have attempted to quantify the influence of positional and rotational error of the axes on the CT image [105]. As demonstrated in 2.3.3 the correct alignment of these components is crucial to avoid image artefacts which can then potentially lead to other sources of error (3.3.2). The position of the rotation axis is used directly for determination of the voxel size (Equation 52) and therefore directly influences the voxel size [77]. The accuracy of axis positioning on non-metrology X-ray CT systems is not adequate for most dimensional measurement tasks. However, this can be overcome through the use of a calibrated reference artefact (Figure 42).

Figure 42. Image of CT ball bar. Steel balls fixed to ends are located with tactile CMM to create a calibrated reference length. The ball bar is scanned by the CT system and used to scale the dataset.

The artefact typically consists of two or more spheres, allowing the distance between them to be calibrated on a tactile CMM. This acts as a reference length to which the voxel size can be more accurately scaled. A description of how this artefact is used can be found in the following chapter.

A number of reference workpieces have been proposed and tested for this purpose. A 'fibre gauge' workpiece was proposed by [106] consisting of holes and pins. The inner and outer features allowed for correction of surface threshold value as well as scale length error. Other workpieces consist of ball bars [54], ball bearings or ruby spheres on carbon fibre rods as used by [88].

Thermal expansion of the workpiece will also manifest as a unidirectional error [107] so it is necessary to record the temperature inside the machine and correct for any systematic errors resulting from thermal effects. So called 'source diameter drift', referring to variation in the position of the source during the scan, has also been investigated for its influence on dimensional measurements. Movement of the source can potentially change the SDD leading to error in voxel size determination, it may also lead to image artefacts, influencing the surface determination also (see 3.3.2). Heating of the source components during operation can potentially lead to movement of the source [25]. The drift of a source diameter on one industrial X-ray CT system was measured in [108], it was found that the drift was significantly greater when starting from 'cold' than when measured after a few hours of operation. A compensation method for instability of the projection images during the scan was applied in [109], the corrected and uncorrected data was reconstructed and compared, finding surface deviations with a standard deviation of 5 µm.

Localised scale errors have also been detected in dimensional X-ray CT due to misalignment of machine components and detector distortions. It was reported in [110] that geometric image distortions due to detector defects could lead to local scale length variation, these errors were then mapped and a correction was applied leading to reduced error variation.

3.3.2 Bidirectional Error

Bidirectional errors are those associated with the detection of edges in X-ray CT. Whether specific influence factors lead to a bidirectional length error depend on the surface determination method, but in general, surface determination can be influenced by image artefacts, image noise and image contrast. The accuracy of surface determination also related to the image resolution. The most common causes of image artefacts in cone beam X-ray CT include beam hardening [51] (cupping artefact, streak artefact), scattering [80] (cupping artefact), Feldkamp effect [9] (Feldkamp artefact, cone beam artefact), misalignment of the CT geometry [52], movement of the workpiece or geometry during the scan [111] (motion artefact) and non-uniformity of the detector or X-ray source [112] (ring artefact).

The effects of beam hardening have been widely cited as influencing dimensional measurements in X-ray CT [91], [113]–[118]. These studies concluded that beam hardening systematically leads to dilation of edges in X-ray CT; the position of the edges moves in the direction of the surface vectors, causing outer dimensions to increase and inner dimensions to decrease [118], [119]. Interestingly, studies performed on Beam Hardening Correction (BHC) using linearization methods found that corrections are typically insufficient and can sometimes lead to overcorrection of the beam hardening effect, which can lead to erosion of the edge [114], [117], [118]. This is usually due to lack of knowledge of the attenuation curve which is not only dependent on the workpiece material but also the source spectrum, filtration and detector properties. Methods to reproduce the attenuation curve exist however [120]–[122] which can improve the validity of the BHC. The accuracy of these corrections are still influenced by other factors however such as scattering and source or detector uniformity. A doctoral thesis by Lifton, investigating the influence of both beam hardening and scattering concluded that these influence factors are not independent and correction methods for each is necessary for reducing systematic edge error in X-ray CT [91]. The reason why BHC and scattering leads to these errors was not fully understood however and further work may be necessary to understand why these systematic errors are observed.

The influence of the spatial resolution on dimensional measurement does not appear commonly in the literature however it is expected that image unsharpness can influence the edge detection. Attempts to quantify the influence of spatial resolution on measurement found that errors were more pronounced at a higher resolution [123] however as the authors state this is most probably explained by stronger Feldkamp artefacts at a higher magnification and is therefore independent of the spatial resolution. Further investigation into the influence of spatial resolution on measurement is required. The influence of Feldkamp artefacts on the probing error form (PF) and probing error size (PS) was investigated by comparing cone beam and helical CT data [89]. Simulated projection data was used in order to remove other influences ~ 25 µm probing error form was found in in the cone beam data at a 17.3° cone angle compared to approximately 7 µm in the central plane and in the helical data. Helical data is more susceptible to errors from misalignment of scanner components however, which is not represented here as the simulated data was not affected by such influences.

3.4 Current State of Dimensional X-ray CT

3.4.1 Uncertainty Estimation for X-ray CT Measurement

Measurement uncertainty estimation in X-ray CT has been studied using the various methods described previously in this chapter. The use of the GUM for X-ray CT is not currently seen as feasible due to the many influence factors involved and lack of guidelines [124]. Some studies have been conducted using simulation for uncertainty estimation [125][126].

Estimation of measurement uncertainty by the substitution method is probably the most popular approach to date, where uncertainty is obtained experimentally using calibrated reference workpieces [127]–[129]. A large number of reference objects has been developed for correction of some systematic errors, [130] [131] [106]. Studies have shown that uncertainty estimation in X-ray CT is at best unreliable [132], further work to quantify these influences is therefore needed before traceability of X-ray CT measurements can be established.

3.4.2 Guidelines, Standards and Good Practice

Currently there is no recognised standardisation for measurement uncertainty evaluation or performance testing for X-ray CT [133], The most widely used documentation is the German guideline VDI/VDE 2630 [24]–[28] series which aims to apply the methods of the ISO 10360 for CMM performance testing to CMMs with CT sensors. There is currently an international working group, ISO TC 213 WG10 generating an additional part of the ISO 10360 series to include CMMs with CT sensors [134]. A number of studies have also proposed various reference tests for the purposes of verification e.g. [135] but these are still on-going. In X-ray CT, measurements are highly dependent on the geometry and material of the workpiece and the positioning of the part within the scan volume. This makes it especially hard to verify the measurement performance for all tasks. The relevance of these standards is considered in the following chapter when performing experimental trials.

3.4.3 Metrology X-ray CT Systems

Metrology dedicated CT systems entered the market around 2005 with the Werth TomoScope [30]. Since then a large number of vendors supply metrology versions of their products. Much of the focus of these systems has been to improve temperature control and employ CMM-like kinematics such as air bearing, granite bases and high accuracy linear encoders to improve the accuracy and repeatability of part positioning. Corrections for non-linear influences such as scattering have been employed, e.g. scatter correct from GE [136] which uses a scatter grid to measure and correct the scatter distribution. Some vendors have integrated CT data into their existing metrology software, allowing better comparison between X-ray CT and CMM measurements as data can be directly compared without exporting STL files which can further influence results, e.g. Zeiss [33]. Vendors currently state the performance of these systems according to the VDI/VDE 2630 guideline, a review of several leading manufacturers has shown the first term error for unidirectional sphere-to-sphere length measurement ranges from 3.5 µm - 15 µm.

3.5 Chapter Summary

This chapter has introduced the important concepts within the field of dimensional X-ray CT. This is a relatively new technology and there is much ongoing development to establish X-ray CT as a standard measurement system in industry. X-ray CT has many unique benefits over existing CMMs but this chapter has shown how this complex process is susceptible to many sources of measurement uncertainty. The main error sources have been studied extensively in the literature and can be divided into two categories:

i. Errors that result from uncertainty in the instrument geometry such as the alignment and positioning of the source, detector and rotation axis. These errors are well understood and with careful calibration, the first term error for unidirectional sphere-to-sphere length measurement ranges from 3.5 µm - 15 µm as quoted by seven leading dimensional X-ray CT vendors according to the VDI/VDE 2630 guideline.
ii. Errors introduced during the process of edge detection. These error sources are much less well understood and depend on the quality of the tomographic images which is known to be influenced by non-linear effects. These errors are much more problematic as they are often task specific and therefore cannot easily be compensated.

Due to the complexity of these error sources, at present, the best estimation of measurement uncertainty is made by analysing the measurement results from carefully designed calibration artefacts. The following chapter of this thesis will use such an artefact to assess the magnitude of these different error type and try to understand the main influencing factors associated with the second type of error.

It is expected that by understanding many of the fundamental influences on measurement, that error sources can be quantified, improving accuracy and estimation of uncertainty. The ultimate goal is to be able to quantify and correct for all known errors in X-ray CT, thus achieving a fully calibrated system. This chapter has highlighted the limitations of the existing research within the current state of dimensional X-ray CT which will serve to guide the direction of this doctoral research.

The objectives of the following chapters will be to investigate and attempt to quantify the magnitude of the key influences outlined in this chapter. This work will focus on the influences that are associated with the edge determination step. In order to do this, some experimental scans will be performed on several micro-focus X-ray CT systems including a comparison between a metrology purposed system and a conventional X-ray CT system in order to highlight the sources of error which are not related to the mechanical precision of the X-ray CT system. After finding the most dominant influences on edge determination through experiment, the key influences will isolated using simulation to quality their individual and combined effects.

Chapter 4: NPL Hole-Plate Study

This chapter presents an experimental study whereby a calibrated reference artefact was scanned using three industrial micro X-ray CT systems and dimensional measurements extracted from the data. The aim of this work is to assess the performance of these X-ray CT systems for dimensional measurement tasks and to identify some the main influence factors in order to steer the direction of the following chapters.

4.1 Background

This experimental work was completed as part of a study coordinated by the National Physical Laboratory (NPL) for their work towards metrological verification of X-ray CT. The NPL had manufactured and calibrated an artefact (Figure 43) based on that designed by their German equivalent Physikalisch-Technische Bundesanstalt (PTB). For the purposes of their study the artefact was then sent to a number of X-ray CT users around the UK where they would perform CT scans on their systems and share the data collected. As such the Manufacturing Technology Centre (MTC) agreed to take part in this study providing the results could be used for the purposes of this doctoral work. The following experimental work was therefore performed by the author using two CT systems at the MTC and another at NPL.

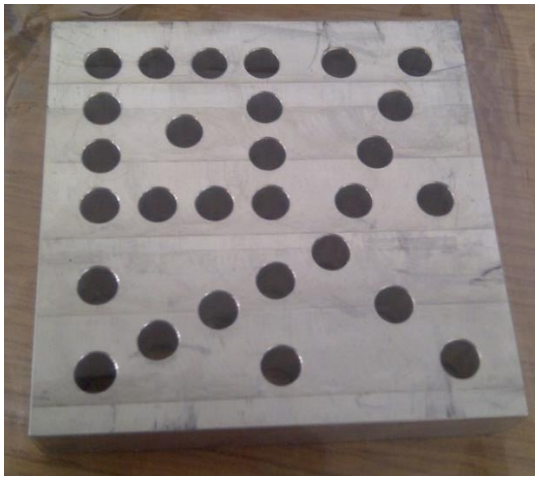

Figure 43. Photograph of the hole-plate artefact provided by the National Physical Laboratories (NPL), Teddington.

4.1.1 Overview of X-ray CT Hole-Plate

The hole-plate artefact was designed by PTB as a suitable artefact for the purposes of metrological performance verification of an X-ray CT system. The example shown in Figure 43 is made from Aluminium and has approximate dimensions of 50 mm x 50 mm x 10 mm with a Coefficient of Thermal Expansion (CTE) of approximately 22 x 10^{-6} K^{-1}. Although no formal standard exists for performance verification of X-ray CT, a number of institutes such as PTB in Germany and NPL in the UK are working on creating a new part of the ISO 10360 series, specifically for X-ray CT. As previously mentioned, the closest document to this is the German guidelines VDI/VDE 2630 which is itself based on the ISO 10360 series. The 10360-2 verification tests require the longest test length to be scaled to the size of the measurement volume, for cone or fan beam X-ray CT systems the measurement volume changes with magnification and as such, a number of different sized artefacts may be required for verification. It is also well known that the workpiece material can strongly influence measurement. The hole-plate was specifically designed so that it could be manufactured and calibrated at a minimal cost, it consists of a single material and could be scaled such that it can be used on different systems or at different magnifications. The ISO 10360-2 standard also requires 5 length measurements along 7 directions, an example of the recommended directions is given in Figure 44 and requires measurements of 5 different lengths along those directions (with the largest length greater than 66% of the measurement volume).

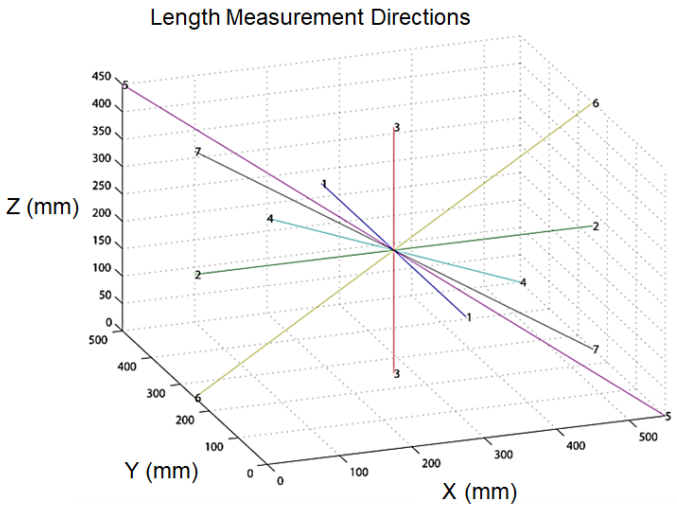

Figure 44. Recommended directions for length measurements in ISO 10360-2 standard. Image taken from [70]**.**

The hole-plate therefore consists of 28 drilled holes that are orientated to give 7 lines of 6 holes (allowing 5 lengths to be measured) as shown in Figure 45. Although the plate only allows measurement of directions within a 2D plane, it will be rotated through a 3D measurement volume during the scan acquisition – this is fundamentally different to the way measurements are performed with a conventional bridge CMM for example and will need to be considered within the additional part of the standard. The diameter and position of each hole is calibrated on a CMM at NPL using a Zeiss UPMC 550 with a stated Maximum Permissible Measuring Error (MPE), E0 $E_{0,MPE} = 1.2 + \frac{L}{400}$ µm The hole-plate is aligned using the three datum features given in Appendix II and a mid-plane is created parallel to datum C at a height of -4 mm to locate it at the nominal centre of the plate. Ten coordinate points were sampled in each of the holes at the mid-plane and circles fitted using a least square Gaussian fit using the Zeiss Calypso software. From this diameter and centre points of each holes were extracted.

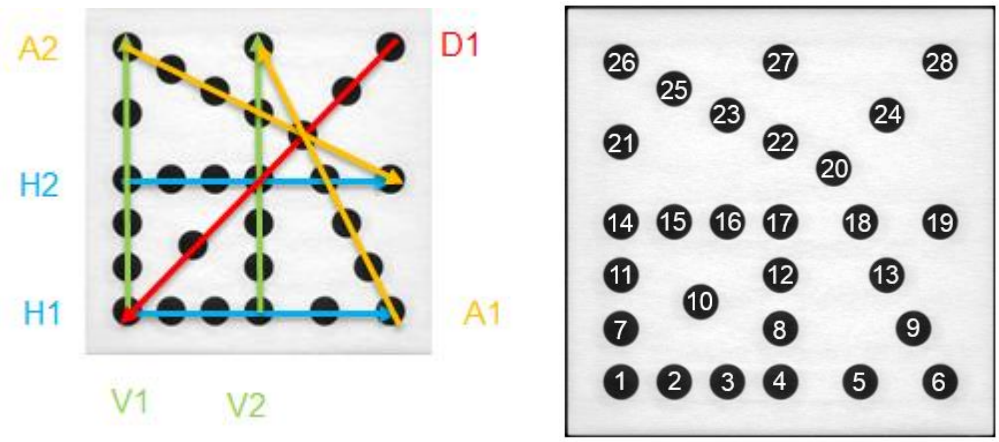

Figure 45. Illustration of hole- plate showing direction of hole-lines and hole ID number.

The hole-plate has two horizontal directions H1, H2, two vertical V1, V2, two angular A1, A2 and one diagonal, D1. This allows the directional dependence of the errors to be analysed. There were two different length measurements that were extracted between hole pairs, these will be referred to throughout as the unidirectional and bidirectional lengths, defined as follows:

i. Unidirectional: distance between centres of the two holes.
ii. Bidirectional: distance between two opposing points of the two holes.

As the unidirectional distances are essentially threshold independent, they will not have a strong dependence on workpiece properties, and can be used to give an indication of other error sources. Conversely, bidirectional lengths will have a strong dependence on the workpiece properties and can be used to assess the influence of workpiece specific error sources.

The unidirectional and bidirectional lengths were calculated between different sets of hole pairs. Along each of the 7 directions, 10 distances are measured; 5 unidirectional and 5 bidirectional between a reference hole and each other hole along that direction. Figure 46 shows the set of points used on each hole to extract the desired length. For example, the bidirectional lengths along the diagonal direction are taken from point b on hole 28 and point g at every other hole along the diagonal row. Unidirectional lengths are all taken from point o.

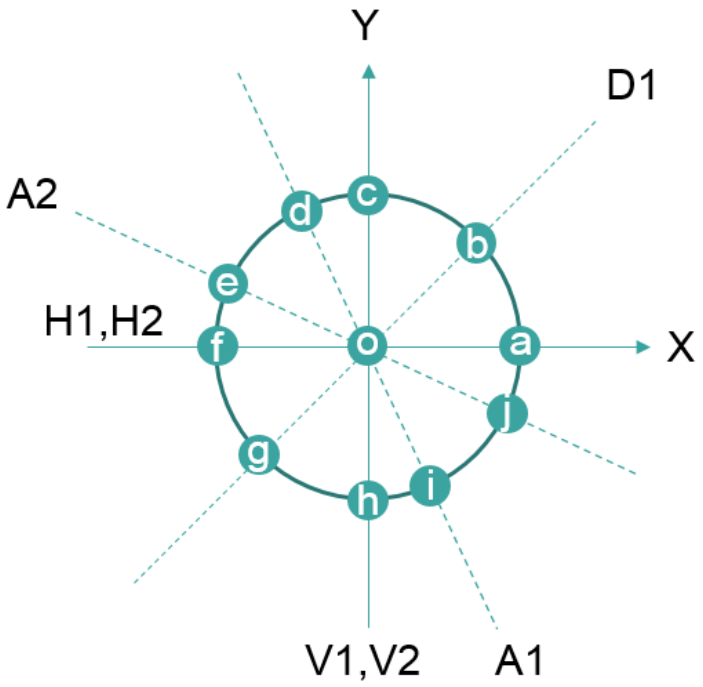

Figure 46. Illustration of the 11 points taken on each hole from which bidirectional and unidirectional lengths are taken from.

The calibration of each of these lengths would normally be very costly and time consuming. As the hole-plate is designed to be a cheaper alternative to other artefacts, the calibration of the bi-directional lengths is performed using an alternative method

according to ISO 10360-2. Here each bidirectional length, Bi_{long}, is estimated using the sum of the long unidirectional length, Uni_{long}, and short bidirectional length, Bi_{short}. An example is given in Equation 57 and illustrated in Figure 47.

$$Bi_{long} \approx Uni_{long} + Bi_{short}$$

Equation 57

All bidirectional lengths were calibrated using the short bidirectional length measured on a single hole. It is important to note these assumptions during the calibration of the hole-plate as later in this chapter it is found that the method used may limit some of the measurement results. The calibrated measurements can be found in Appendix A.

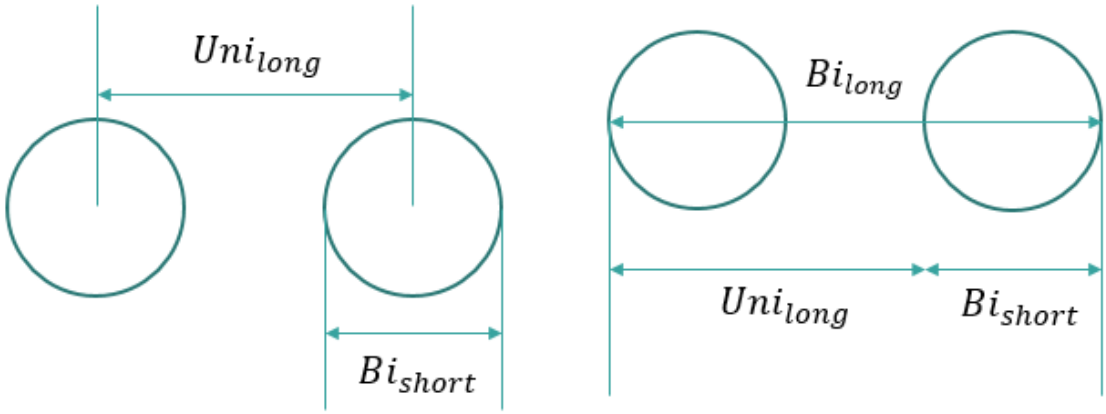

Figure 47. Illustration of long and short bidirectional lengths.

4.1.2 X-ray CT Systems

Three different CT systems were used in this study, two of these were standard industrial X-ray CT systems and the third is a dedicated metrology system. All machines were manufactured Nikon X-TEK. Thus the performance of these systems to measure the different features could be assessed to determine how suitable each system is for each measurement task. The specifications of each system is given in Table 1 and each systems is briefly described.

Table 1. X-ray CT system specifications of three systems used in hole-plate study.

System	Max Voltage (kV)	Min Source Size (µm)	Source Type	Detector Size (mm)	Pixel Size (µm)	Detector Type
XT H 225 ST	225	3	Tungsten Reflection	400x400	200	Varian 2520 FPD
XT H 450 LC	450	80	Tungsten Reflection	400x400	200	Perkin Elmer 1620 FPD
MCT 225	225	3	Tungsten Reflection	400x400	200	Varian 2520 FPD

Nikon XT H 225 ST

The XT H 225 ST, shown in Figure 48, is a medium to high power micro-CT system capable of scanning a wide range of materials and sample sizes. The micro-focus source can achieve a source size of 3 µm (as claimed by the manufacturer [34]) which allows high magnification of up to 150x to be performed, providing sample sizes are small enough to fit within the field of view. The vendor does not provide an MPE statement for this model as it is designed for imaging purposes only.

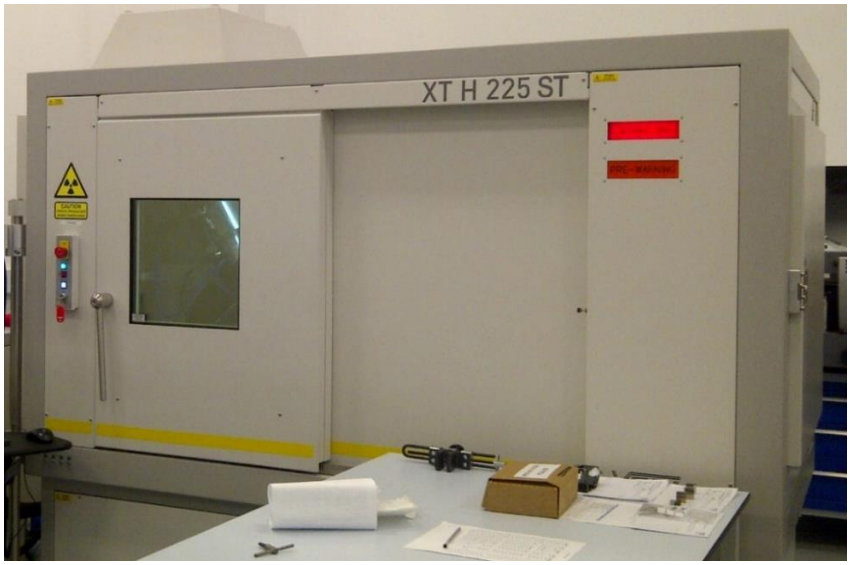

Figure 48. Photograph of XT H 225 ST system at the Manufacturing Technology Centre (MTC), Coventry.

Nikon XT H 450 LC

The XT H 450 LC, shown in Figure 49, is a high powered micro-CT system which can generate twice the acceleration voltage and power of the XT H 225 ST but the minimum achievable source size is much greater at 80 µm up to 50 W for the reflection target [137]. This is mainly due to the greater thermal load on the target, however, as this system is designed for scanning larger objects a smaller source size would typically not be required as the resolution would most likely be limited by the physical size of the object (as the object would not fit within field of view at high magnifications). The vendor does not provide an MPE statement for this model as it is designed for imaging purposes only.

Figure 49. Photograph of XT H 450 LC system at the Manufacturing Technology Centre (MTC), Coventry.

Nikon MCT 225

The MCT 225, shown in Figure 50, is based on the XT H 225 ST which has been modified to make it more robust and suitable for metrology applications. The main new features include a superior mounting of the gun to reduce the influence of thermal expansion of the X-ray tube, a temperature controlled enclosure to meet measurement standards and high precision linear encoders for manipulator axes to improve repeatability of sample placement (particularly important along the magnification axis). The stated

accuracy for sphere-to-sphere distance measurement is $MPE_{SD} = 9 + \frac{L}{50}$ μm according to the VDI/VDE 2630.

Figure 50. Photograph of MCT225 system at the National Physical Laboratory (NPL), Teddington. Image courtesy of NPL.

4.1.3 Experimental Plan

The design of the hole-plate artefact allows measurement of the relative position, diameter and form of the 28 holes. A number of potential sources of measurement error have already been discussed in the previous chapters of this thesis, the goal of this initial experimentation is to demonstrate some of these influences, such as beam hardening, Feldkamp artefacts, source drift and voxel size determination. All X-ray CT systems were housed in a temperature controlled environment however only the MCT system had active temperature control within the enclosure. To reduce the influence of temperature on the measurements at the MTC, the hole-plate was left to 'soak' in the lab in between scans and scan length kept to a minimum.

The hole-plate measurements are split into three parts as shown in Table 2, the first part compares measurements from each of the three CT systems under a similar set of parameters. The second part compares three measurements performed on a single system in different scan orientations as illustrated in Figure 51. The third part compares

three scans of the hole-plate performed on a single system at three different geometric magnification factors. The vertical orientation was chosen for this to maximise the object field of view in the detector plane, to highlight the associated geometric errors.

Table 2. Scanning strategy for each measurement. At each of the scan configurations, three repeated measurements were performed. It is noted that some scan configurations were used in two different parts e.g. 3 and 5.

ID	X-ray CT System	Orientation	Geometric Magnification
Part 1			
Scan Configuration 1	225 ST	Tilted	4
Scan Configuration 2	225 MCT	Tilted	4
Scan Configuration 3	450 LC	Tilted	4
Part 2			
Scan Configuration 3	450 LC	Tilted	4
Scan Configuration 4	450 LC	Horizontal	4
Scan Configuration 5	450 LC	Vertical	4
Part 3			
Scan Configuration 5	450 LC	Vertical	4
Scan Configuration 6	450 LC	Vertical	3
Scan Configuration 7	450 LC	Vertical	1.5

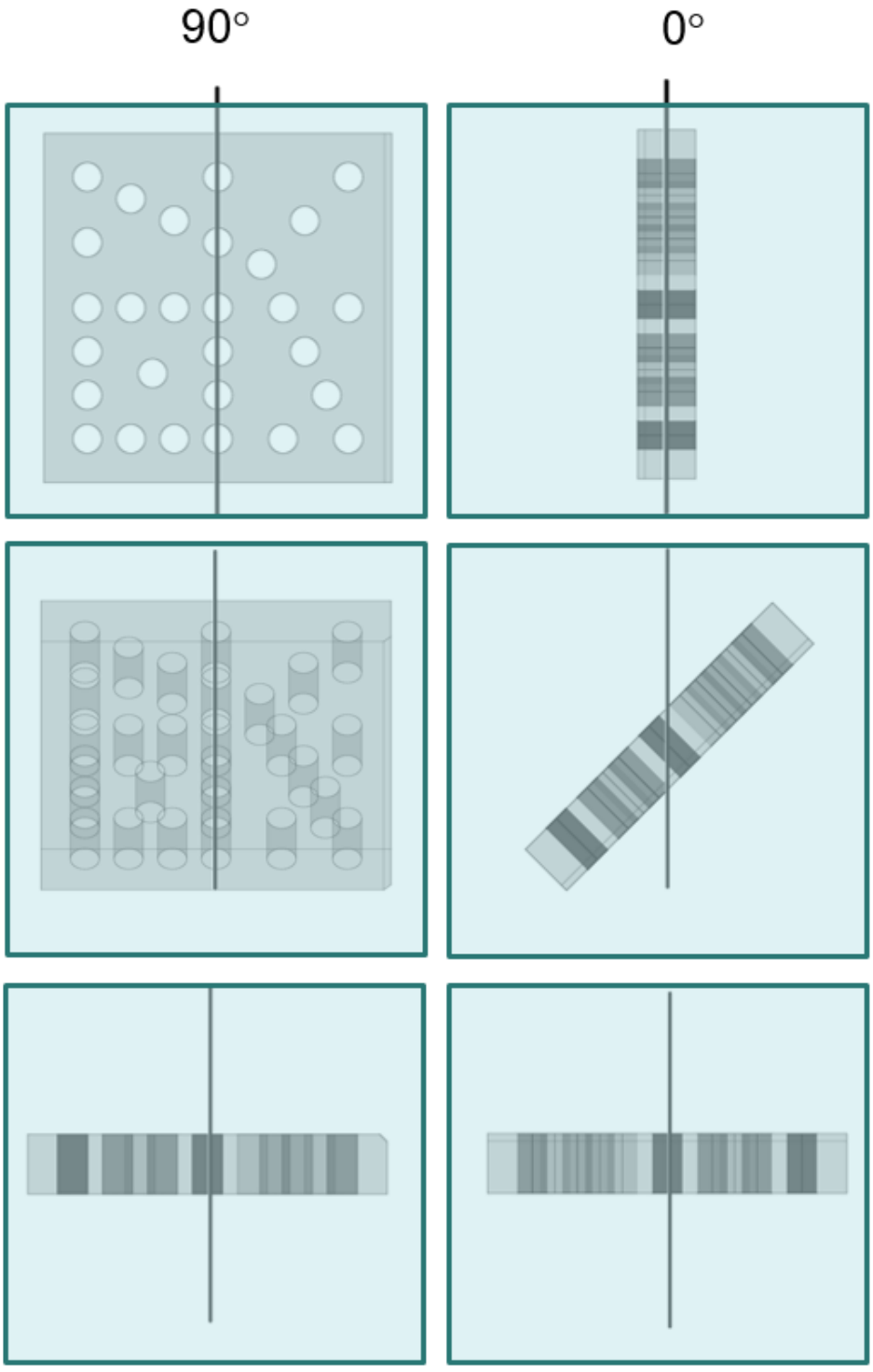

Figure 51. Illustration of the three different scan orientations used, from top to bottom; vertical, tilted and horizontal. The vertical line on each image represents the rotation axis of the scanner, the plates are viewed from the perspective of the X-ray source.

In addition to these varying scan strategies, a number of common software options are considered; pre-reconstruction beam hardening correction and post-reconstruction image filtration are applied to one of the data sets in scan configuration 5. These measurement are extracted and given in part 4 and part 5 of the results section respectively.

Using a measurement template supplied by the NPL (Figure 52), the following information is outputted from each data set:

i. Unidirectional lengths: These were defined as the centre-to-centre points of holes.
ii. Bidirectional lengths: Point-to-point distances in opposing directions as per Figure 46.
iii. Diameters of holes: Gaussian least-square fit of cylinder diameter at the mid-plane of hole-plate.
iv. Hole fit points: Surface points used to generate diameters.
v. 1D Grey-scale Profile: along the diagonal line at the mid-plane slice.

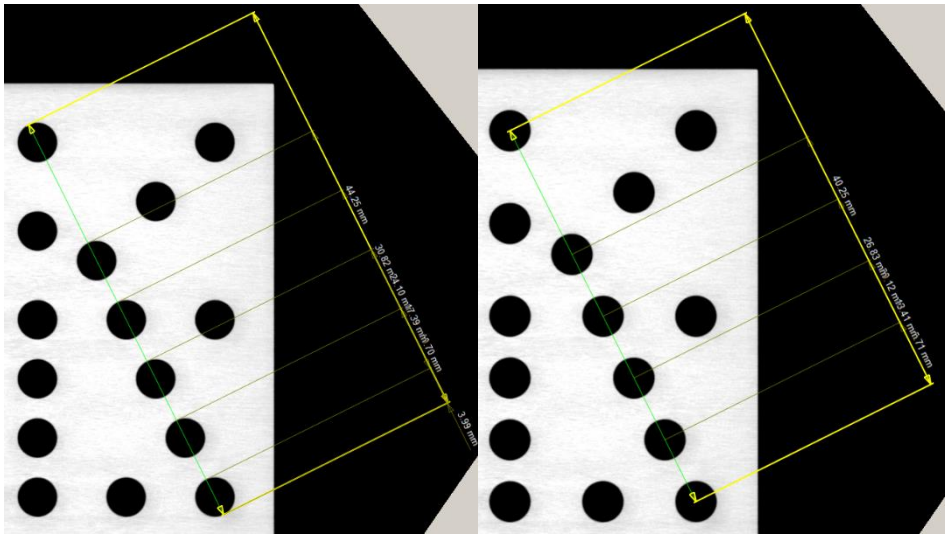

Figure 52.Example of measurements of hole-plate in VG Studio MAX 2.2.

All post processing was performed in VGStudioMax 2.2, relevant settings are given in Table 3.

Table 3. Relevant software settings used in VGStudioMAX for hole-plate measurements.

Setting	Value
Version	2.2.6
Surface Determination	Automatic
Advance Mode	On
Starting Contour	As define in histogram
Search Distance (Voxels)	4.00
Starting Contour Healing	Off
Fit Method	Gauss Least Squares
Auto Fit Points	On
Max. Points	1000
Search Distance (mm)	0.01
Max Gradient (Deg)	15
Edge Void (mm)	0.01
Gradient Mode	Default
Auto Expand	On

4.2 Methodology

This section details the methodology used for the measurement of the hole-plate including the experimental set-up, system parameters used and details of how measurements are extracted from the reconstructed CT data. This methodology closely follows the workflow for dimensional measurements outlined in Chapter 3.

4.2.1 Selection of Parameters

A few trial scans of the hole-plate are performed to better optimise the scan parameters that would be chosen for the scans of the hole-plate. As the hole-plate is scanned in different orientations, different parameters could have been used to optimise the settings for each scan. It is decided however to keep the scan settings constant to reduce the number of variables involved. Due to the inherent differences between the 225 ST,

MCT and 450 LC systems, slightly differing parameters were used to ensure the image signal is comparable between the two systems this is done by increasing the source current on the 450 LC system, in principle the current is related to the intensity of X-ray source and the voltage is related to the mean energy of the X-ray source. The reason for requiring a larger current on the 450 LC may be due to a thicker source window or the different detector models. It is noted that this may also result in a different spectrum. The final parameters are given in Table 4, these settings are used for all scans of the hole-plate.

Table 4. Table of other CT parameters used for all scans, some parameters differed for different machines such as the current, this is to achieve a comparable signal between the 225 ST and 450 LC systems.

System	Voltage (kV)	Current (µA)	Gain (dB)	Exposure Time (ms)	Number of Projections	Frames per Projection
225 ST	180	55	18	1000	1642	1
450 LC	180	100	18	1000	1642	1

4.2.2 Flat Field Correction

For each scan configuration, a flat field or shading correction is performed. For this, two images are captured in the absence of the workpiece; a bright image using the source scan parameters and a dark image where the source is turned off. Only one shading correction is used for each scan configuration, at the beginning of each set of repeated scans as collecting additional corrections requires changing the position of the rotation axis and any error in repositioning would invalidate the calibration of the image magnification factor, as explained in the following section on voxel size determination. Despite this, significant ring artefacts are not seen in the results which would suggest that the flat field correction is sufficient.

4.2.3 Voxel Size Determination

Two of the three X-ray CT systems used in the experimental measurements are not purposed for coordinate measurement tasks, as such the magnification axes are not calibrated to a sufficient accuracy that are required for this work. To obtain a more accurate value of the geometric magnification of the projection images, a calibrated

reference object is scanned for each scan configuration before each of the three repeats. The reference object, shown in Figure 42 in Chapter 3, consists of an aluminium body and arm to which two steel ball bearings are attached. The point-to-point distance of the ball centres are calibrated yearly at a UKAS accredited laboratory.

This distance is used as a reference length to determine a more accurate estimation of the voxel size for the sets of scan data. This method assumes that there is no variation in the value of the geometric magnification between scanning the ball bar and the three repeated scans of the hole-plate. The corrected voxel size, V_c, is therefore calculated in Equation 58 as:

$$V_c = \frac{L_{Ref}}{L_{Ind}} V$$

Equation 58

Where, L_{Ref}, is the reference length, L_{Ind} is the indicated length and V is the original voxel size. To calculate the corrected voxel size, the indicated length must first be measured. This measurement is performed in VG Studio MAX 2.2 after reconstruction by fitting spheres to the ball bearings and measuring the distance between the centre points Figure 53. The software has an in-built feature to adjust the voxel size based on the indicated value of a reference length. After calculation of the correct voxel size, the original value is then updated in each of the three repeats in each scan configuration. It is noted that correction of the voxel size is done after the reconstruction.

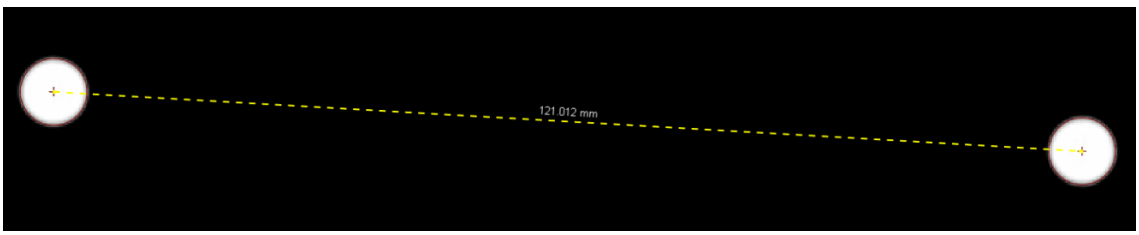

Figure 53. Reference measurement on reconstructed CT image of calibrated ball-bar artefact.

4.2.4 Beam Hardening Correction and Reconstruction

Beam hardening corrections are then applied to the data sets using the built-in options supplied with the Nikon reconstruction software. The correction is performed using a linearization technique; this method applies a non-linear scale factor to the projection

images before reconstruction in order to compensate the beam hardening effect. The limitation of this method is that it requires knowledge of the attenuation properties of the X-ray source. This 'attenuation curve' is unique for each material, voltage setting, target material and filter used for the scan. Without measuring this directly, the attenuation curve is unknown and only an estimation can be used. The software provided a number of pre-set correction options that could be applied, typically relying on the operator to manually select the 'best' correction for each scan. The general form of the pre-set corrections are given in Equation 59 where Y represents the corrected attenuation values and X is the uncorrected values.

$$Y = a(b + cX + dX^2 + eX^3 + fX^4)$$

Equation 59

The coefficient values for each pre-set are given in Table 5. It is noted that for pre-set 1, $Y = X$, and therefore no correction is applied.

The beam hardening correction pre-set 2 is applied to each of the data sets before reconstruction as it is determined to be the most appropriate correction based on the grey-scale profile. Each data set is then reconstructed using a 3D filtered back projection algorithm using the Nikon 3D CT Pro reconstruction software.

Table 5. Coefficient values used in beam hardening correction pre-sets in the Nikon 3D CT Pro software.

Pre-Set	a	b	c	d	e	f
1	1	0	1	0	0	0
2	1	0	0.75	0.25	0	0
3	1	0	0.5	0.5	0	0
4	1	0	0.2	0.8	0	0
5	1	0	0.1	0.9	0	0
6	1	0	0	0.2	0.8	0

4.2.5 Surface Determination

Determination of surfaces in the data is achieved using the in-built functionality in VG Studio MAX 2.2 (Figure 54) from Volume Graphics. There are two options for surface determination, the first using the ISO-50 method and an 'advanced' mode based on the local edge gradient. The specifics of the surface determination algorithm are not available as they are proprietary to the software vendor. The advanced mode is used for surface determination on all data sets; in other studies it has been considered as more robust for dimensional measurement tasks [17].

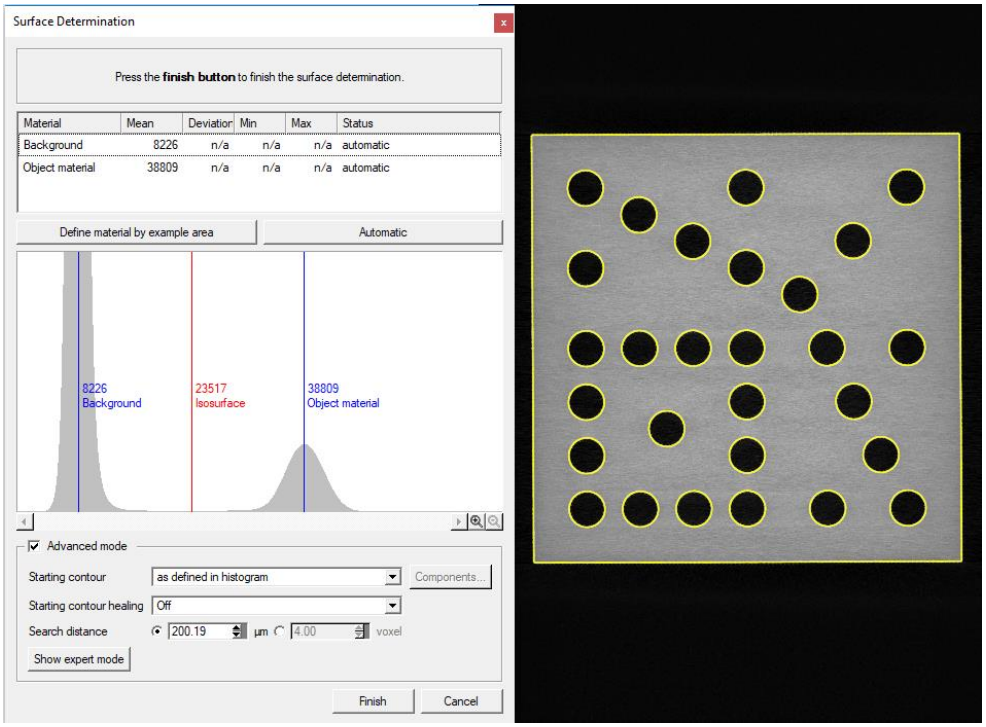

Figure 54.Screenshot of VG Studio MAX 2.2 surface determination options.

4.2.6 Measurement

A more efficient and repeatable way of extracting the desired dimensional measurements is achieved using a measurement template, created by Osamu Sato of the National Metrology Institute of Japan. In order to apply the measurement template correctly the reconstructed data is first aligned to a CAD model using a best fit algorithm (See Figure 55). As there is some symmetry to the hole-plate the alignment had to be manually checked each time to ensure correct orientation. Once in place the geometric primitives are applied to the surface data and a secondary registration is performed

using a 3-2-1 alignment method based on plane, line and point datums in the measurement templates. The measurements were then extracted and exported as a .CSV file. To assess the repeatability of the software workflow, the entire process was repeated five times on a single dataset. It was found that variations in the measurement results deviated no more than 0.1 µm. It was therefore assumed than the need for repeated measurements within the software was not necessary for the subsequent data sets.

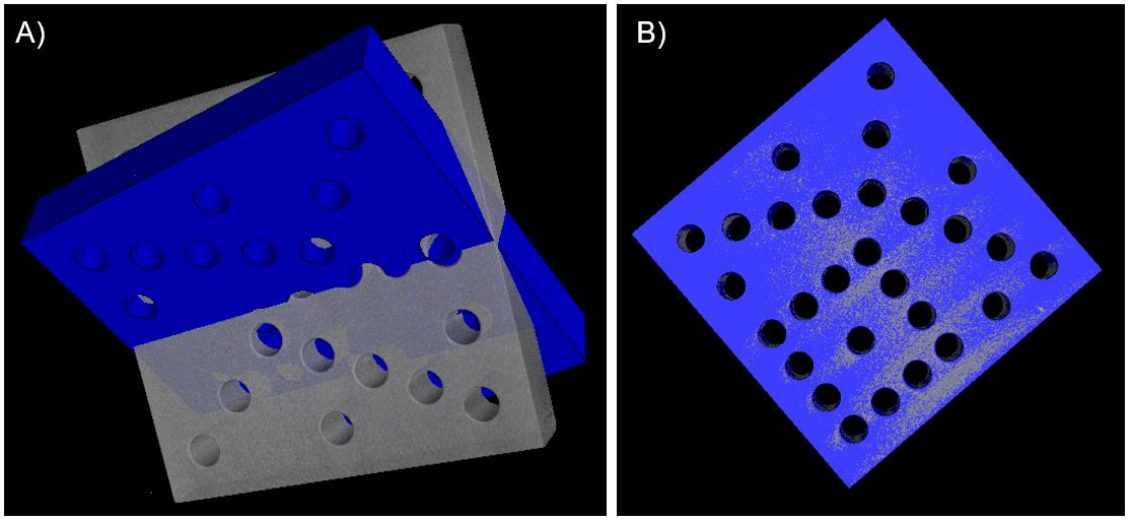

Figure 55.Screenshots of alignment to CAD model. A) X-ray CT surface data and CAD model before alignment. B) X-ray CT surface data and CAD model after alignment.

The measurement results are presented throughout the next section. The error bars, where given, represent the standard error on the repeated measurements. This was calculated using Equation 60.

$$\sigma_{\bar{x}} = \frac{\sigma_s}{\sqrt{N}}$$

Equation 60

Where $\sigma_{\bar{x}}$ is the standard error and N is the number of repeat measurements, which was equal to 3. σ_s is the corrected sample standard deviation, given in Equation 61.

$$\sigma_s = \sqrt{\frac{1}{N-1}\sum_{i=1}^{N}(x_i - \bar{x})^2}$$

Equation 61

Where x_i is the value of each repeated measurement and $\bar{x}$ is the mean value of all repeats.

4.3 Results & Discussion

4.3.1 Correcting for residual scale error

Before the final results are obtained, the scale error is assessed by comparison to the reference measurements of the hole-plate in each of the reconstructed data sets. Figure 56 shows and example of unidirectional length errors against the value of the calibrated reference lengths. Any constant gradient is indicative of a systematic error in the voxel size. The data in Figure 56 is obtained from scan configuration 1 taken on the XT H 225 ST, it is noted that the second two repeats indicate a larger scale error than the first. This is most likely explained by thermal expansion of the X-ray tube during operation as the first repeat is performed 'cold' before the system had been in operation. The approximate decrease in voxel size between repeats 1 and 2 is 0.1% (as calculated using Equation 58) which is also the approximate percentage shortening of the SOD; at a magnification factor of 4 in the XT H 225 ST, this corresponds to a change of 250 µm. For reference this is comparable to the thermal expansion of one metre of aluminium with a difference of 10° C.

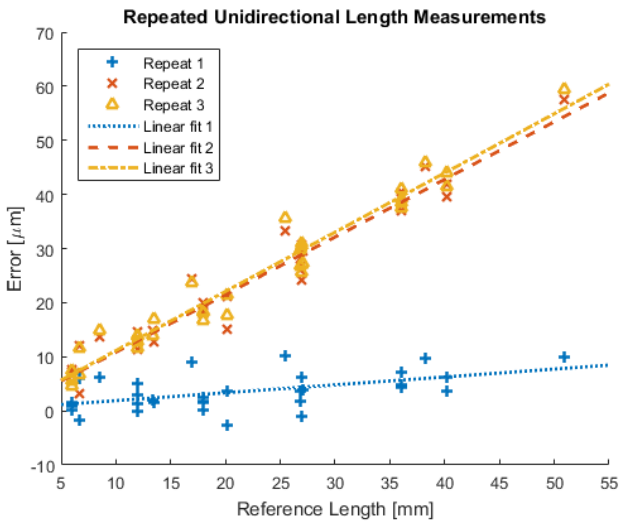

Figure 56. Unidirectional length measurements of three repeated scans on XT H 225 ST. The scale error of each repeated scan can be observed. Figure created in MATLAB ver. R2019a.

This error is observed when using the corrected voxel sizes using the ball bar artefact. This suggests that even when using this method, significant error is still present. A more robust method of voxel scaling is to scan a reference length simultaneously with the scan data. This generally makes scanning more difficult, in this case however, known reference lengths are available from the CMM measurements of the hole-plate. This can be used to remove the global scale error from the data. The result of this is shown in Figure 57.

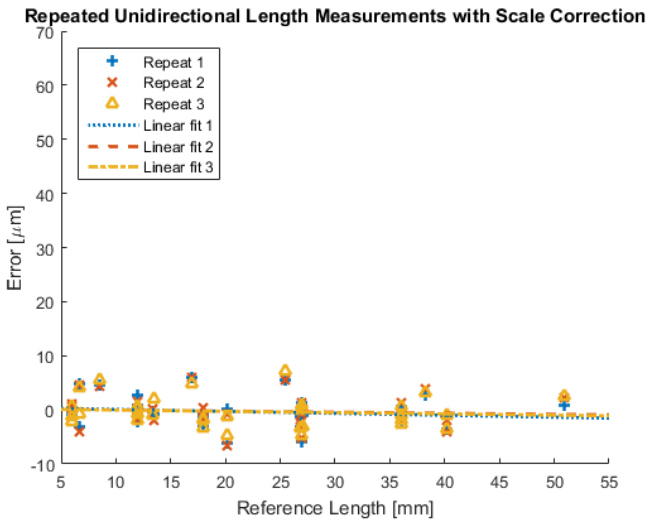

Figure 57.Unidirectional length measurements of three repeated scans on XT H 225 ST after correction of scale error. Figure created in MATLAB ver. R2019a.

4.3.2 Part 1: System Comparison

The first part of the experimental results compare the X-ray CT dimensional measurements of the hole-plates for the three different systems. The following results therefore correspond to scan configuration 1-3 in Table 6 with the workpiece in the tilted orientation for each scan.

Table 6. Scanning strategy for each measurement. At each of the scan configurations, three repeated measurements are performed.

ID	X-ray CT System	Orientation	Geometric Magnification
	Part 1		
Scan Configuration 1	225 ST	Tilted	4
Scan Configuration 2	225 MCT	Tilted	4
Scan Configuration 3	450 LC	Tilted	4

Grey-scale Profile

Firstly, the grey-scale profiles from a single scan on each of the systems is compared in Figure 58. The grey-scale contrast differs quite significantly between the three systems. It is expected that some differences in contrast could occur between the 225 kV and 450 kV systems due to variations in the source spectrum however, it is not clear why there is such a large difference in the grey-scale values between the two 225 systems as a number of factors could contribute to this, for example different scaling of the grey values. One explanation for this may be the uniformity of the source, the less uniform the source the more the flat fielding correction will have to compensate for changes in sensitivity thus reducing the effective dynamic range of the detector. Other noticeable differences in the profiles are at the edges of the configuration 3 profile where the grey-scales appear to drop-off at the edges, this suggests that the beam hardening pre-set has overcorrected for the beam hardening effect, this is possible since the 450 kV source is more filtered than the 225 kV source and is therefore less chromatic. It is not possible to avoid this as the extra filtration is due to the design of the X-ray gun. A larger filter could not have been added to the 225 kV systems due to the physical limitations of the filter fixture.

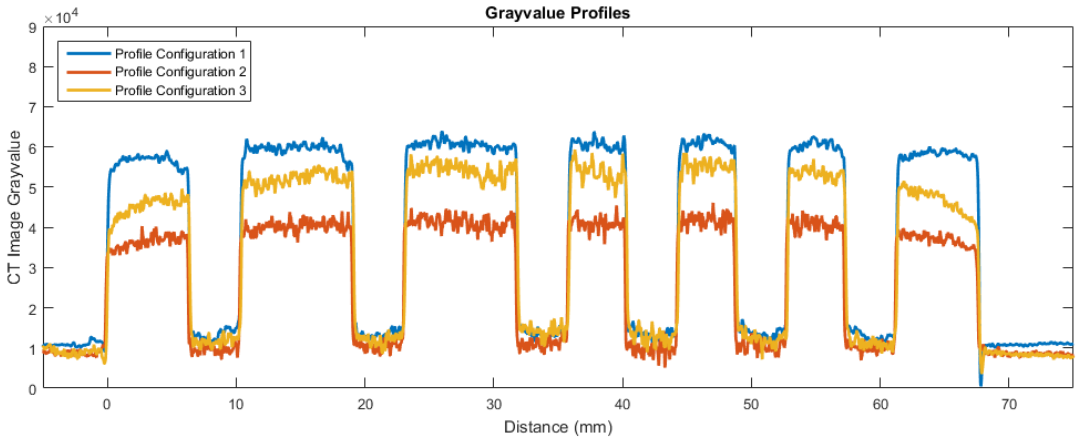

Figure 58. Grey-scale profile of three CT data sets from scan configuration 1, 2 and 3. Figure created in MATLAB ver. R2019a.

Unidirectional Lengths

The mean unidirectional length measurements for each of the three scan configurations are given in Figure 59. These results show that the performance of all three systems are comparable with errors within +/- 5 µm of the calibrated values. The size of the errors appears to be in good agreement between scan configuration 1 and 2 which were performed on the XT H 225 ST and MCT225 respectively, suggesting there is some systematic error or bias in a certain measurement direction especially in the V1, D1 and H1 directions. The results from scan configuration 3 are less consistent with the other two, however not enough information is available to draw any immediate conclusions from these results especially as the repeatability of the magnitude of the errors is approaching the uncertainty of the reference measurements. It is expected that after correction of scale error each of the three systems would perform equally well for unidirectional length measurement as systematic edge effect associated with image artefacts and noise is negated through centre-to-centre measurement.

Bidirectional Lengths

The mean bidirectional length measurements for each of the three scan configurations are given in Figure 60. The magnitude of the bidirectional length error is greater than the unidirectional length error. This is expected as these measurements are influenced by the surface determination more strongly. Most of the length errors now fall within +/- 10 µm of the reference values which is still reasonable considering the 50 µm voxel

size of the data sets. This is in good agreement with similar studies which found that sub-voxel accuracy is achievable with X-ray CT measurements [17]. Comparing all three scan results, it appears that there is systematic bias along some of the measurement directions; A1 and A2 consistently have a negative error whilst V1 and V2 have a positive error.

Diameter Measurements

The results of the diameter measurements are more telling than the bidirectional length measurements as they are less susceptible to image noise and potential issues associated with the calibration of the hole-plate. Systematic errors will be apparent from analysing the hole diameter measurements; as such the mean value of all diameter measurements is plotted in each of the graphs in Figure 61 as a way of identifying any systematic surface offsets. From the three data sets it is seen that the diameter error is relatively small with the maximum deviation below +/- 3 μm. The mean diameter error is slightly negative for all three of the systems.

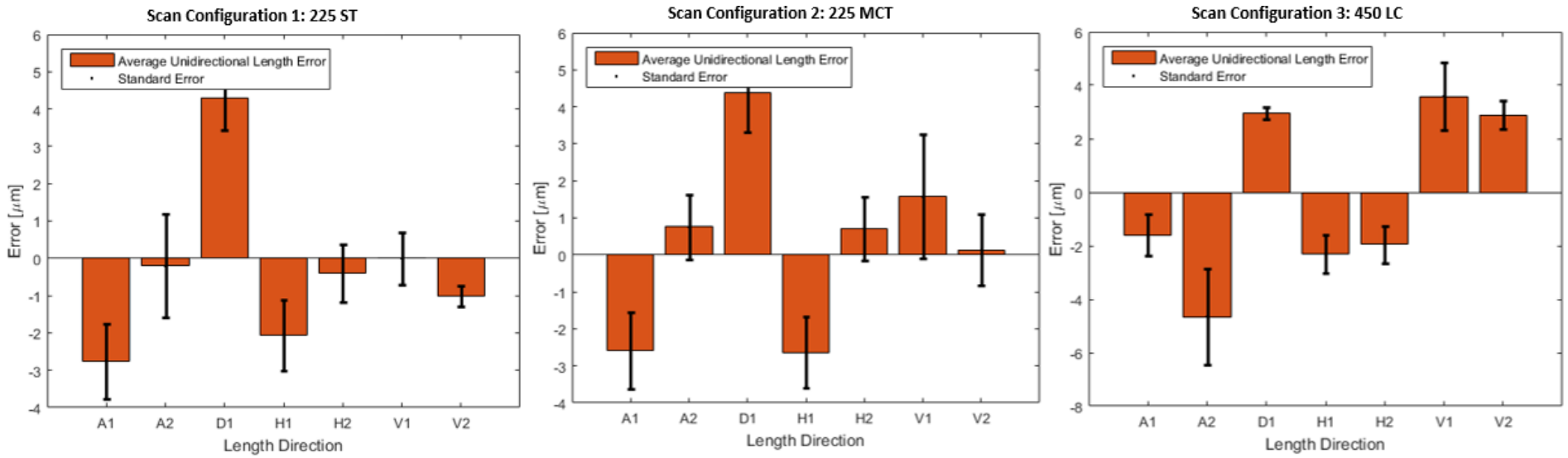

Figure 59. Mean unidirectional length error of each of the five hole-pairs along each length direction. Figures created in MATLAB ver. R2019a.

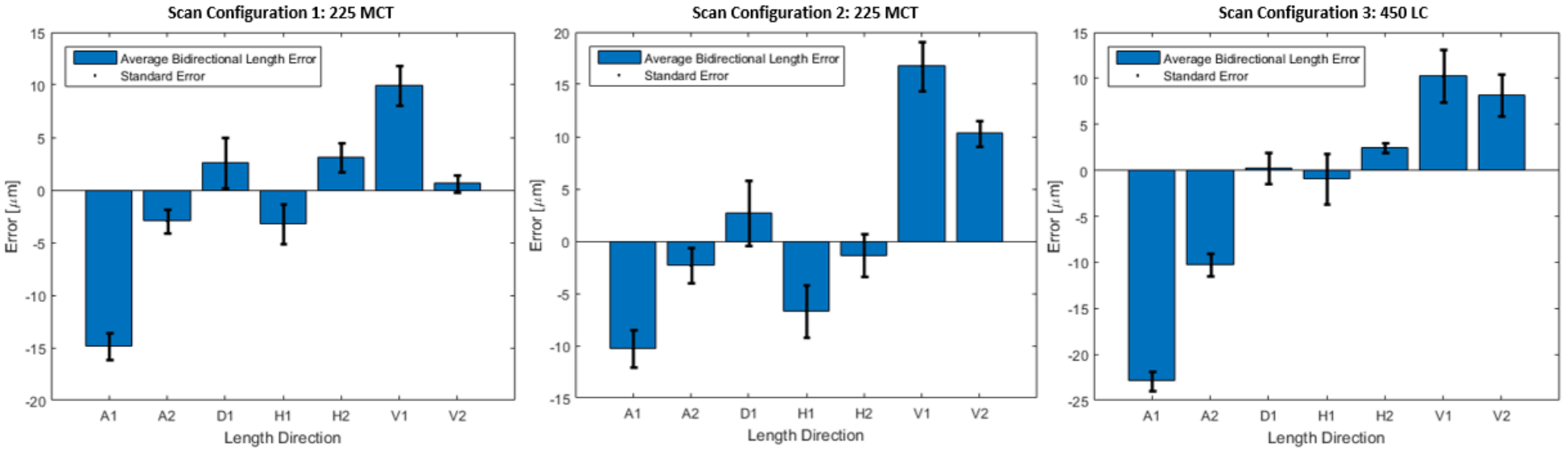

Figure 60. Mean bidirectional length error of each of the five hole-pairs along each length direction. Figures created in MATLAB ver. R2019a.

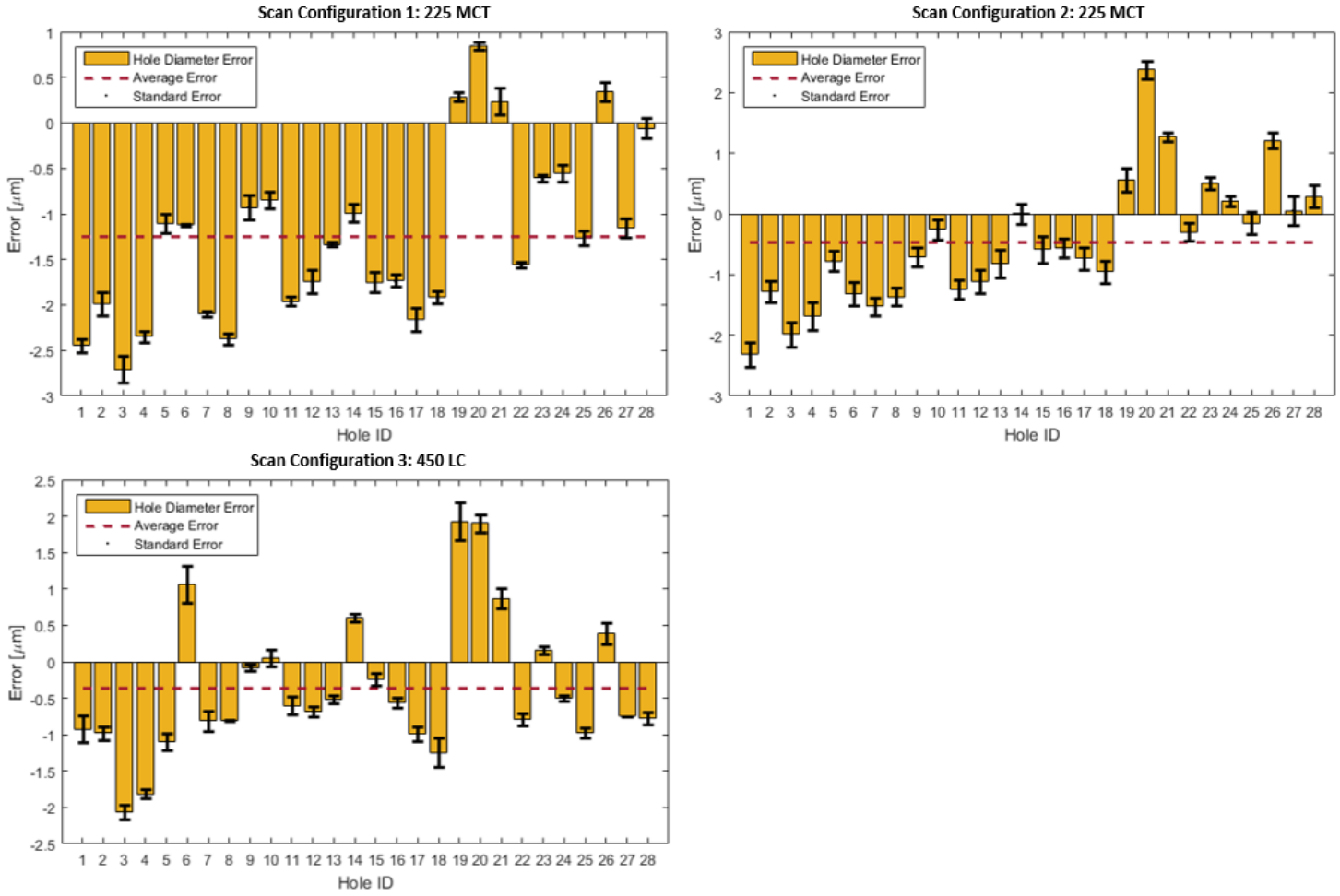

Figure 61. Hole diameter errors for scan configurations 1,2 and 3. Figures created in MATLAB ver. R2019a.

4.3.3 Part 2: Influence of Workpiece Orientation

The second part of the hole-plate results analyses the measurements obtained from scanning the workpiece at different orientations as given in Table 7. Changing the orientation of the hole-plate can potentially influence the measurement results as it can affect the mean path length of the material, changing the beam hardening properties, noise level and image contrast.

Table 7. Scanning strategy for each measurement. At each of the scan configurations, three repeated measurements are performed.

ID	X-ray CT System	Orientation	Geometric Magnification
Part 2			
Scan Configuration 3	450 LC	Tilted	4
Scan Configuration 4	450 LC	Horizontal	4
Scan Configuration 5	450 LC	Vertical	4

Grey-scale Profiles

The grey-scale profiles for the three orientations are plotted in Figure 62. The noise and contrast values are comparable for configurations 3 and 5 which correspond to the tilted and vertical scan orientations respectively. However the increased noise and decreased contrast are seen in the horizontal scan profile (configuration 4). This is expected as the mean X-ray path length through the material is greater than the other two orientations. As the scan setting are kept constant for all scans, a longer path length results in less X-rays detected and therefore a poorer signal-to-noise ratio in the image. The contrast is also reduced due to further beam hardening through the horizontal plate; the difference in attenuation coefficient between aluminium and air is smaller for higher energy X-rays.

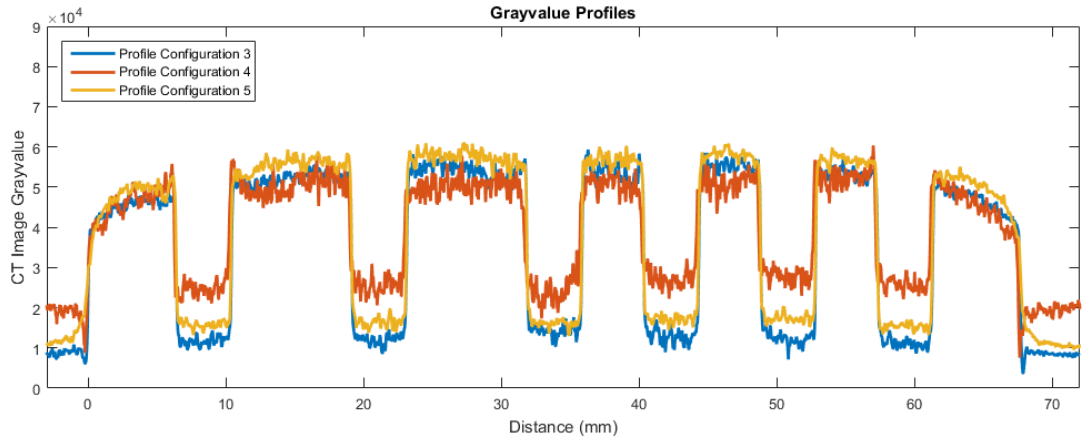

Figure 62. Grey-scale profile of three CT data sets from scan configuration 3, 4 and 5. Figure created in MATLAB ver. R2019a.

Unidirectional Lengths

The unidirectional length error, shown in Figure 63, do not show a clear bias in a specific measurement direction, as expected since the measurement directions now align differently in the scanner in the different scan orientation. This also suggests that these errors are associated with the X-ray acquisition and not with the calibration of the hole-plate or fitting of the measurement template in the analysis software. The largest errors are observed in scan configuration 5, in the vertical orientation, and the smallest errors are recorded in scan configuration 4, in the horizontal orientation. This would suggest that length measurements are more susceptible to error in the direction parallel to the rotation axis.

Bidirectional Lengths

The mean bidirectional length measurements for each of the three scan configurations are given in Figure 64. The bidirectional length measurements vary when changing the scan orientation, this is explained in part by a systematic offset of the surface, as seen more clearly in the diameter measurements (see below). There does appear to be some bias along certain measurement directions despite the different orientations of the hole-plate in the scanner, as in the A1 and V1 directions show, this suggests that these errors are coming from other sources such as the calibration of bidirectional lengths.

Diameter Measurements

The mean diameter measurements for each of the three scan configurations are given in Figure 65. The diameter measurements show a strong dependency on the orientation of the hole-plate; in the vertical orientation a positive error of approximately 8 µm is observed, in the tilted orientation the mean error is less than 1 µm and in the horizontal orientation a negative error is now observed of approximately –8 µm. The negative error in the horizontal orientation is most probably caused by the beam hardening effect, as demonstrated in previous studies [91], beam hardening leads to a dilation of material i.e. holes would appear smaller. The reason for the apparent positive errors of the hole diameters measured in the vertical direction is less clear, especially as beam hardening will still be present in this orientation. This 'erosion' effect in the vertical orientation is studied further within Chapter 5.

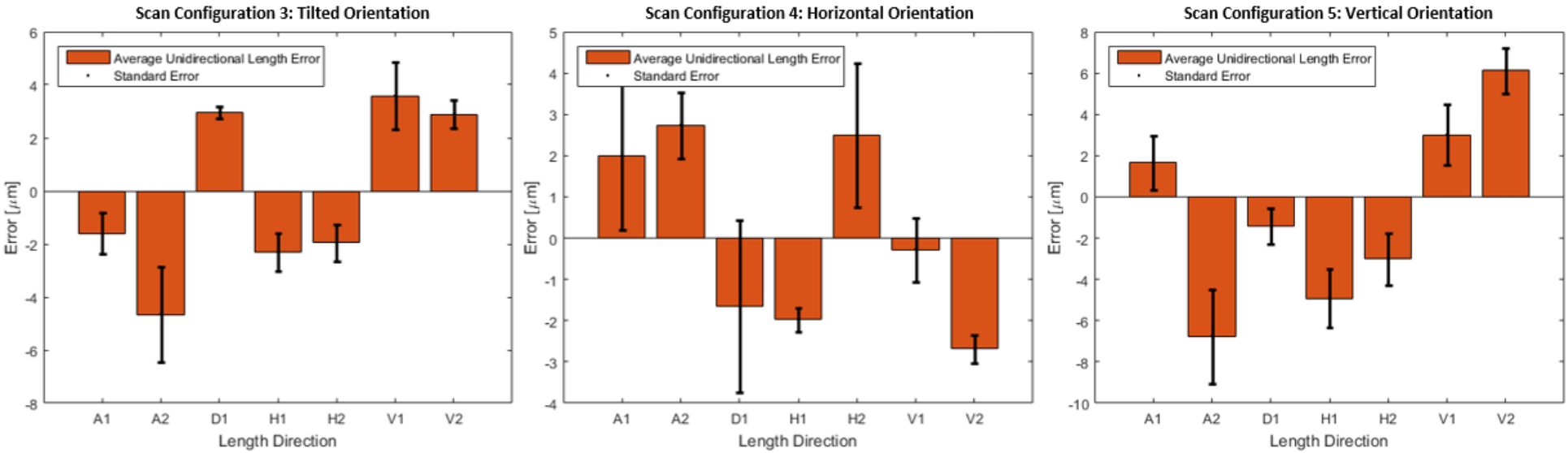

Figure 63. Mean unidirectional length error of each of the five hole-pairs along each length direction. Figures created in MATLAB ver. R2019a.

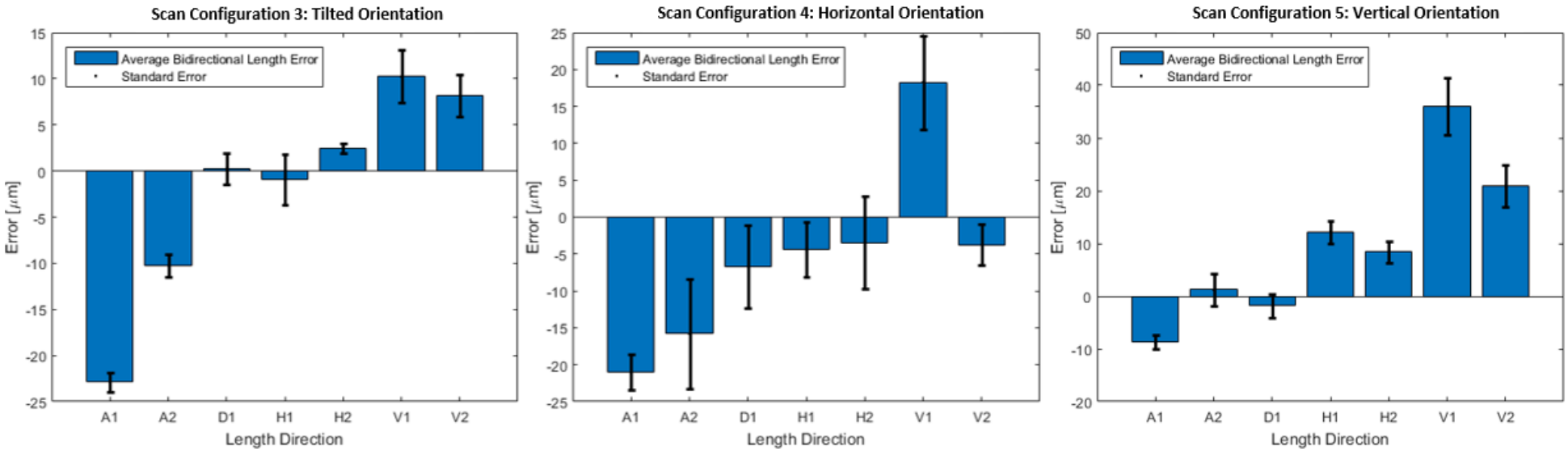

Figure 64. Mean bidirectional length error of each of the five hole-pairs along each length direction. Figures created in MATLAB ver. R2019a.

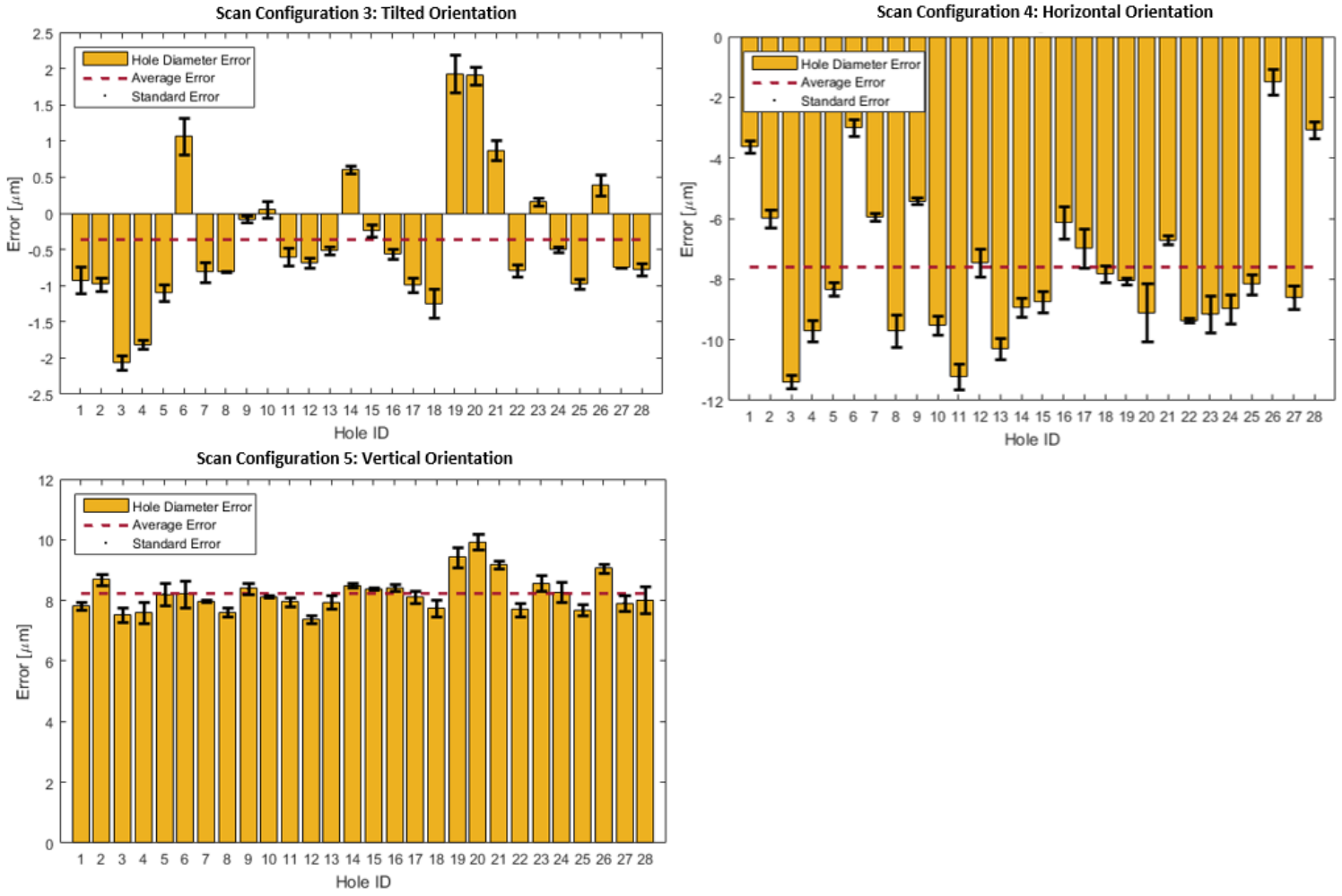

Figure 65. Hole diameter errors for scan configurations 3,4 and 5. Figures created in MATLAB ver. R2019a.

4.3.4 Part 3: Influence of Magnification

The third part of the hole-plate results relate to the measurements obtained from scanning the workpiece at different geometric magnifications as given in Table 8. Changing the geometric magnification influences the resolution of the scan and the angle of the intersecting rays; a lower magnification should reduce the influence of Feldkamp effects. The voxel size for magnifications of 4, 3 and 1.5 were 50 µm, 66.67 µm and 133.33 µm respectively.

Table 8. Scanning strategy for each measurement. At each of the scan configurations, three repeated measurements are performed.

ID	X-ray CT System	Orientation	Geometric Magnification
Part 3			
Scan Configuration 5	450 LC	Vertical	4
Scan Configuration 6	450 LC	Vertical	3
Scan Configuration 7	450 LC	Vertical	1.5

Grey-scale Profiles

The grey-scale profiles from a single scan on each of the systems is compared in Figure 66. The grey-scale profiles are quite similar for the three scan configurations taken at different magnifications, this is expected as the attenuation properties do not depend on the magnification. The only noticeable difference is the noise; a lower magnification appears to reduce noise, this is due to a larger voxel size and therefore image noise is averaged out.

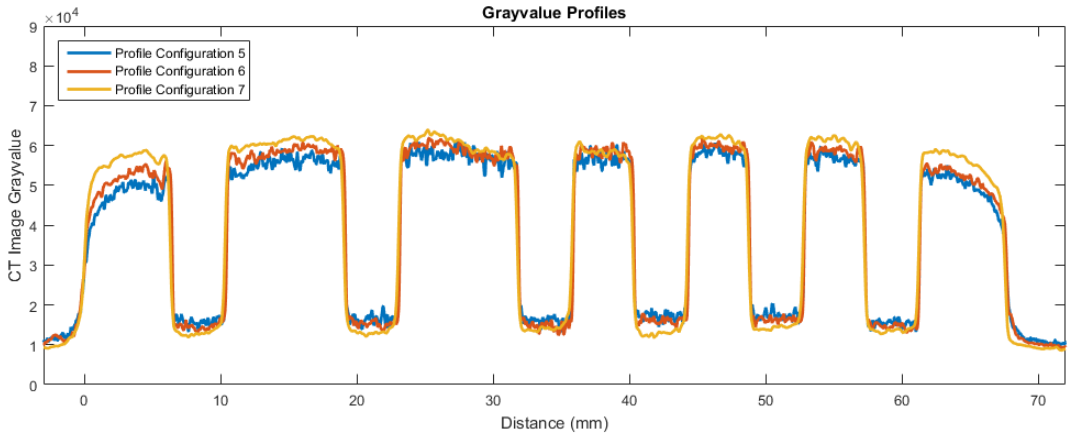

Figure 66. Grey-scale profile of three CT data sets from scan configuration 5, 6 and 7. Figure created in MATLAB ver. R2019a.

Unidirectional Lengths

The mean unidirectional length measurements for each of the three scan configurations are given in Figure 67. The unidirectional length measurements are relatively small with no clear influence of the scan magnification on the error. In fact the highest resolution scan, configuration 5, appears to indicate the largest error. The reason for this may be due to the stability of the system during data acquisition, as vibrations and movement have a larger effect on the results as they are amplified by the geometric magnification factor.

Bidirectional Lengths

The mean bidirectional length measurements for each of the three scan configurations are given in Figure 68. The bidirectional length measurements at different magnification show a clear positive bias. This bias is also observed in the vertical orientation for measurements in part 2. This erosion effect now appears to be correlated with the magnification factor. This is more easily seen in the diameter measurements as discussed below.

Diameter Measurements

The mean diameter measurements for each of the three scan configurations are given in Figure 69. The diameter measurements confirm this positive error, or apparent erosion of material, enlarging the holes. This erosion is stronger for lower resolution

scans with quite a significant mean error in diameter of 20 µm in scan configuration 7. These results are interesting but the origin of this erosion effect is not understood. The reduction of the voxel size appears to cause a systematic error in the hole diameter. The reduced voxel size can be thought of applying a smoothing filter to the data – this may give an indication of the cause of these effects.

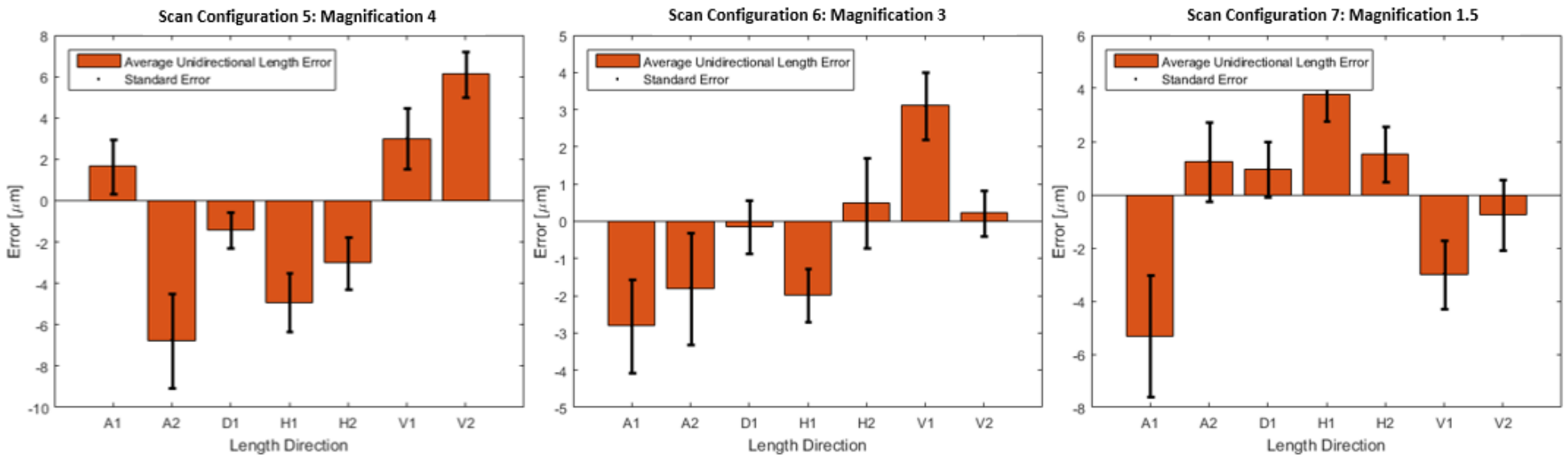

Figure 67. Mean unidirectional length error of each of the five hole-pairs along each length direction. Figures created in MATLAB ver. R2019a.

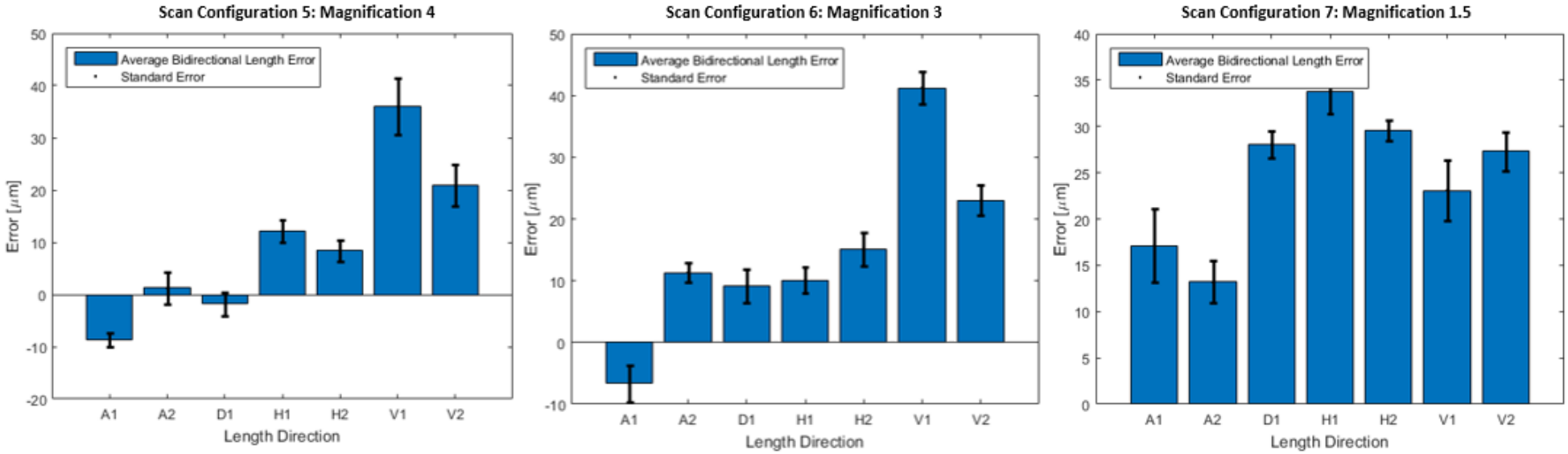

Figure 68. Mean bidirectional length error of each of the five hole-pairs along each length direction. Figure created in MATLAB ver. R2019a.

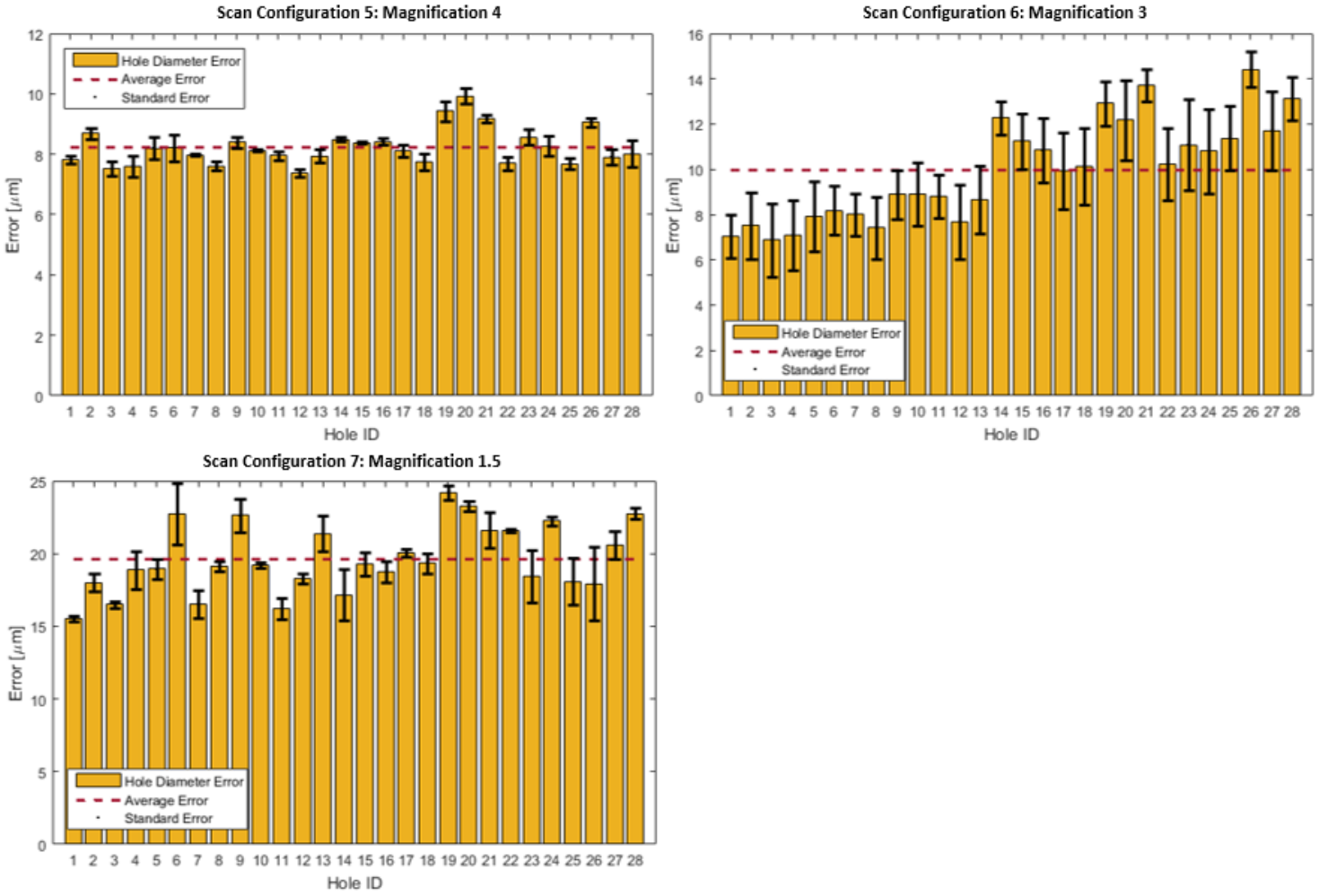

Figure 69. Hole diameter errors for scan configurations 5, 6 and 7. Figures created in MATLAB ver. R2019a.

4.3.5 Part 4: Influence of Beam Hardening Correction

The fourth part of the hole-plate results analyse the measurements obtained by applying different beam hardening corrections to the data. For this part of the results, the data acquired using a single scan configuration, number 5, is used (Table 9). Three different beam hardening correction pre-sets were applied to the projection data and then reconstructed.

Table 9. Scanning strategy for each measurement. At each of the scan configurations, three repeated measurements are performed.

ID	X-ray CT System	Orientation	Geometric Magnification
Scan Configuration 5	450 LC	Vertical	4

Grey-scale Profiles

The grey-scale profiles from a single scan on each of the systems is compared in Figure 70. The grey-scale profiles show clear variations between the three data sets. The cupping effect is observed when beam hardening correction 1, the uncorrected data, is applied. This cupping is reduced by applying correction 2 and is reversed when applying correction 3, suggesting over correction for the beam hardening effect. Another effect of applying beam hardening correction is to reduce the contrast and signal-to-noise ratio.

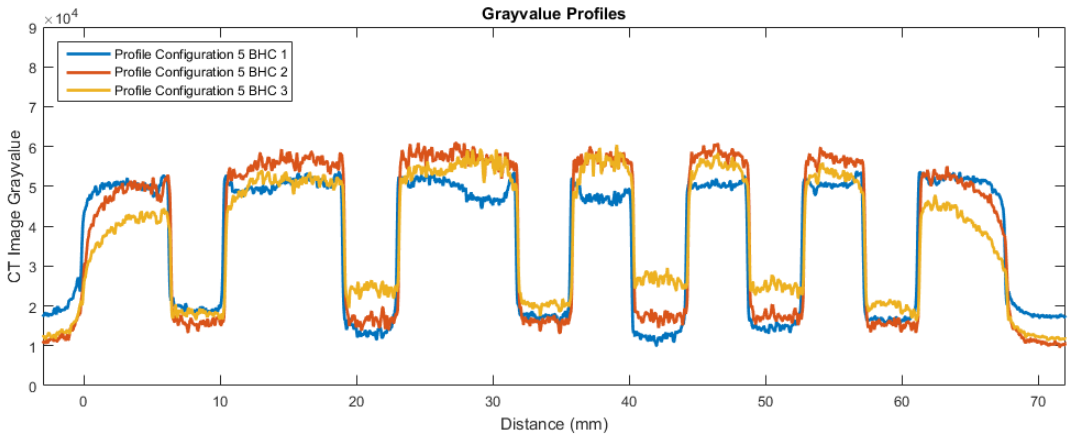

Figure 70. Grey-scale profile of three CT data sets from scan configuration 5 with beam hardening correction pre-sets 1, 2 and 3 applied. Figure created in MATLAB ver. R2019a.

To better illustrate the effect of the beam hardening corrections on the data, three cross sections are shown in Figure 71. Here it is possible to see the variations in grey-scales caused by the beam hardening effect.

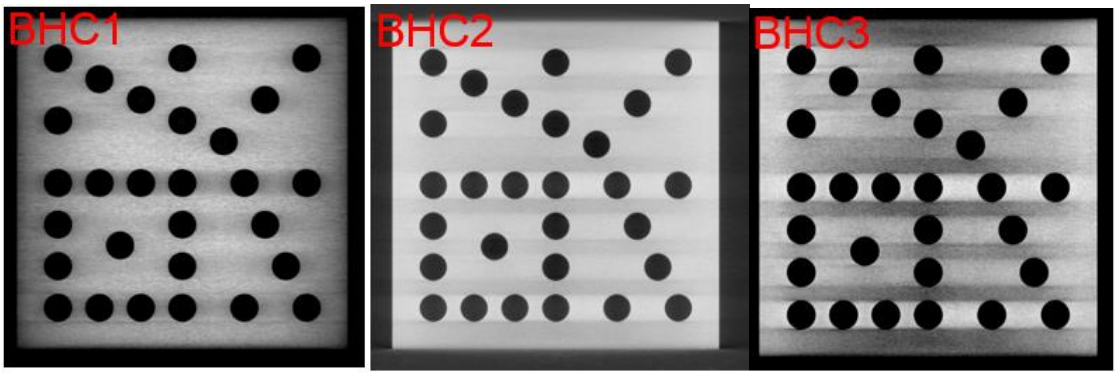

Figure 71.Cross-section of hole-plate CT data with stretched contrast to see beam hardening artefacts.

Unidirectional Lengths

The mean unidirectional length measurements for each of the three scan configurations are given in Figure 72. The unidirectional lengths are, as expected, mostly unaffected after applying the different beam hardening corrections. This is due to centre-to-centre distances being independent of systematic surface errors.

Bidirectional Lengths

The mean bidirectional length measurements for each of the three scan configurations are given in Figure 73. The bidirectional length measurements vary quite significantly with the different beam hardening corrections. The bidirectional lengths seem to increase as a stronger beam hardening correction is applied, this systematic behaviour is more apparent when considering the hole diameters.

Diameter Measurements

The mean diameter measurements for each of the three scan configurations are given in Figure 74. The diameter measurements again show a clear trend when applying the beam hardening corrections, BHC1 is most affected by beam hardening and results in a slight negative mean error. After applying the second beam hardening correction, BHC2, a positive error is now recorded. Further erosion of the edge is observed when applying

BHC3. As beam hardening is known to cause dilation of edges, it is therefore expected that over-correction will lead to erosion of edges. This may be the reason for the observed positive errors, this is investigated further in Chapter 5.

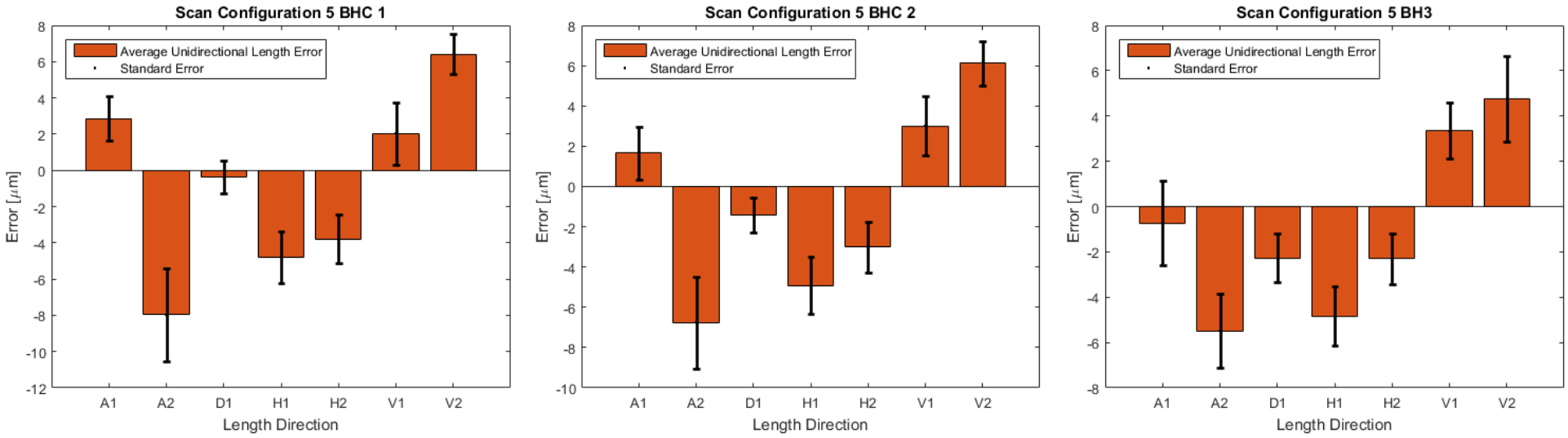

Figure 72. Mean unidirectional length error of each of the five hole-pairs along each length direction. Figures created in MATLAB ver. R2019a.

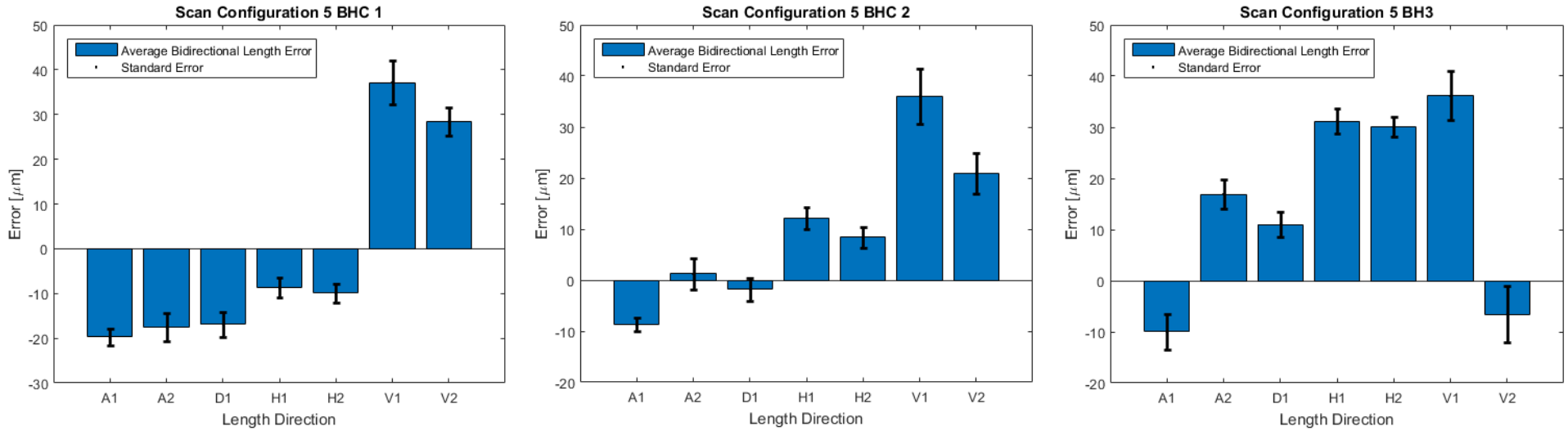

Figure 73. Mean bidirectional length error of each of the five hole-pairs along each length direction. Figures created in MATLAB ver. R2019a.

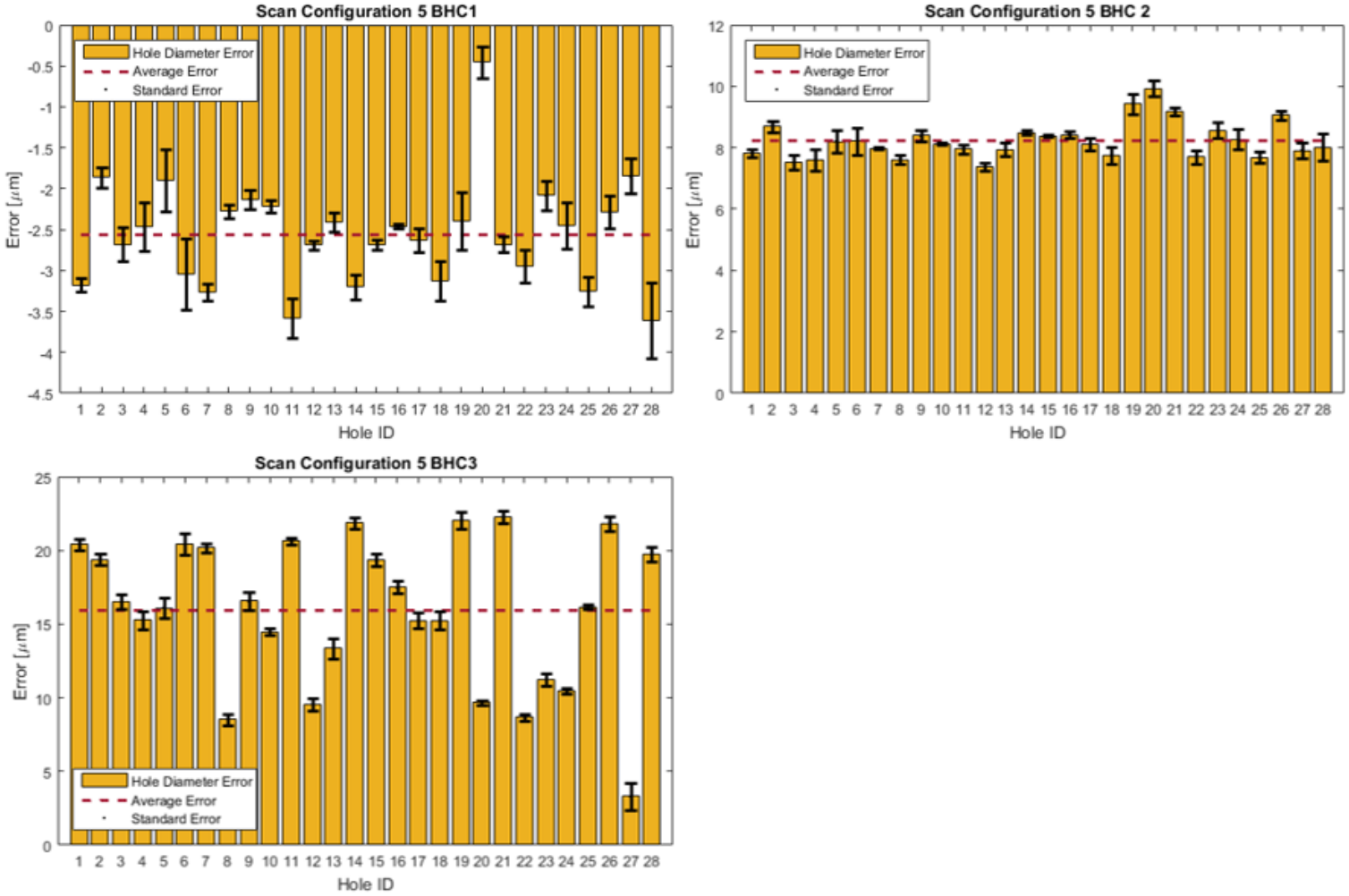

Figure 74. Hole diameter errors for scan configuration 5 with beam hardening corrections 1, 2 and 3 applied. Figures created in MATLAB ver. R2019a.

4.3.6 Part 5: Influence of Image Filters

The final part of the hole-plate results analyse the measurements obtained from applying a Gaussian smoothing filter to the reconstructed CT image. A 5x5x5 operator and a 9x9x9 operator is applied in VG Studio MAX 2.2 to one of the repeated data sets, scanned in configuration 5 as given in Table 10. Note that the bidirectional length measurements were not considered in this section as the diameter measurement have consistently shown clearer trends in the data.

Table 10. Scanning strategy for each measurement. At each of the scan configurations, three repeated measurements are performed.

ID	X-ray CT System	Orientation	Geometric Magnification
Scan Configuration 5	450 LC	Vertical	4

Grey-scale Profiles

The grey-scale profiles from a single scan on each of the systems is compared in Figure 75. The Gaussian filter is a low-pass filter, preserving lower frequency signals, commonly applied to reduce the influence of image noise. As expected the filter has reduced the high-frequency noise from the image. There are no other clear influences of the filter on the grey-scale profiles.

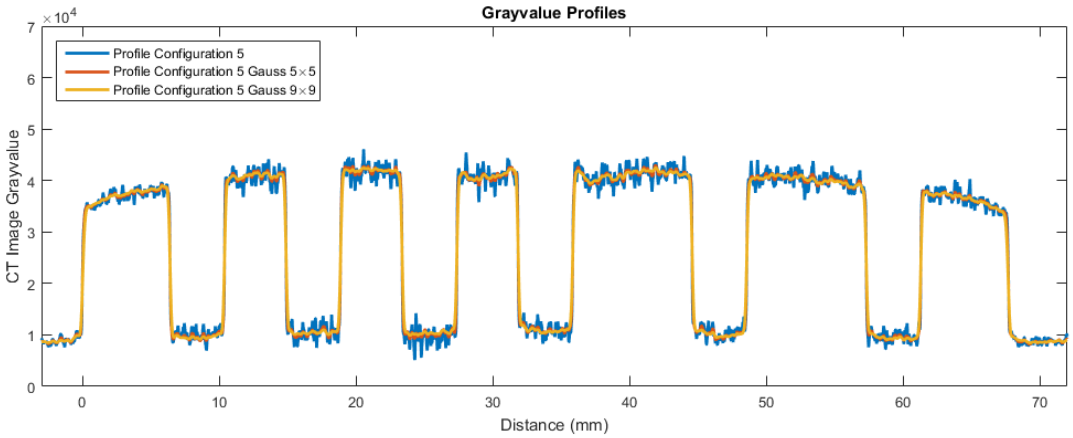

Figure 75. Grey-scale profile of one CT data from scan configuration 5 with varying levels of Gaussian smoothing. Figure created in MATLAB ver. R2019a.

Unidirectional Lengths

The mean unidirectional length measurements for each of the three scan configurations are given in Figure 76. The application of the image filters to the data has very little influence on the unidirectional lengths in general. This is to be expected as random noise or global surface offset is unlikely to influence the extraction of centre-to-centre measurements.

Diameter Measurements

The Gaussian filtering of the data has greatly influenced the measurements of the hole diameters however, as shown in Figure 77. The mean edge error has decreased as a result of the filtering. The filtering has caused dilation of the material, leading to smaller holes. The dilation effect is however non-uniform and appears to be greater for specific holes. The deviation of each hole after filtering is illustrated in Figure 78. It is seen that the holes closer where the vertical centre line is located are more influenced by the filter. As the scan data is taken from the hole-plate in the vertical orientation, this line represents the holes that are measured with the most hardened X-rays. It is noted that beam hardening artefacts are well known to cause dilation of edges, this appears to be exaggerated when applying Gaussian filters. This suggests that a combination of edge smoothing and beam hardening is responsible for the edge dilation effect.

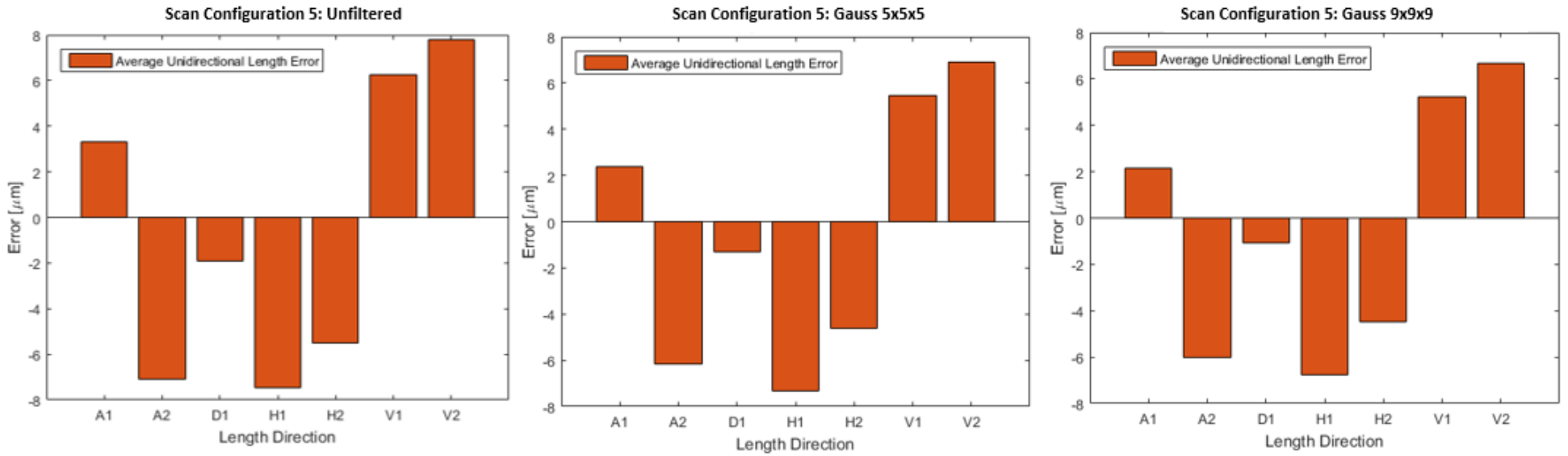

Figure 76. Mean unidirectional length error of each of the five hole-pairs along each length direction. Figures created in MATLAB ver. R2019a.

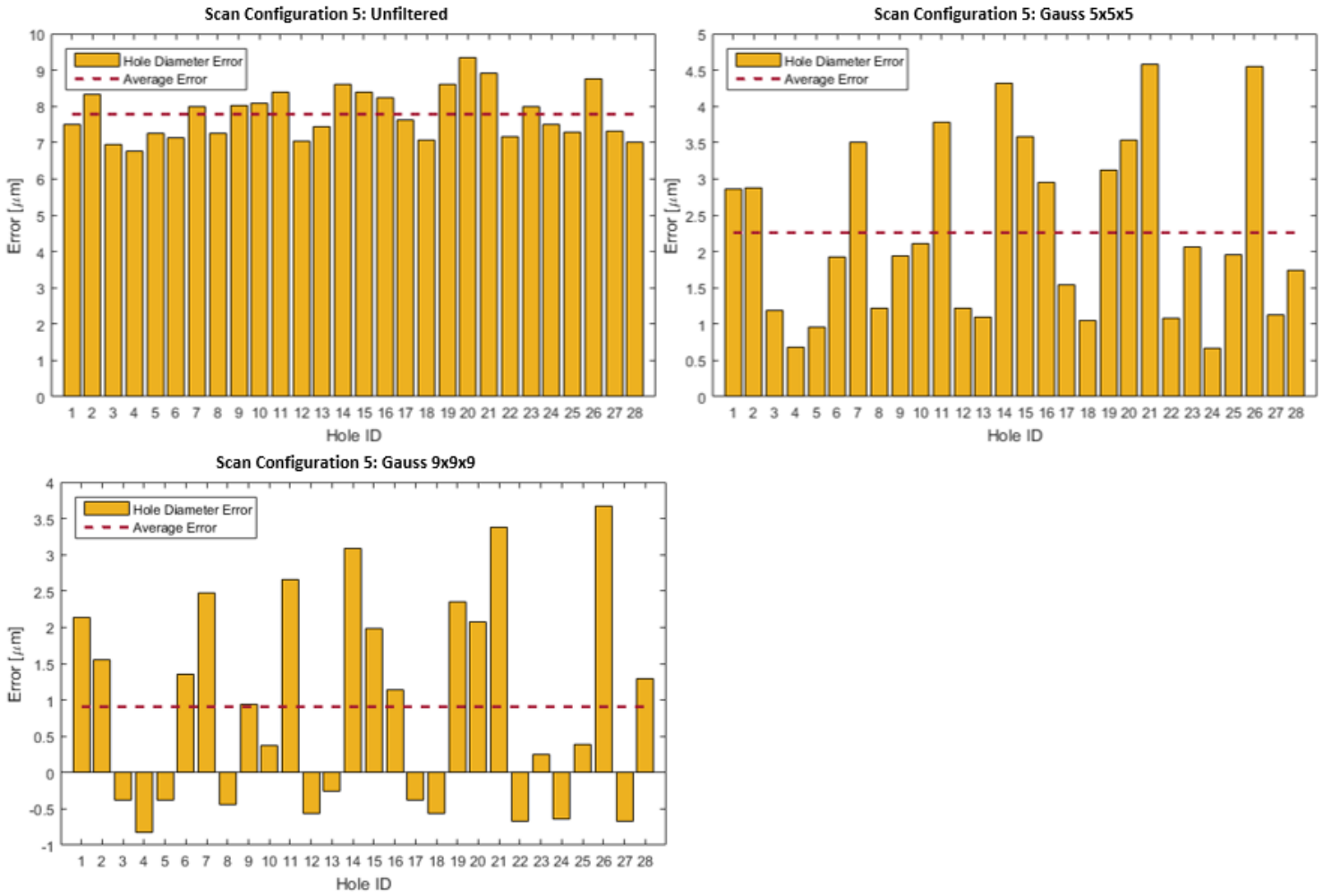

Figure 77. Hole diameter errors for scan configuration 5 with varying levels of Gaussian smoothing. Figure created in MATLAB ver. R2019a.

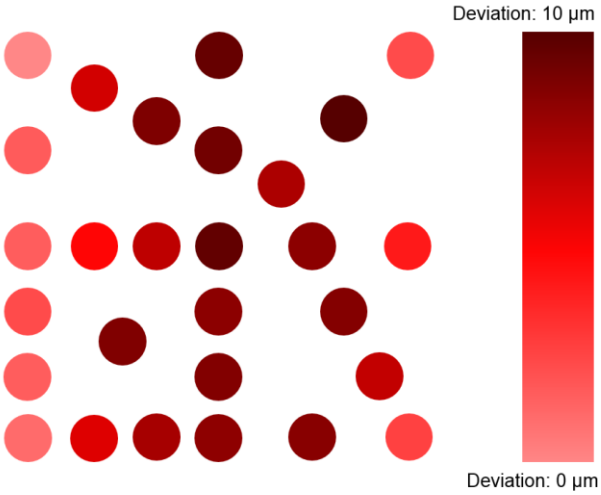

Figure 78. Colour plot of relative deviation of hole diameter after filtering with the 9x9 Gaussian filter.

4.4 Chapter Summary

This chapter has empirically compared three industrial X-ray CT systems in the context of dimensional measurement, most notably a comparison of a metrology purposed system to a conventional system. This work also considered the influence of geometrical magnification, part orientation, beam hardening correction and the effect of applying smoothing filters to the post reconstructed data. The later influence had not been explicitly investigated in previous works. A number of novel findings were therefore observed from this experimental work.

The first part of the results compared near-identical measurements of the hole-plate on three different industrial CT systems. The main findings from this showed that the most significant error source on the 'standard' systems were associated with the global scale length, the XT H 225 ST recorded the largest scale errors of approximately 0.1% when using the calibrated artefact as a reference (Figure 56), this showed that even without moving the manipulator, fluctuations in the system are present and can affect the geometric magnification. In this case it is most likely caused by temperature changes during operation leading to thermal expansion of the X-ray tube and gantry. Further work would be needed to confirm this, however, much research has already been published on this topic so it is not considered advantageous to pursue this further. After correction of the global scale length, using the calibration data directly, the dimensional measurement results were comparable between the three systems. Unidirectional,

centre-to-centre, lengths between hole pairs recorded the lowest errors between +/- 5 µm. This shows that for this type of measurand, using metrology specific hardware, X-ray CT has the potential to measure with the accuracy equivalent to some laboratory CMMs. However, as expected, when measurement are dependent on the surface determination, larger errors were recorded. This illustrates the main barrier to X-ray CT metrology. The subsequent experimental results also highlight how a large number of factors can influence the determination of edges in X-ray CT data.

The second part of the results compared the measurements of the hole-plate in different orientations during the scan. This appeared to have little effect on the unidirectional lengths, although the smallest errors were recorded in the horizontal plane and the largest in the vertical plane. This is an interesting result especially as in the horizontal position, the X-rays must penetrate through significantly more material. This suggests that material influences are not critical for these measurands. Conversely, the orientation of the hole-plate makes a large difference to the bidirectional and hole diameter measurements. By interpolating the result from the three positions, it appears that as the hole-plate is rotated from the horizontal to the vertical plane, the apparent hole diameter increases. A negative error is recorded in the horizontal position and a positive error is recorded in the vertical position. The negative error is most likely explained by the beam hardening effect; this is well known to cause dilation of edges and therefore, holes should appear smaller. The reason for the positive error in the vertical position is not known however, this erosion of the edge has not been reported previously.

Edge erosion is again recorded in the third part of the results, where the hole-plate is scanned in the vertical orientation at three different magnification positions. As the geometric magnification is reduced, the erosion of the edge is exaggerated. This is an interesting result as it suggests that the observed edge erosion is not due to material or workpiece influences and may in fact be related to the resolution. The geometric magnification appears to have less effect on the unidirectional lengths, although the largest errors are observed at the highest magnification, this may be due to reduced image noise that result from the larger effective pixel size.

The influence of beam hardening on the hole-plate measurements is also recorded in the fourth part of the results. Different beam hardening corrections were applied to a single data set and the measurement results were compared. The effect of the beam hardening corrections is to compensate for the non-linear attenuation of X-rays, known as linearization. When applying these corrections to the same data set, before reconstruction, the influence of the beam hardening on dimensional measurements is directly observed. As expected, the unidirectional lengths were largely unchanged by these corrections. It is found that correction of beam hardening reversed the dilation effect, as expected, it is also observed that overcorrection lead to erosion of edges.

The final part of the results quantified the influence of applying a Gaussian smoothing filter to one of the data sets, post reconstruction. This is a common post processing step used to reduce image noise. It is expected that this filter would reduce the influence of image noise but preserve position of the edge. The results however show that the filter lead to dilation of edges, similar to beam hardening. A more important observation is that the deviation appeared to depend on the location of the holes within the plate, finding that the deviations caused by the filter are larger closer to the centre-line of the plate. This suggests that the dilation is linked to beam hardening. The effect of filtration on the edges needs to be more carefully considered however to justify these claims. Edge preserving filers may be more appropriate for dimensional X-ray CT such as median filters, these should be considered in future work.

This experimental work has highlighted how dimensional measurements in X-ray CT can be influenced by a number of generic factors associated with the measurement process. The position and orientation of the workpiece is found to have a systematic influence on the edge position. After correction of the global scale length, it is found that these edge dependent measurements were the most problematic and if these systematic errors were better understood, they could be correctly compensated, improving the accuracy of CT based dimensional measurement. The following chapters therefore attempt to understand the fundamental causes of the observed erosion and dilation effects.

Chapter 5: Erosion and Dilation of Edges in X-ray CT

In Chapter 4, a number of systematic edge effects were observed when measuring the hole diameter of a calibrated hole-plate using a number of micro-X-ray CT systems; these erosion and dilations effects were found to be related to the magnification factor of the scan - related to the image unsharpness - and the orientation of the hole-plate during the scan – related to the beam hardening properties. It is also observed that dilation, attributed to beam hardening, is enhanced when applying a low-pass filter to the reconstructed image. The goal of the following work is to investigate these results further to better understand the apparent relationship between beam hardening and image unsharpness. The influence of beam hardening on dimensional measurements is well known but it is not fully understood how 'cupping' of the data leads to systematic error. This chapter will quantify the combined effect of cupping artefacts and sources of image unsharpness through simulation of X-ray CT data to understand their influence on edge detection. The results of the simulation are then verified through experimental tests on an industrial CT system.

5.1 Background

In Chapter 3, an overview of influence on X-ray CT data is presented, these were divided into two categories; the first type that lead to error in the voxel size determination (unidirectional scale error) and the second type that lead to error in the surface determination (bidirectional). From the results of Chapter 4 it is clear that systematic errors of the first type can be reduced significantly through correction of the voxel size using reference measurements, furthermore no correction is necessary on measurements performed on the dedicated metrology system. Reduction of systematic errors of the second type were less successful and remained the biggest contributor to dimensional measurement error. This chapter therefore focuses on the influences of the edge determination step in X-ray CT, specifically, the influences that are highlighted by the experimental results in Chapter 4.

5.1.1 Cupping Artefacts

Cupping artefacts are most commonly described as a continuous depreciation of the material attenuation coefficient further from the material edges. As previously noted, cupping artefacts are most commonly caused by beam hardening and scattering. How each of these influences leads to cupping artefacts is described in the following sections.

Beam Hardening

According to the Beer-Lambert law the intensity, $I(x)$, observed when a monochromatic X-ray beam passing through a distance, x, in an homogenous material is given by,

$$I(x) = I_0 e^{-\mu x}$$

Equation 62

where I_0 is the initial intensity of the source and μ is the linear attenuation coefficient. This relationship describes the attenuation of a monochromatic source well, however it is noted that the linear attenuation coefficient is not only dependent on the material characteristics but also on the energy of the incident source. Since the X-ray sources of interest are inherently polychromatic, this relationship must be modified to include this energy dependency. An X-ray source consisting of multiple energies will be attenuated at different rates and therefore the spectrum will vary at different penetration lengths. This effect known as beam hardening since an increase in the mean energy of a polychromatic X-ray beam is generally observed as it traverses through a material. Writing the attenuation coefficient as an explicit function of energy $\mu(E)$, the intensity $I(x)$, of a polychromatic X-ray source, $I_0(E)$, at a depth x through a material is therefore,

$$I(x) = \int_0^{E_{max}} I_0(E) e^{-\mu(E)x}\, dE$$

Equation 63

where E_{max} is the maximum energy X-ray generated by the source. For the purposes of tomographic reconstruction, the attenuation value is used as for a monochromatic

source it is linearly proportional to the path length through a homogeneous material, as given in Equation 64:

$$Attn. = -\ln(\frac{I}{I_0})$$

Equation 64

For a polychromatic source, the total attenuation varies non-linearly with path length, this is shown in Figure 79.

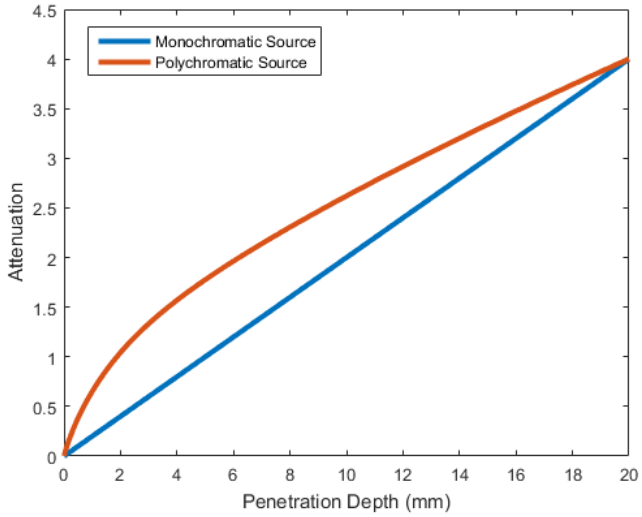

Figure 79. Example of attenuation vs penetration depth plot for a polychromatic and monochromatic X-ray source. Figure created in MATLAB ver. R2019a.

With the assumption of linear attenuation, any material becomes less attenuating as the penetration depth increases. This presents itself as a higher attenuation coefficient at the edges once reconstructed leading to the so called cupping artefacts.

Scattering

Although scattering is described by a complex interaction process, the influence of scatter on reconstructed CT data can be demonstrated using a simple approximation. It can be assumed that scattered X-rays contribute to a constant additional signal to image. By applying a constant offset to the all intensity values and calculating the attenuation a non-linear relationship can again be observed, as shown in Figure 80, where an offset of 5% of the peak value was used. In contrast to a polychromatic attenuation curve however, the scatter curve behaves more linearly at the shorter penetration depths.

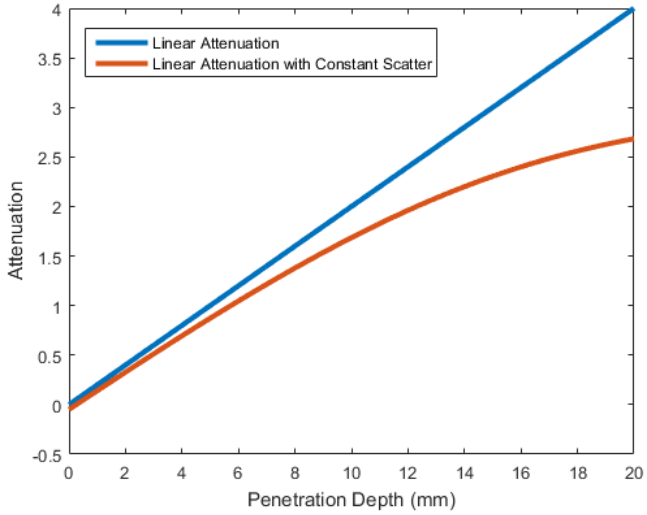

Figure 80. Plot of total attenuation vs penetration depth with and without scatter signal. The additional scatter signal is 5% of the peak intensity. Figure created in MATLAB ver. R2019a.

5.2 Edge Blurring

It is noted by Lifton in [91], that cupping artefacts such as those caused by beam hardening do not physically change the position of the edge but influence edge determination, leading to systematic error. However, it is not conclusive why these artefacts lead to the observed measurement error although it is argued that edge contrast is responsible. It is found via experiment that the systematic errors observed due to cupping artefacts were enhanced when applying a Gaussian smoothing filter to the data. Cupping artefacts however have been shown to change the edge profile [91], this may lead to the observed error when applying the smoothing filter.

5.2.1 Edge Dilation

It is expected that when applying a Gaussian filter to an ideal edge, the edge position is preserved, the previous chapter showed that in the presence of cupping artefacts, systematic errors can occur when applying smoothing filters to the reconstructed images. To demonstrate this, ideal and cupped edge profiles ware modelled and the edge position recorded before and after applying a Gaussian operator.

An Ideal edge is therefore defined as,

$$Y(x) = \begin{matrix} M & x <= r \\ B & x > r \end{matrix}$$

Equation 65

Where Y is the grey-scale value of a reconstructed edge, M is the material linear attenuation co-efficient, B is the background attenuation co-efficient and r is the edge position. A cupped edge is defined in Equation 66 as:

$$Y(x) = \begin{matrix} M & & x <= 0 \\ M + f(x) & x > 0 \ \ and & x <= r \\ B & & x > r \end{matrix}$$

Equation 66

Where $f(x)$ is a function that describes the cupping profile in Equation 67,

$$f(x) = h\mathrm{e}^{-(\mathrm{r}-\mathrm{x})}$$

Equation 67

And h is the maximum height of the peak. These edges are smoothed using a Gaussian filter and plotted in Figure 81 along with the edge gradient function, calculated using the 1D Prewitt kernel in Equation 68.

$$\nabla_x = [-1 \quad 0 \quad 1]$$

Equation 68

For the case of the ideal edge, the point of maximum gradient is unaffected by the smoothing filter. The edge position shifts however for the case of a cupped edge when the filter is applied. This can be explained by considering the gradient of a cupped edge before smoothing – the gradient of the cupping artefact opposes that of the edge and as this is smoothed it mixes with the edge gradient and causes the point of maximum gradient to shift outwards. This is an important result as smoothing filters are commonly applied to CT data for noise reduction. Smoothing these edges may therefore lead to dimensional measurements error if there is edge cupping. This dilation effect is in

agreement with previous research [8-12] however this has not previously been associated with image blurring. It is noted however that the effect of the source diameter is not to smooth the reconstructed image but to smooth the pre-reconstruction projected intensity images. In other words the blurring occurs in the intensity images collected by the detector and several steps are then performed before the reconstructed image is determined. In previous work, the effect of the source size has not been considered mainly due to the small source sizes that can be achievable on low power systems which are suitable for plastics and light metals. However on higher power systems the source diameter size may have a considerable influence on the measurement results. It is well understood that a finite source diameter will lead to unsharpness of the projected image which may therefore influence the position of edges.

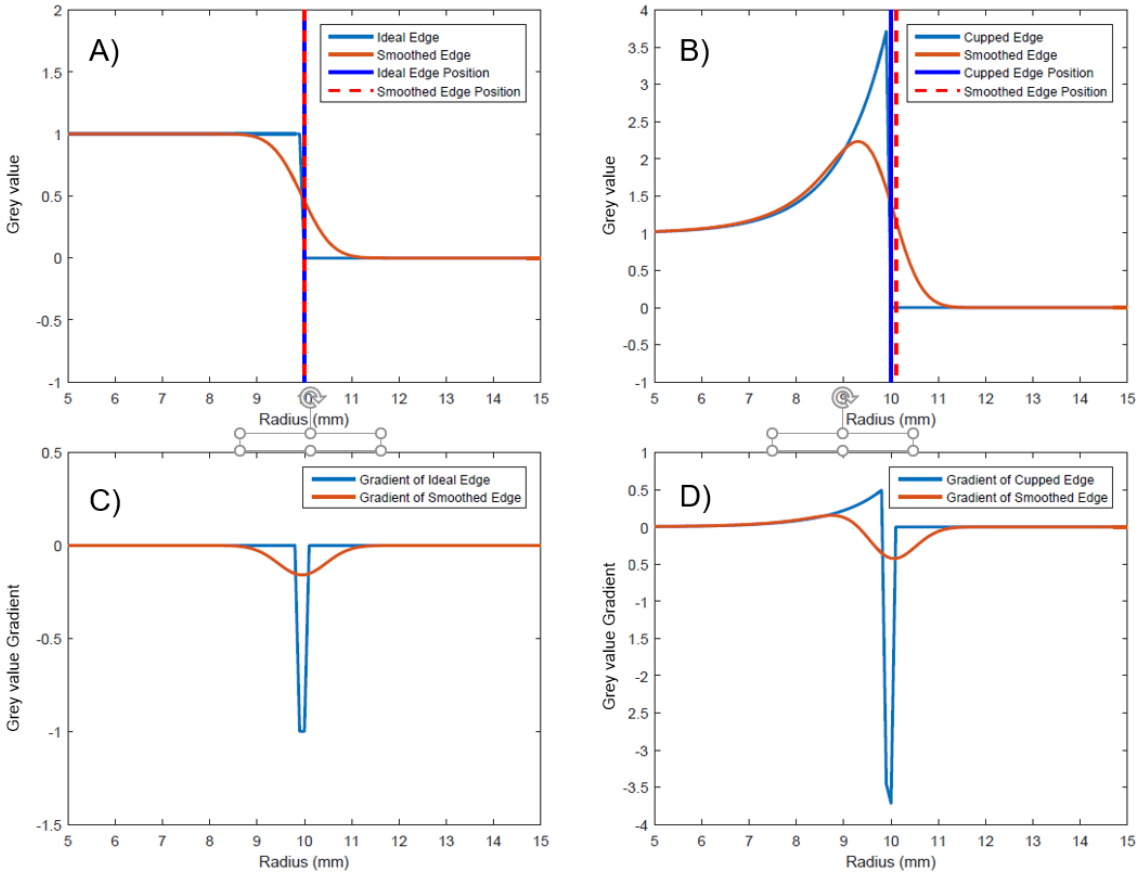

Figure 81. A demonstration of the influence of smoothing edges. The position of maximum gradient is unaffected by smoothing with a Gaussian filter (A and C), however the maximum gradient of a cupped edge is shifted when a Gaussian filter is applied (B and D). Figures created in MATLAB ver. R2019a.

5.2.2 Edge Erosion

In the previous example, it is demonstrated that smoothing of cupped edges can lead to systematic dilation of the edge gradient, it is important to note that other sources of image unsharpness, such as from a finite source, directly influence the radiographic projection images before the reconstruction step. By again considering the gradient of an edge, the influence of blurring on the projection images can be studied. Figure 82 gives the gradient of an intensity value before and after Gaussian smoothing is applied (as would be measured by the detector). As before the position of maximum gradient is unaffected by the smoothing operation. For the purposes of CT reconstruction however, the X-ray attenuation is first calculated from the intensity values (see Equation 64). It is observed that the result of this operation can influence the position of the maximum edge gradient when smoothing is first applied to the intensity image. A systematic shift of the maximum gradient, given by the position of the peaks, is observed leading to an 'erosion' of the edge.

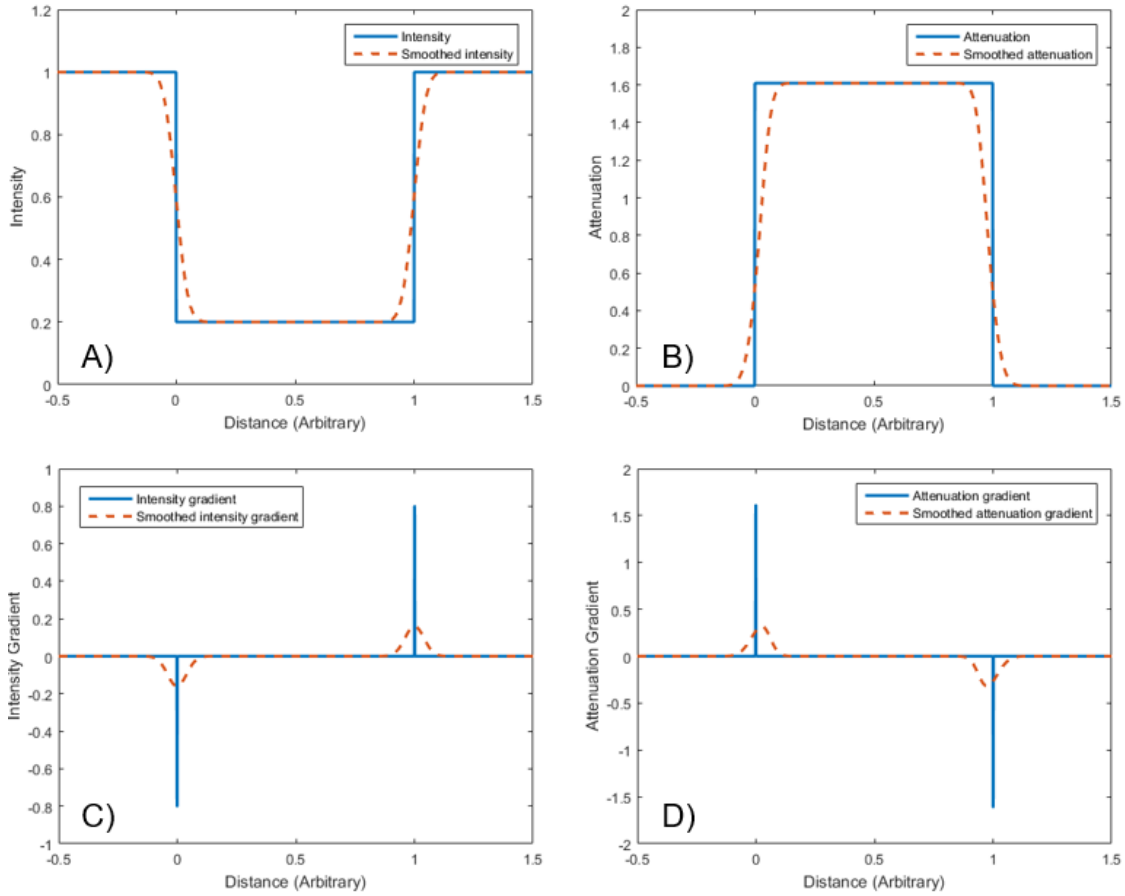

Figure 82. Demonstration of how erosion of edges can occur in X-ray CT data. A) Intensity plot of a parallel ray projection of a square object of uniform thickness. B) Attenuation of A. C) Gradient of A. D) Gradient of B). Figures created in MATLAB ver. R2019a.

It has been demonstrated that edge smoothing can result in both dilation and erosion of edges subject to whether the smoothing is applied before or after the reconstruction step. It is not clear however how edges are affected when both beam hardening and blurring are considered simultaneously. It is therefore proposed that a more complex model be tested using simulation of the beam hardening effect and the influence of a finite source size.

5.3 Simulation of X-ray CT Measurements

Through simulation, the effect of individual influence factors, such as beam hardening, on the edge position can be quantified. A methodology is proposed for modelling the acquisition of X-ray projections, reconstruction, edge detection and dimensional measurement extraction.

5.3.1 Modelling the X-ray Spectrum

The beam hardening effect is achieved through simulation of a polychromatic source and the attenuation properties of the workpiece. The beam hardening effect for a 400 kV X-ray source spectrum is modelled which is attenuated by an iron workpiece. Iron is chosen as the workpiece material in order to exaggerate the cupping artefacts due to its relatively high density. Experimental data is used to model the X-ray attenuation of iron, for the workpiece, and copper, for the source filtration. This is obtained from the NIST online database [13], as shown in Figure 83. 400 kV was chosen in this instance to enhance the beam hardening effects associated with a broad spectrum, this could also be matched experimentally by the XT H 450 LC system.

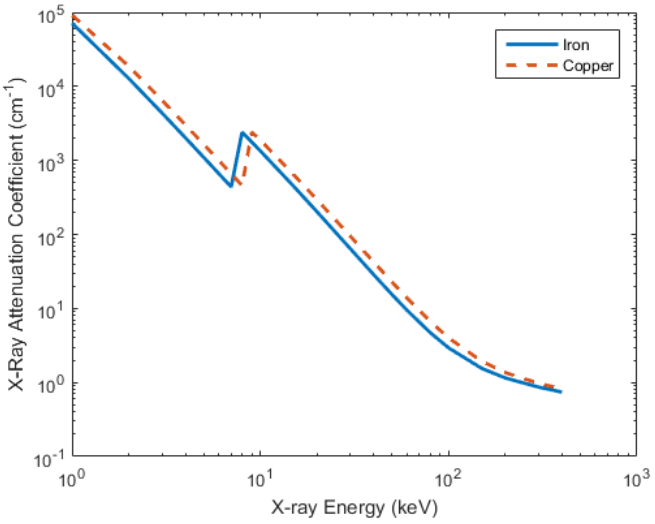

Figure 83. X-ray attenuation coefficient of iron and copper for X-ray energies from 1 keV to 400 keV. Data from [45]. Figure created in MATLAB ver. R2019a.

The X-ray source spectrum is simulated using a radiographic simulation package, aRTist [138]. The source parameters are given in Table 11. The X-ray spectrum generated is plotted in Figure 84.

Table 11.Parameters used in simulation of source spectrum.

Parameter	Value
Target material	Tungsten
Target thickness	1 mm
Target angle	21°
Acceleration voltage	400 kV
Window material	Aluminium
Window thickness	5 mm

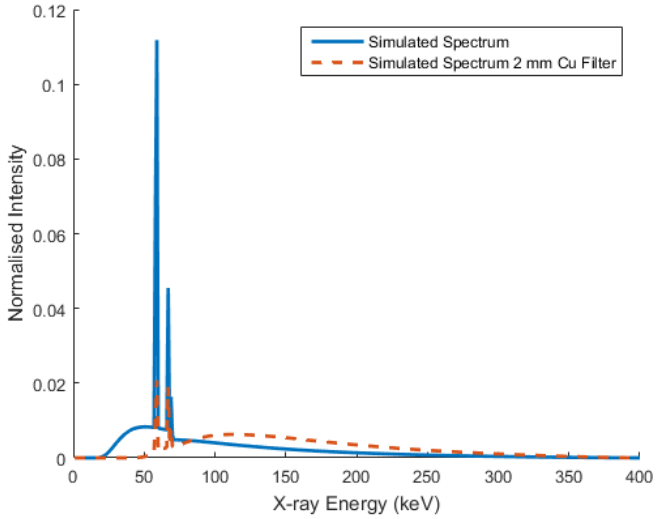

Figure 84. Simulated X-ray spectrum using aRTist simulation software [14] before and after filtration with 2 mm of copper. Figure created in MATLAB ver. R2019a.

Using this model for beam hardening, the resulting intensity for a polychromatic source is then determined using Equation 63.

5.3.2 Simulation of Fan beam Projections

In order to investigate the influence of the source diameter size on the results of dimensional X-ray CT, simulation of a fan beam CT scan is performed with various source sizes. The combined influence of the source diameter size and the beam hardening effect is included to understand the relationship between these two factors. Simulation is used to isolate these factors from other potential influence on measurement. The acquisition of fan beam CT projection images of a solid circular disk is modelled through

calculation of the ray paths through the workpiece from the source to each detector pixel. The parameter used in the simulation are given in Table 12.

Table 12. Parameters used in fan beam model.

Parameter	Value
Source-to-detector distance (SDD)	1027.9 mm
Source-to-object distance (SOD)	205.58 mm
Detector width (D)	400 mm
Detector pixel size (P)	200 µm
Number of pixels	2000
Workpiece diameter ϕ	20 mm
Source opening angle θ	22°
Source spacing (S)	5 µm
Sub-pixel spacing (P_s)	40 µm

To simulate the finite size of the X-ray source, multiple point sources were generated at equal spacing along the width of the source diameter as illustrated in Figure 85. The intensity of each source is also weighted to produce a Gaussian profile across the source width with a sigma value of a quarter of the total width.

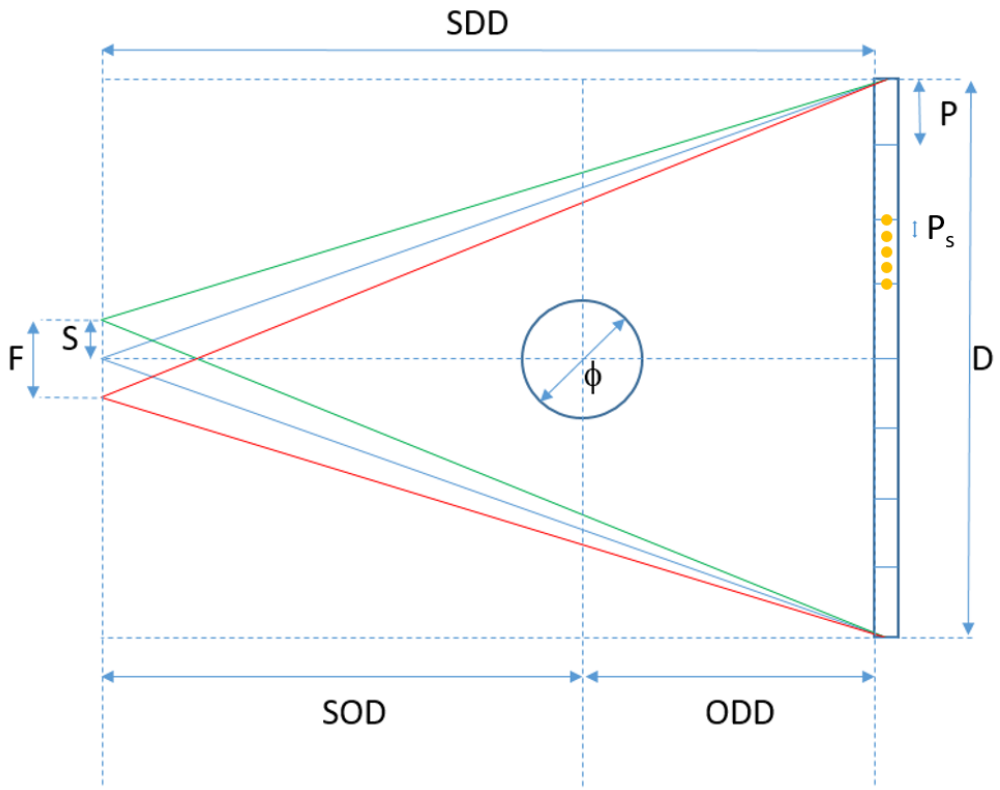

Figure 85. Diagram of fan beam geometry used in simulation. Not to scale.

The fan beam CT data is then simulated by performing the following steps; at each source, ray paths are traced to five equally spaced points within each pixel, this is repeated for each pixel in the detector array. The total path length travelled through the material is then calculated. The ray intensity after attenuation through the workpiece is then calculated. This is dependent on the initial intensity, path length and the energy spectrum of the source. Two source types are used, a single energy or monochromatic source and a multi-energy or polychromatic source. (See 5.3.1). The intensity of all rays that reach each pixel are then summed. The X-ray attenuation is then calculated for each pixel using Equation 64. Some examples of the intensity and attenuation images are given in Figure 86 with 0 mm and 0.5 mm source diameter respectively. Despite this however the differences are subtle, these difference become more obvious in the following section after image reconstruction.

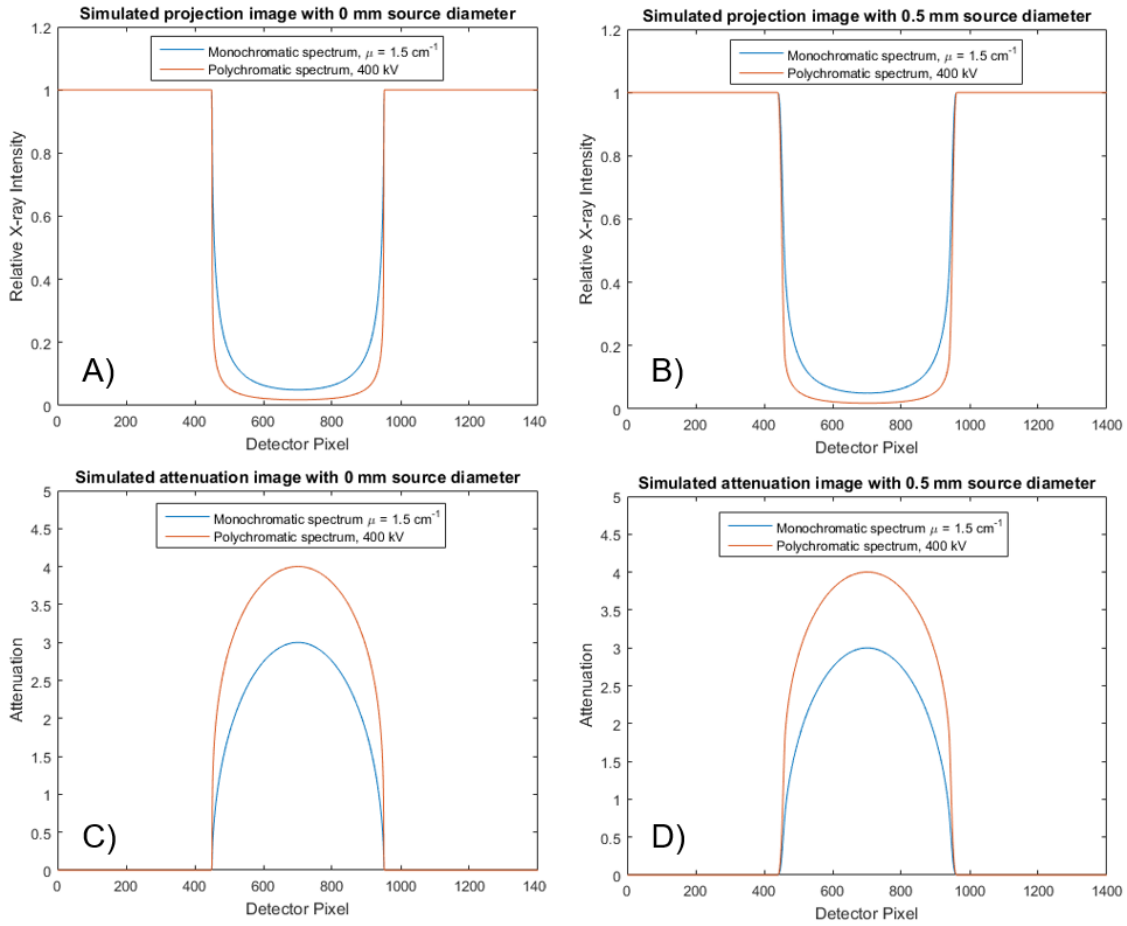

Figure 86. Simulated intensity (A and B) and attenuation (C and D) plots for monochromatic and polychromatic sources with a 0 mm source diameter (A and C) and 0.5 mm source diameter (B and D). Figures created in MATLAB ver. R2019a.

5.3.3 Reconstruction

This set of projection data is then reconstructed using an equidistance fan beam filtered back projection algorithm as outlined in detail in 2.2.4 to generate a 2D cross sectional image; the ramp filter is applied to each projection and a weighted back projection of attenuation values for each pixel along fan beam is performed. This is repeated for each projection angle.

An example of the output of the simulations is given in Figure 87, showing the difference between an ideal scan with a point source diameter and no beam hardening and a scan with a large source diameter and beam hardening artefacts present.

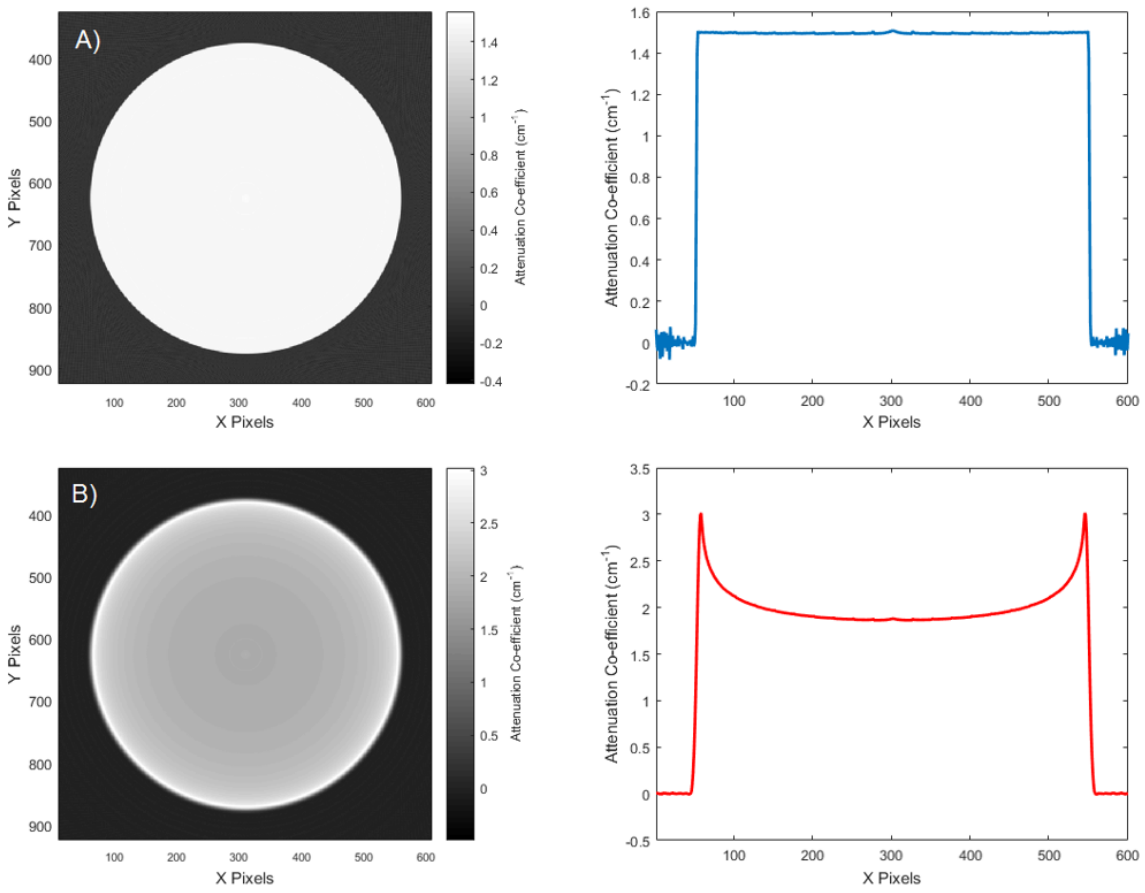

Figure 87. Simulated CT data: A) Reconstructed simulation of monochromatic source with 0 mm source diameter size. B) Reconstructed simulation of polychromatic source with 0.5 mm source diameter. Figures created in MATLAB ver. R2019a.

5.3.4 Edge determination

Diameter measurements of the reconstructed disks are then determined by firstly; taking the edge profile through centre and then calculating the grey-scale value gradient. Next the maxima of the local gradient is used to determine the edges of disk. A quadratic interpolation is then used to determine sub-pixel turning point. This is repeated for 360 equally spaced angles intersecting the centre of the disk. Finally the distance between edge turning points is calculated by fitting a circle using a least squares Gaussian method to determine the diameter. This is a common fitting method used in diameter determination however it should be noted that other methods can be used. The least squares method chooses the diameter than minimises the sum of the squares of the residuals of the all the fitted points. The gradient is calculated using the 1D Prewitt kernel in Equation 68.

5.3.5 Results

The simulated results are given for various source diameters for both monochromatic and polychromatic sources.

Monochromatic Source

Figure 88 shows there is a correlation between the source diameter size and the measured diameter. The effect of a larger source size is to decrease the indicated diameter of the object. It is expected that blurring of the monochromatic edges may influence the position of the edge in this way as demonstrated in 5.2.2.

Another key observation is that the magnitude of the erosion effect is also dependent on the absorption coefficient of the material - more accurately it is dependent on the total attenuation (a higher attenuation coefficient will lead to a larger attenuation for the same path length). The reason for this is the logarithmic operation behaves non-linearly for large differences in the intensity, therefore the erosion effect is stronger for highly contrast edges. This is an important result as it shows that the source diameter size can directly influence the measured position of an edge in X-ray CT. This effect may explain results found in other work [11]. In this paper the authors commented that a systematic negative error is measured for the case of a monochromatic source in their simulations. For the worst case of a 300 μm source diameter, the edge position was found to erode by 8 μm and 35 μm with a maximum attenuation value of 2 and 4 respectively

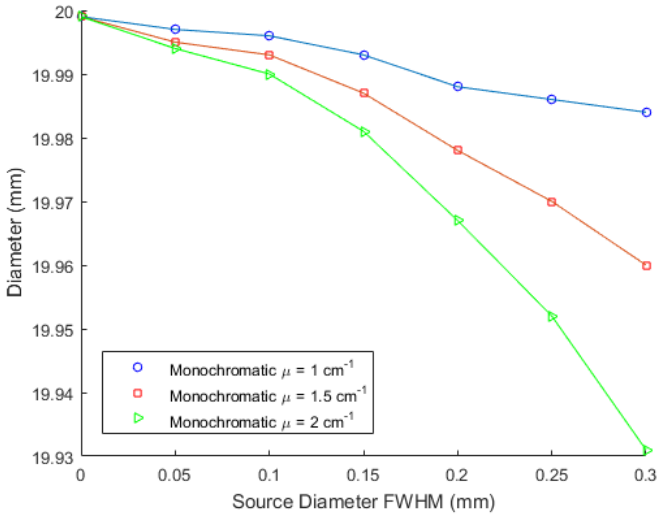

Figure 88. Diameter measurements of simulated data with monochromatic sources of different X-ray energies corresponding to a different attenuation coefficient. Figure created in MATLAB ver. R2019a.

Polychromatic Source

Figure 89 shows a similar trend to the monochromatic results; the erosion due to the source diameter size is the dominating influence as the measured diameter decreases with increasing source size. As noted in the monochromatic results, the erosion effect is also dependent on the total attenuation of the workpiece. In the polychromatic results, this has caused the unfiltered spectrum to be influenced more by the source size. At smaller source sizes however the filtered and unfiltered spectrums record a dilation of the edge, which is greater for a more polychromatic source. As these results are diameter measurements, the error in the edge position is half as large. For the worst case of an unfiltered polychromatic 400 kV source, the edge position was found to dilate by 18 µm and 14 µm when filtered by 2 mm of Cu.

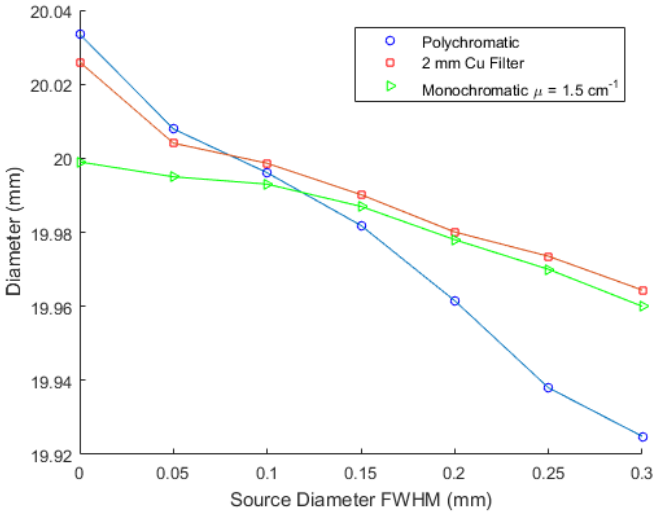

Figure 89. Diameter measurements of simulated data with polychromatic source. Figure created in MATLAB ver. R2019a.

5.3.6 Discussion

The results of the simulation have confirmed the erosion of edges caused by the source diameter size as predicted in 5.2.2. To the knowledge of the author this effect has not been reported previously. The results suggest that the bias is greater the larger the source size or the more attenuating the edge. It is therefore supposed that these errors will more likely be detected on high power X-ray CT systems which tend to have larger source diameters.

The dilation of edges due to cupping artefacts is also observed for small source diameter sizes, however as the source diameter size is increased the dilation effect dominated and negative errors were observed. It is also found that by filtering the source the error due to beam hardening (at small source size) and the error due to source diameter blurring (at large source sizes) is reduced. While the former effect is well known, the reason for the latter effect is that filtration increases the mean beam energy which therefore reduces the overall attenuation. The attenuation is found to be related to the magnitude of the edge erosion. The next step is to confirm that these are real, observable effects by experimenting on an industrial X-ray CT system.

5.4 Experimental Validation

An experimental evaluation is performed to validate the results of the simulation. A steel cylinder, shown in Figure 90, is scanned in an industrial CT scanner in fan beam mode at a constant voltage of 400 kV. A number of scans are performed using a range of source powers and source filtration. The purpose of this is to recreate the simulation results for the polychromatic and filtered spectrums. It is noted that it is not possible to recreate the ideal conditions of the monochromatic source.

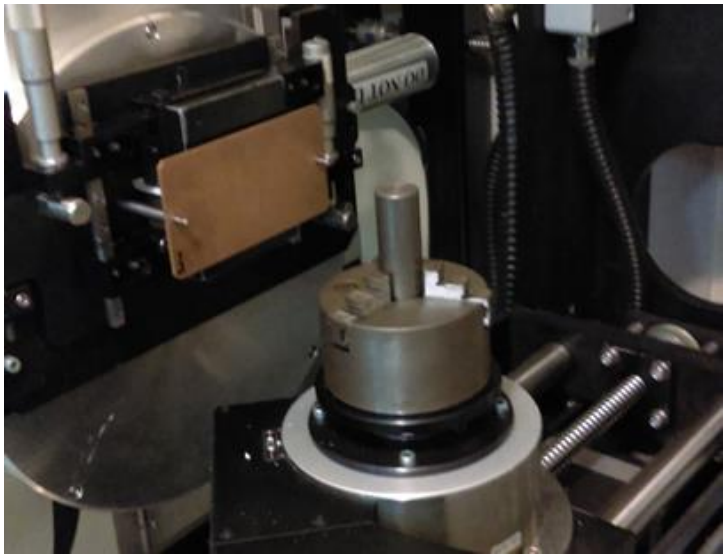

Figure 90. Image of experimental set-up. Two lead collimators were used to create a fan beam.

5.4.1 Methodology

A steel cylinder is scanned using fan beam CT on a Nikon XT H 450 system and the diameter measured. This is achieve using two collimating lead blocks with a small gap for the beam to pass through. 24 scans were completed in total; one for each of the four power setting with and without source filtration, each repeated three times. The scan parameter values are given in Table 13. The purpose of changing the current value is to increase the size of the source diameter without affecting the form of the spectrum. The source spectrum and therefore the beam hardening properties are also controlled using hardware filtration. The source diameter is measured at each of the power settings by fitting a Gaussian profile to an image with a sharp edge contrast. This is achieved by imaging a thin copper plate at multiple angular views and taking the minimum recorded source diameter. Each of the scans are performed at the same magnification which is

calibrated with the ball-bar reference artefact used Chapter 4. This is to ensure any scale errors are minimised so that only the error due to edge influences are measured. Measurement of diameters is performed in VG Studio MAX 2.2 [15] using the exact settings given in Table 3.

Table 13. Parameters used for the fan beam scans of the iron cylindrical workpiece.

Parameter	Value
X-ray CT System	Nikon XT H 450
Magnification	5
Voxel Size	35 µm
Acceleration Voltage	400 kV
Current	125 µA/250 µA/375 µA/500 µA
Source Filtration Material	Copper
Source Filtration Thickness	0 mm/2 mm
Exposure Time	1415 ms
Number of Projections	900

5.4.2 Experimental Results

The cylinder diameter measurements are plotted against the source Full Width at Half Maximum (FWHM) value in Figure 91. The simulation results from Figure 89 are also plotted for comparison accounting for the difference in the cylinder diameter. The experimental results agree with the main trend of the previous simulation results where a larger source diameter leads to an erosion in the diameter measurements of the cylinder. It is noted that there is an 'optimal' source diameter where the influence of beam hardening and source blurring cancel out. The erosion of the real edges are not as large as in the simulation results. One reason for this may be due to scatter in the experimental results. This may reduce the edge contrast and therefore reduce the erosion effect as observed in Figure 88. Overall however these results agree with the findings of this chapter.

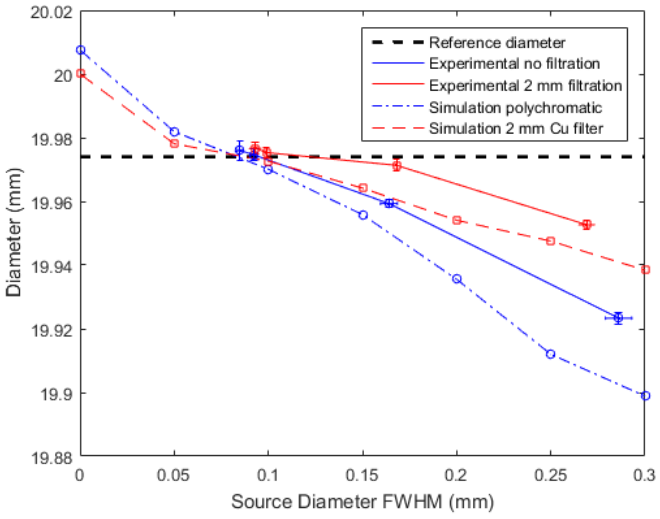

Figure 91. Results of the experimental measurement of the cylindrical workpiece. A simulation is set up with similar parameters for comparison. Figure created in MATLAB ver. R2019a.

5.5 Revisiting the Hole-Plate

In Chapter 4, dimensional X-ray CT measurements were acquired on a calibrated hole-plate artefact. A number of systematic errors were observed when changing the orientation and magnification of the hole-plate and applying beam hardening corrections and image smoothing filters. These systematic errors are observed only on the so called bidirectional lengths; those that are influenced significantly by the edge determination step. Both dilation and erosion of edges are observed when measuring the hole-plate diameters. In this chapter, it is found that erosion of material edges could occur due to blurring of the radiographic intensity images. In light of this new information, the hole-plate measurement result will be analysed to understand if they are consistent with this hypothesis.

5.5.1 Erosion of Edges in the Vertical Orientation

The first set of unexplained results were from the measurements of the hole-plate diameters in the vertical scan orientation as shown in Figure 69. Here there appears to be a correlation between the geometric magnification of the scan and the mean diameter error of the holes. In the beginning of this chapter it is shown that image unsharpness due to a finite source size could lead to edge erosion. Image unsharpness in fan beam and cone beam X-ray CT is related to a number of other factors including

the geometric magnification, detector pixel size, reconstruction filter and also movement of the detector, source or object during capture of the radiographic projections. By considering only the geometric factors effecting unsharpness it is possible to explain the unsharpness of a CT system based on the characteristics of the source and detector. These geometric limitations of the system are analysed in [74] where the effect of the source size, pixel size and geometric magnification are related to the theoretical OTF of the system. In the previous chapter, the effect of the geometric magnification is not considered however it is shown, in Equation 69, that the unsharpness of a projected image due to the source is related to the geometric magnification;

$$U_S = \frac{S(m-1)}{m}$$

Equation 69

where U_S is the size of the penumbra, S is the source size and m is the geometric magnification factor. It is seen that the unsharpness of the image due to the source diameter is therefore dependent on the geometric magnification. Another source of image unsharpness is the size of the individual pixels however the effective unsharpness is reduced by the image magnification such that:

$$U_a = \frac{a}{m}$$

Equation 70

The total unsharpness of the projected image is therefore given by:

$$U_{Total} = \sqrt{U_a^2 + U_S^2}$$

Equation 71

For the X-ray CT system used the pixel size and source size as quoted by the vendor is 200 µm and 80 µm respectively. The total unsharpness across the typical magnification range is plotted in Figure 92. For these parameters it is expected that the unsharpness increases at lower values of the magnification as found in the results.

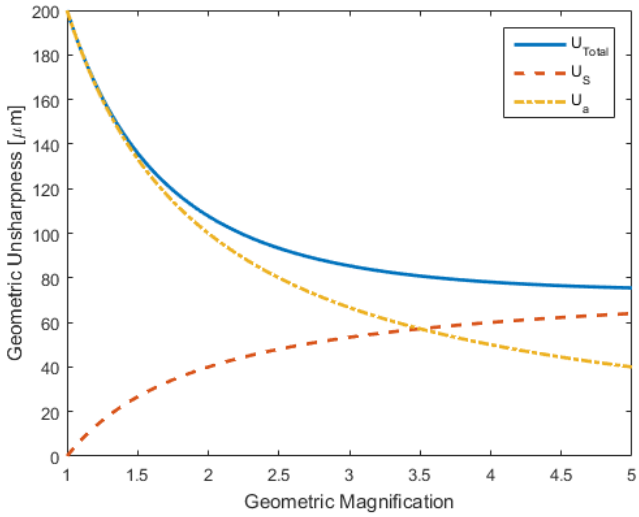

Figure 92. Plot of U_{Total} , U_a and U_S for S = 200 µm and a = 200 µm. Figure created in MATLAB ver. R2019a.

5.5.2 Erosion/Dilation of Edges When Changing the Orientation

Systematic error in the diameter measurements are also observed when changing the orientation of the hole-plate as shown in Figure 65. The measurements of the hole diameters differ considerably and there is clearly a systematic edge error. In the vertical orientation there is an edge erosion and in the horizontal orientation, there is a dilation of the material edge resulting in a negative error. Whilst in the tilted angle orientation the mean error in the hole diameters is close to zero. The erosion of the edge in the vertical orientation is explained in the previous section

Another important finding in this chapter is that the erosion effect is dependent not only on the image unsharpness but also on the magnitude of the edge gradient. In other words the more attenuating an edge is in comparison to its background, the stronger the erosion effect. When comparing the diameters of the hole-plate in the three orientations, the unsharpness should remain constant, however by changing the orientation the material path lengths are altered. In the horizontal position the X-rays have to travel through more surrounding material than in the vertical orientation as illustrated by the grey-scale profiles in Figure 93.

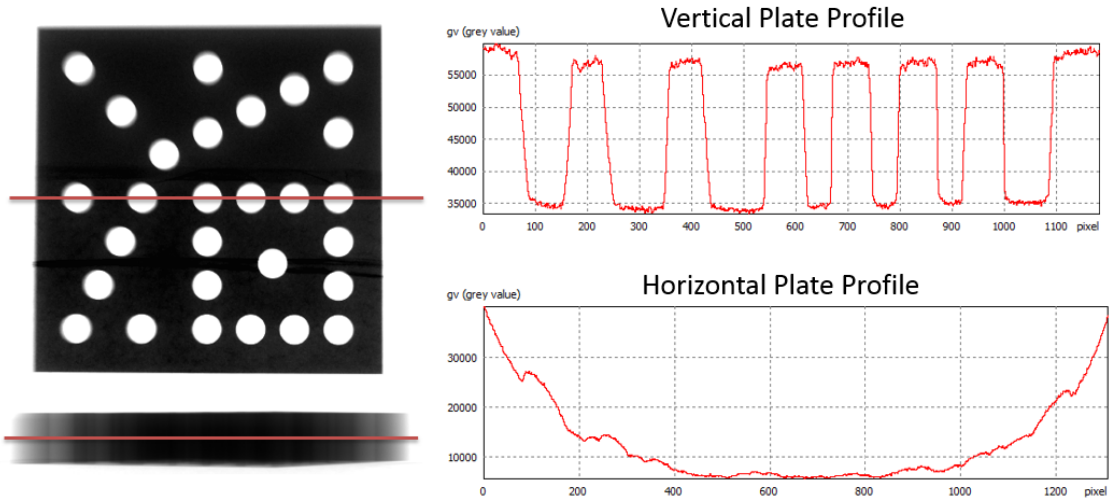

Figure 93. Grey-scale profiles taken from the projection image of the hole-plate in the vertical and horizontal orientations. The edge contrast is much greater in the vertical orientation and so is susceptible to edge erosion according to the findings in Chapter 5.

A greater edge contrast is therefore apparent in the vertical orientation. As a larger edge contrast can lead to larger edge erosion for the same degree of blurring, this can explain the strong erosion observed in the vertical orientation hole-plate measurements. Beam hardening may also contribute to this result, in the horizontal plane the mean path length through the material is greater, leading to further beam hardening. As this effect is well known to lead to dilation edges it is expected that edge dilation is observed in the horizontal orientation.

5.5.3 Summary of Hole-plate Results

After revisiting the initial results of the hole-plate measurements, it is argued that the systematic effects are in fact due the combination of beam hardening and image unsharpness. These results have also highlighted the fact that the workpiece geometry and the scan orientation can dictate how these errors manifest themselves. This is illustrated quite clearly when considering the hole diameter error in the three gross orientations (Figure 65), where on average, a positive error is observed in the vertical orientation and a negative error is observed in the horizontal orientation whilst at 45 degrees the mean error is close to zero. For the purposes of calibration, systematic errors or bias such as a global surface error can easily be corrected for. It is clear from these results however that a more complex workpiece could in fact have cases of both

edge dilation and erosion and is completely workpiece and scan parameter specific which would prevent such global treatment of error. The best approach to handle these errors therefore is to correct for these influences before reconstruction. Typical beam hardening corrections will not be applicable as they do not account for the image unsharpness. Corrections will be considered in the following further work section.

5.6 Chapter Summary

This chapter has quantified the combined effects of beam hardening and source diameter blurring on dimensional measurement in X-ray CT through simulation and experimental validation. By considering the effect of blurring filters on ideal and cupped edges, a systematic shift in the edge gradient is found when applied to the cupped edges. It is therefore argued that edge blurring is contributing to the commonly cited beam hardening edge dilation.

The effect of blurring the pre-reconstructed intensity projections is also demonstrated. This time a systematic erosion of the edge gradient is observed in the attenuation signal. Although a symmetrical smoothing filter has no influence on the edge gradient position of the intensity signal, the attenuation signal requires a logarithmic computation which results in a systematic edge error.

In order to fully quantify the effect of both of beam hardening and image blurring on measurement of X-ray CT data, a simulation was performed, enabling control over the source spectrum and the size of the source diameter. The results of the simulation confirmed the erosion of edges due to source diameter blurring. It also found the error to be dependent on the attenuation of the edge. For the worst case of a monochromic source with a 300 µm source diameter, the edge position was found to erode by 8 µm and 35 µm with a maximum attenuation value of 2 and 4 respectively.

Simulations were also performed using a polychromatic source. The dilation of edges due to beam hardening is observed for small source diameters but this dilation is dominated at large source sizes by the erosion effect of the source blur. For the worst case of an unfiltered polychromatic 400 kV source, the edge position was found to dilate by 18 µm and 14 µm when filtered by 2 mm of Cu. The effect of hardware filtering of the

source is found to not only reduce cupping artefacts and therefore reduce the edge dilation at small source sizes but to also reduce the erosion effect of the source diameter by reducing the edge contrast. It is expected that increasing the source energy or scanning a less attenuating material will have similar effects.

The results of the simulation were then verified in experimental measurements performed on a high power industrial X-ray CT system. The results of the experiment were found to be in good agreement with the simulation, confirming that a large source size lead to erosion of the edges. The effect of the source diameter on CT dimensional measurements has not previously been reported, and so the results of this study are of significance to this field. These results are probably more relevant in high power CT systems where the source diameter size tends to be larger, which is perhaps why many studies have overlooked the significance of source blurring. It should be noted that previous work did observe these erosion effects related to the source size but did not investigate these findings further [139].

It is therefore recommended that the influence of image unsharpness is carefully considered when performing X-ray CT scans for the purposes of dimensional measurement. The main contributors to the image unsharpness, the effective source diameter and the effective detector pixel size, should be minimised to reduce the influence of edge blurring. The magnification can be chosen to achieve this via Equation 71. Sufficient X-ray acceleration voltage and filtration should then also be used to reduce the influence of beam hardening and other non-linear influences related to highly attenuating edges. It is noted that these influence are more dominant in high energy X-ray applications, not to mention the addition of a high scatter fraction. This highlights the current problems with high energy X-ray imaging, where novel X-ray generation technologies such as liquid metal jet anodes or laser driven sources may help to overcome these issues in the future.

Chapter 6: Summary and Conclusion

This chapter summarises the findings of all previous chapters and outlines the key conclusions that can be drawn from this work. The limitations of this work are discussed and recommendations for future work are made. The novel contributions of this work are outlined and the specific outcomes that have resulted from this work are discussed.

6.1 Overview

The initial scope of this work was relatively broad and one of the first goals was to narrow down the large list of metrological influence factors to a few significant influences affecting dimensional measurement in industrial X-ray Computed Tomography (CT), more specifically those which were related to the interactions between the workpiece and the X-ray source.

The initial step was to understand the fundamental physical principles of the X-ray CT process such as how the X-ray source is generated, how it interacts with an object, and finally how the resulting X-ray are detected to form a radiographic image. It was also necessary to understand how these so-called projection images can be mathematically reconstructed to generate a set of cross-sectional images, as described in Chapter 2.

The following chapter focussed on how dimensional measurements can be extracted from the reconstructed CT images. Chapter 3 also reviewed the relevant scientific literature and standards to quantify the main influencing factors that have previously been studied. It also outlined the limitations with current standards and the fundamental contrast between conventional measurement techniques and dimensional X-ray CT. It was clear that these differences need to be understood in order for measurements between these techniques to be truly comparable. It is for this reason that these standards were not fully applied in this work. This chapter outlined the standard practice that has been adopted for X-ray CT measurement and the methodology followed during the experimental measurements performed in the proceeding chapters.

An initial experimental study was performed in Chapter 4 using a calibrated reference hole-plate which had been designed as a performance verification object – analogous to those used by conventional CMMs. The main aim of this work was to characterise the typical errors observed in X-ray CT and quantify the magnitude of these errors to understand the most significant. The study used a range of industrial X-ray CT systems, including a metrology grade system to act as a benchmark. The workpiece was also scanned using a number of different configurations to understand the influence of orientation and scan position on the measurement results. A number of unexpected systematic effects were observed in the results which appeared as errors in the edge position; both erosion and dilation of the edges were recorded. These were correlated to the orientation and position (geometric magnification factor) of the hole-plate and could not be explained by previously understood influences such and beam hardening and scattering. After applying smoothing filters to the reconstructed images it was found that image unsharpness could lead to erosion of the edge. It was therefore decided that influence of image unsharpness would be studied further in the proceeding chapter. A key finding of this chapter was the fact that equivalent dimensional error was found between the standard and metrology systems, highlighting the need for further work to be performed to understand the source of these errors.

Chapter 5 initially demonstrated how the gradient of theoretical edges behaved when smoothing filters were applied. More importantly, it considered at which stage in the data acquisition this smoothing was applied. It was found that when smoothing filters were applied to reconstructed data with cupping artefacts, the edge bias was in the direction material surface; that is edges would dilate agreeing with previous findings. Applying these kind of image processing filters are typically optional and can be omitted from the measurement workflow, other sources of image unsharpness are inherent in the X-ray CT process. For this reason, these smoothing filters were also applied to ideal radiographic edges and the resulting signal processed through the necessary steps. Since the X-ray attenuation is calculated through a logarithmic operation, it was again found that an edge bias resulted from the application of the smoothing filter. This time however, the edge error was in the opposing direction; leading to an erosion of the edge.

These edge effects were studied further by performing a full fan beam simulation which modelled a finite X-ray source diameter and X-ray energy spectrum. This was used to generate a number of reconstructed cylindrical cross-sections with various levels of unsharpness and cupping artefacts. The edge position was then measured to determine the influence of these properties on dimensional measurement. The results of the simulation largely agreed with the previous findings; that stronger cupping artefacts caused by a more polychromatic source lead to dilation of edges. However the erosion effect due to a finite source size was more dominant in this case and lead to edge erosion. The erosion was also dependent on the edge contrast, it would therefore be expected that an exterior surface would be influenced more than an interior one.

To validate these results, an experimental X-ray CT scan was performed using a fan beam cross-section of a steel cylindrical workpiece. The results of the simulation were emulated and good agreement between the experimental and simulated measurements were observed. It was found that the erosion and dilation effects could be described by the influence of image unsharpness and beam hardening. These results have highlighted the significance of the workpiece geometry, the scan orientation and the geometrical magnification.

6.2 Limitations

Limitations of this work mainly relate to the consideration of other relevant influence factors such as X-ray scatter, the influence of the filtration process during reconstruction, the influence of the detector characteristics such as the unsharpness, noise and efficiency. This work therefore has only considered the most significant influence such as beam hardening as the main cause of cupping artefacts and the X-ray source diameter as the cause of unsharpness. However, scattering is known to have similar effects on the CT image as beam hardening and image unsharpness can come from a number of other influences. These lesser effect have been neglected but should be considered in future work, for example, Compton scattering is known to be much more problematic at higher X-ray energies as it becomes the dominant interaction mechanism, as described in 2.1.2. Limitations of the simulation and experimentation in Chapter 5 should be highlighted also. Here, only fan beam CT was considered in order

to simplify the computation and also to negate the influence of scatter in the experimental trials as scattered X-rays will mostly fall out of the fan beam plane and therefore will not be recorded by the detector. The geometry of the test object was also simplistic and only external surfaces were considered as other work has demonstrated that these are more strongly influenced by the effects of cupping artefacts. A further limitation of this work is the method of surface determination; in this work the position of edges was determined by measuring the edge gradient; different methods of edge detection have been considered in other studies and a gradient based approach has been demonstrated to be the most robust method for dimensional metrology applications.

6.3 Research Outcomes

Overall, this work has investigated a number of influence factors that lead to systematic erosion or dilation of material edges in a CT scan. The key findings of this work were the influence of the X-ray source characteristics on the determination of edges in X-ray CT images. It was found that the most influencing attributes were the energy spectrum and the physical size of the X-ray source. In previous work, beam hardening had been found to cause dilation of material edges in the reconstructed image. In this work however, a systematic effect was demonstrated between cupping artefacts, caused by beam hardening, and edge blurring. It was found that smoothing cupped edges could amplify the dilation effect, leading to an increased error. Since the finite size of the source is a potential cause of image unsharpness in X-ray CT, it was expected that the combination of beam hardening and a finite source size would lead to further dilation of edges. It was found however that unsharpness caused by the X-ray source size lead to a systematic erosion of edges. This was an interesting result and it has not previously been reported in the literature.

The novel contributions of this work are therefore summarised as follows:

i. By performing scans of a calibrated workpiece on multiple CT systems this work has highlighted the benefits and limitations of three industrial CT systems. Firstly the advantages of the metrology CT system to perform unidirectional length measurements compared with the standard systems. Secondly the result that

the metrology CT system offered no advantage when performing edge dependent measurement. When using the ball bar reference artefact to adjust the voxel scale of subsequent scans on a non-metrology X-ray CT system, unidirectional length errors up to 0.1 % were observed.

ii. This work studied the influence of blurring on X-ray CT images, more specifically the influence that smoothing had on the edge gradient. To the authors knowledge this is the first time that these effects of the source and pixel size have been quantified in a metrology context and a number of key findings were reported.

iii. The first of these findings was the effect of blurring the pre-reconstruction radiographic intensity images which lead to a systematic erosion of the edge gradient. The magnitude of this effect was found to be dependent on the width of the smoothing filter and the contrast of the material edge. In the simulated measurements of a cylindrical workpiece, for the worst case of a 300 µm source diameter at a geometric magnification of 5, the edge position was found to erode by 8 µm and 35 µm with a maximum attenuation value of 2 and 4 respectively.

iv. The second of these findings was the effect of blurring on the reconstructed CT images afflicted with cupping artefacts which lead to a systematic dilation of the edge gradient. The magnitude of this effect was found to be dependent on the width of the smoothing filter or voxel size and the strength of the cupping artefact. In the simulated measurements of a cylindrical workpiece, for the worst case of an unfiltered polychromatic 400 kV source, the edge position was found to dilate by 18 µm and 14 µm when filtered by 2 mm of Cu.

v. These findings were then used to both predict and explain systematic errors observed within experimental results.

A number of beneficial outcomes have resulted from the findings of this work. The Manufacturing Technology Centre who sponsored this doctorate recently purchased a metrology X-ray CT system to expand their capability in this area. A transmission target tube was favoured over the reflection target due to the superior source resolution in order to reduce the influence of blurring. A smaller detector pixel pitch was also chosen for the same reasons. The MTC now also has representatives on the ISO/TC 213,

contributing to the ISO 10360 Part 11. The MTC has also recently joined the AdvanCT (Advanced Computed Tomography for dimensional and surface measurements in industry) project as a collaborator funded by the European Metrology Research Programme EMPIR. A number of industrial projects were also contributed to as part of this doctorate including a core research project on industrial X-ray CT and a recent innovate UK project named 3-in-1 X-ray CT (Reference Number: 103466). It is also expected that the main outcomes of this work will be published at the end of this doctorate.

6.4 Further Work

This section will discuss the recommended further work that has not been covered within this doctoral thesis. This will include possible correction methods that can account for the combined effect of beam hardening and blurring, assessing the influence of more complex geometries, assessing the influence of other sources of unsharpness including the pixel size and the reconstruction filter, the effect of scatter and assessing different methods for the surface determination and reconstruction process.

In Chapter 5, dilation and erosion effects were observed within the simulated and experimental results by measuring the outer diameter of a cylindrical object. This was used as it represents the simplest geometry and therefore reducing the influence of other influencing factors. This work however did not quantify the edge effects for more complex geometries, including internal holes and other features. Further work in this area is recommended to understand these edge effects better. A full simulation of the hole-plate geometry would give more insight into the systematic error observed in Chapter 4. This would however require performing a full cone-beam acquisition of the workpiece which would be harder to implement. There are currently a number of commercial simulation packages available which could be tested, however.

6.4.1 Non-linear Influences

In this thesis, the effects of beam hardening were analysed extensively as it is the principal contributor of non-linear attenuation in X-ray CT. There exist however numerous other sources of error which can lead to misrepresentation of the grey-scale

values. These effects include X-ray scatter, detector afterglow caused by the lag in the scintillation process, the heel effect which is caused by difference in X-ray path length through the X-ray target leading to a non-uniform source spectrum over the detector area. Although these influences are well-known they were not considered within this work. Further work should therefore look to include these effects especially when applying beam hardening correction as outlined in [91].

6.4.2 Sources of Unsharpness

As discussed previously within this chapter, many other sources of image unsharpness exist and should be included within the scope of any follow-on studies. An experimental study could be performed to demonstrate the influence of the geometric sources of unsharpness on measurement and how this varies within the scanner volume; this could be done using a cylindrical object such as that used in Chapter 5. Other factors should be considered as well such as the influence of source or object movement on the unsharpness and the influence of the reconstruction filter. Another study should look into the effect of arbitrarily varying the size of the voxel grid to see what effect this could have on measurement results.

6.4.3 Correction Methods

Approaches to correction of beam hardening have been looked at extensively in the available literature. The standard approach to beam hardening correction of a single material object is to use the linearization method. This method attempts to correct the projection images in order to obtain the grey-scales that would be recorded for the case of a monochromatic X-ray source .i.e. linearly proportional to the ray path lengths. This can be performed with knowledge of the attenuation curve which describes the attenuation of the source at each material penetration depth. The form of the attenuation curve depends not only on the object material but also the X-ray source spectrum and detector energy response. The goal of beam hardening correction of a single material is therefore is to obtain this attenuation curve either through estimation, modelling, iteration or direct measurement.

Correction of image unsharpness have also been explored. Image deconvolution techniques are well established and are used for many image enhancement applications

[140]. These methods attempt to estimate the PSF of the image in order to restore the true image, so called blind deconvolution involves trying many estimation of the PSF without prior knowledge and then assessing if the image has improved.

This work has considered the combined effect of the source size and spectrum on the reconstructed edges, the influence of a combination of these effects is difficult to predict and therefore correct for. An iterative approach may therefore provide the most promising way of 'undoing' the effect of the source. Other methods of correcting for edge error include the use of known reference object; with interior and exterior features which could be used to determine the first order edge bias, leading to improved accuracy.

6.4.4 Surface Determination Methods

This work has primarily looked at gradient based surface determination methods however further work could look into applying different methods to determine the edges in the CT image. Different methods or fitting techniques could be less susceptible the effects of systematic erosion and dilation. This could be explored in the context of future work.

Appendix A

Hole-plate reference measurements provided by the NPL.

Table 14. Reference diameters and centre positions for each of the 28 holes on the hole-plate artefact.

Hole ID	X Position (mm)	Y Position (mm)	Z Position (mm)	Hole Diameter (mm)
1	6.00992	6.00072	-4.01314	3.99915
2	12.00465	6.00074	-4.01241	3.99696
3	18.00551	6.00546	-4.01167	3.99916
4	24.00798	6.00846	-4.01094	3.99811
5	33.00408	6.00984	-4.00984	3.99993
6	42.01047	6.01267	-4.00873	3.99577
7	6.00939	12.002	-4.01221	3.99749
8	24.00011	12.00568	-4.01001	3.99899
9	38.99975	12.00884	-4.00817	3.99487
10	15.00202	15.0069	-4.01065	3.99817
11	6.00874	18.00573	-4.01128	3.99879
12	24.00026	18.00973	-4.00908	3.99933
13	35.99954	18.0022	-4.00761	3.99626
14	6.00701	24.00358	-4.01035	3.99804
15	12.00579	24.01166	-4.00962	3.99837
16	18.006	24.00659	-4.00888	3.99833
17	24.00838	24.01057	-4.00815	3.99821
18	33.01028	24.00501	-4.00705	3.9965
19	42.00206	24.0098	-4.00594	3.99498
20	30.00557	30.00296	-4.00648	3.99645
21	6.00536	33.00175	-4.00896	3.99649
22	23.99981	33.01355	-4.00675	3.99449
23	18.0113	36.01503	-4.00702	3.99727

24	36.00526	36.0093	-4.00482	3.99558
25	12.00281	38.99595	-4.00729	3.99769
26	6.01195	42.00184	-4.00756	3.99769
27	23.99847	42.00726	-4.00536	3.99736
28	42.00147	42.01213	-4.00315	3.99412

Table 15.Reference length values for the unidirectional and bidirectional length on the hole-plate artefact.

Unidirectional Length ID	Length (mm)	Bidirectional Length ID	Length (mm)
<Uni_A1>_1	6.709582	<Bi_A1>_1	10.7049
<Uni_A1>_2	13.41194	< Bi_A1>_2	17.40795
<Uni_A1>_3	20.11785	< Bi_A1>_3	24.11398
<Uni_A1>_4	26.82632	< Bi_A1>_4	30.82243
<Uni_A1>_5	40.24975	< Bi_A1>_5	44.24632
<Uni_A2>_1	6.702669	< Bi_A2>_1	10.70036
<Uni_A2>_2	13.40993	< Bi_A2>_2	17.40741
<Uni_A2>_3	20.10852	< Bi_A2>_3	24.10461
<Uni_A2>_4	26.82661	< Bi_A2>_4	30.82368
<Uni_A2>_5	40.23682	< Bi_A2>_5	44.23315
<Uni_D1>_1	8.484604	< Bi_D1>_1	12.47945
<Uni_D1>_2	16.97415	< Bi_D1>_2	20.96944
<Uni_D1>_3	25.45206	< Bi_D1>_3	29.44823
<Uni_D1>_4	38.18708	< Bi_D1>_4	42.18322
<Uni_D1>_5	50.91378	< Bi_D1>_5	54.91042
<Uni_H1>_1	5.99473	< Bi_H1>_1	9.992785
<Uni_H1>_2	11.99559	< Bi_H1>_2	15.99475
<Uni_H1>_3	17.99806	< Bi_H1>_3	21.99669
<Uni_H1>_4	26.99416	< Bi_H1>_4	30.9937
<Uni_H1>_5	36.00055	< Bi_H1>_5	39.99801
<Uni_H2>_1	5.998785	< Bi_H2>_1	9.99699

<Uni_H2>_2	11.99899	< Bi_H2>_2	15.99718
<Uni_H2>_3	18.00137	< Bi_H2>_3	21.9995
<Uni_H2>_4	27.00327	< Bi_H2>_4	31.00054
<Uni_H2>_5	35.99505	< Bi_H2>_5	39.99156
<Uni_V1>_1	6.00128	< Bi_V1>_1	9.9996
<Uni_V1>_2	12.00501	< Bi_V1>_2	16.00398
<Uni_V1>_3	18.00286	< Bi_V1>_3	22.00146
<Uni_V1>_4	27.00103	< Bi_V1>_4	30.99885
<Uni_V1>_5	36.00112	< Bi_V1>_5	39.99954
<Uni_V2>_1	5.997225	< Bi_V2>_1	9.995775
<Uni_V2>_2	12.00127	< Bi_V2>_2	15.99999
<Uni_V2>_3	18.00211	< Bi_V2>_3	22.00027
<Uni_V2>_4	27.00509	< Bi_V2>_4	31.00139
<Uni_V2>_5	35.9988	< Bi_V2>_5	39.99654

References

[1] NPL, *Good practice guide No. 131 - Beginner' s guide to measurement in mechanical engineering*, no. 131. NPL Good Practice Guide, 2013.

[2] M. Goldsmith, *Good practice guide No. 118 - A beginner's guide to measurement*, no. 118. NPL Good Practice Guide, 2010.

[3] F. Redgrave and P. Howarth, *Metrology – In Short*, 3rd Editio. EURAMET project 1011, 2008.

[4] A. Weckenmann, P. Kraemer, and J. Hoffmann, "Manufacturing metrology – State of the art and prospects," in *Proceedings of the 9th International Symposium on Measurement and Quality Control*, 2007, p. [Online]. Available: www.semanticscholar.org.

[5] "Hexagon manufacturing intelligence," 2018. [Online]. Available: https://www.hexagonmi.com/products/coordinate-measuring-machines/bridge-cmms/leitz-infinity. [Accessed: 19-Aug-2018].

[6] L. De Chiffre, S. Carmignato, J. P. Kruth, R. Schmitt, and A. Weckenmann, "Industrial applications of computed tomography," *CIRP Ann. - Manuf. Technol.*, vol. 63, no. 2, pp. 655–677, 2014.

[7] R. Hague, P. Reeves, and S. Jones, *Mapping UK research and innovation in additive manufacturing*. Innovate UK: Manufacturing and materials Research and development UK economic growth, 2016.

[8] "Additive manufacturing UK national strategy 2018 - 25," 2018.

[9] T. Buzug, *Computed Tomogrpahy - From photon statistics to modern cone-beam CT*. Berlin, Germany: Springer, 2008.

[10] H. Saewert, D. Fiedler, M. Bartscher, and F. Wäldele, "Obtaining dimensional information by industrial CT scanning – present and prospective process chain," in *International Symposium on Computed Tomography and Image Processing for Industrial Radiology*, 2003, pp. 163–172.

[11] W. Sun, S. B. Brown, and R. K. Leach, *An overview of industrial x-ray computed tomography*. National Physical Laboratory, 2012.

[12] A. Weckenmann and P. Krämer, “Application of computed tomography in manufacturing metrology,” *Tech. Mess.*, vol. 76, no. 7–8, pp. 340–346, 2009.

[13] R. Christoph and H. J. Neumann, *X-ray tomography in industrial metrology*. Werth Messtechnik GmbH, 2012.

[14] H. Villarraga-Gómez, “X-ray computed tomography for dimensional measurements,” *Digit. Imaging*, vol. 48116, pp. 44–57, 2016.

[15] F. Welkenhuyzen, K. Kiekens, M. Pierlet, and W. Dewulf, “Industrial computer tomography for dimensional metrology : Overview of influence factors and improvement strategies,” *Opt. Meas. Tech. Struct. Syst.*, vol. 100, no. 9, pp. 401–410, 2010.

[16] S. Kasperl, J. Hiller, and M. Krumm, “Computed tomography metrology in industrial research & development,” in *International Symposium on NDT in Aerospace*, 2009, p. [Online]. Available: http://www.ndt.net/?id=8052.

[17] J. P. Kruth, M. Bartscher, S. Carmignato, R. Schmitt, L. De Chiffre, and A. Weckenmann, “Computed tomography for dimensional metrology,” *CIRP Ann. - Manuf. Technol.*, vol. 60, no. 2, pp. 821–842, 2011.

[18] Zeiss, “Zeiss Xradia 810 Ultra.” [Online]. Available: https://www.zeiss.com/microscopy/int/products/x-ray-microscopy/xradia-810-ultra.html. [Accessed: 11-Apr-2020].

[19] A. Townsend, L. Pagani, P. Scott, and L. Blunt, “Areal surface texture data extraction from X-ray computed tomography reconstructions of metal additively manufactured parts,” *Precis. Eng.*, vol. 48, pp. 254–264, 2017.

[20] Joint Committee for Guides in Metrology, *Evaluation of measurement data — Guide to the expression of uncertainty in measurement*. International Organization for Standardization, 2008.

[21] ISO, *ISO 15708-1 - Non-destructive testing - Radiation methods - Computed tomography - Part 1: Principles*. International Organization for Standardization, 2002.

[22] ISO, *ISO 15708-2 - Non-destructive testing — Radiation methods — Computed tomography — Part 2: Examination practices*, vol. 2002. International Organization for Standardization, 2002.

[23] "ASTM E1814 - 14 Standard practice for Computed Tomographic (CT) examination of castings." ASTM International, 2014.

[24] *VDI/VDE 2630 - Computed tomography in dimensional measurement - Part 1.1 - Fundamentals and definitions*. The Association of German Engineers, 2015.

[25] *VDI/VDE 2630 - Computed tomography in dimensional measurement - Part 1.2 - Influencing variables on measurement results and recommendations for computed-tomography dimensional measurements*. The Association of German Engineers, 2010.

[26] *VDI/VDE 2630 - Computed tomography in dimensional measurement - Part 1.3 - Guideline for the application of DIN EN ISO 10360 for coordinate measuring machines with CT sensors*. The Association of German Engineers, 2010.

[27] *VDI/VDE 2630 - Computed tomography in dimensional metrology - Part 1.4 - Measurement procedure and comparability*. The Association of German Engineers, 2010.

[28] *VDI/VDE 2630 - Computed tomography in dimensional measurement - Part 2.1 - Determination of the uncertainty of measurement and the test process suitability of coordinate measurement systems with CT sensors*. The Association of German Engineers, 2010.

[29] M. Bartscher, O. Sato, F. Härtig, and U. Neuschaefer-Rube, "Current state of standardization in the field of dimensional computed tomography," *Meas. Sci. Technol.*, vol. 25, no. 6, p. 064013, 2014.

[30] Werth, “TomoScope - Werth,” 2020. [Online]. Available: https://werthinc.com/products/tomoscope-200/. [Accessed: 11-Apr-2020].

[31] Baker Hughes, “Phoenix nanotom m,” 2020. [Online]. Available: https://www.bakerhughesds.com/inspection-technologies/radiography-ct/x-ray-computed-tomography/phoenix-nanotom-m. [Accessed: 11-Apr-2020].

[32] YXLON, “CT Precision - YXLON,” 2015. [Online]. Available: https://www.yxlon.com/Yxlon/media/Content/Products/X-ray and CT inspection systems/YXLON CT Precision/CT_Precision_Product-brochure_12_2015_eng-A4-OP.pdf. [Accessed: 11-Apr-2020].

[33] Zeiss, “Metrotom - Zeiss,” 2020. [Online]. Available: https://www.zeiss.co.uk/metrology/products/systems/computed-tomography/metrotom.html. [Accessed: 11-Apr-2020].

[34] Nikon Metrology, “MCT225 - Nikon,” 2020. [Online]. Available: https://www.nikonmetrology.com/en-gb/product/mct225. [Accessed: 11-Apr-2020].

[35] J. G. Anderson, “William Morgan and X-rays,” *Trans. Fac. Actuar.*, vol. 17, no. 162, pp. 219–221, 1938.

[36] B. Kevles, *Naked to the bone: medical imaging in the twentieth century*. Rutgers University Press, 1997.

[37] W. C. Röntgen, “On a New Kind of Rays,” *Science (80-.).*, vol. 3, no. 59, pp. 227–231, 1896.

[38] S. Webb, *The physics of medical imaging*. CRC Press, 1988.

[39] K. Sansare, V. Khanna, and F. Karjodkar, “Early victims of X-rays: a tribute and current perception,” *Dentomaxillofacial Radiol.*, vol. 40, no. 2, pp. 123–125, Feb. 2011.

[40] HSE, *Work with ionising radiation*. HSE Books, 2000.

[41] D. Mery, V. Riffo, U. Zscherpel, G. Mondragón, I. Lillo, I. Zuccar, H. Lobel, and M. Carrasco, “GDXray : The database of x-ray images for nondestructive testing,” *J. Nondestruct. Eval.*, vol. 34.4, pp. 1–12, 2015.

[42] R. Behling, *Modern diagnostic x-ray sources : technology, manufacturing, reliability*. CRC Press, 2015.

[43] P. J. Duke, *Synchrotron radiation : production and properties*. Oxford University Press, 2009.

[44] *ASTM E1441 - 11 - Standard Guide for computed tomography (CT) imaging*. ASTM International, 2011.

[45] M. J. Berger, J. H. Hubbell, S. M. Seltzer, J. Chang, J. S. Coursey, R. Sukumar, D. S. Zucker, and K. Olsen, “XCOM: Photon cross sections database,” 2010. [Online]. Available: https://www.nist.gov/pml/xcom-photon-cross-sections-database. [Accessed: 11-Apr-2020].

[46] *BS EN 16016-2 - Non destructive testing - Radiation methods - Computed tomography - Part 2: Principle, equipment and samples*. British Standards Institue, 2011.

[47] A. Kak and M. Slaney, *Principles of computerized tomographic imaging*. Society for Industrial and Applied Mathematics, 2001.

[48] L. A. Feldkamp, L. C. Davis, and J. W. Kress, “Practical cone-beam algorithm,” *J. Opt. Soc. Am. A*, vol. 1, no. 6, p. 612, 1984.

[49] H. K. Tuy, “An inversion formula for cone-beam reconstruction,” *SIAM J. Appl. Math.*, vol. 43, no. 3, pp. 546–552, Jun. 1983.

[50] S. M. Hubbell, J.H. and Seltzer, “NIST X-Ray mass attenuation coefficients,” 2004. [Online]. Available: https://www.nist.gov/pml/x-ray-mass-attenuation-coefficients. [Accessed: 11-Apr-2020].

[51] A. Duerinckx and A. Macovski, “Polychromatic streak artifacts in computed tomography images.,” *J. Comput. Assist. Tomogr.*, vol. 2, no. 4, pp. 481–487,

1978.

[52] Y. Sun, Y. Hou, F. Zhao, and J. Hu, “A calibration method for misaligned scanner geometry in cone-beam computed tomography,” *NDT E Int.*, vol. 39, no. 6, pp. 499–513, 2006.

[53] J. Hsieh, *Computed tomography : principles, design, artifacts, and recent advances*. SPIE Optical Engineering Press, 2003.

[54] M. Bartscher, U. Hilpert, J. Goebbels, and G. Weidemann, “Enhancement and proof of accuracy of industrial Computed Tomography (CT) measurements,” *CIRP Ann. - Manuf. Technol.*, vol. 56, no. 1, pp. 495–498, 2007.

[55] P. Müller, “Coordinate metrology by traceable computed tomography,” Technical University of Denmark,Kongens Lyngby, [Doctoral Thesis], 2013.

[56] S. Carmignato and A. Pierobon, “Preliminary results of the ‘ CT Audit ’ project : First international intercomparison of computed tomography systems for dimensional metrology,” in *International Symposium on Digital Industrial Radiology and Computed Tomography*, 2011, p. [Online]. Available: http://www.ndt.net/?id=11122.

[57] “CXMM50 - North Star Imaging,” 2020. [Online]. Available: https://4nsi.com/innovations/metrology/. [Accessed: 11-Apr-2020].

[58] P. Müller, A. Cantatore, J. L. Andreasen, J. Hiller, and L. De Chiffre, “Computed tomography as a tool for tolerance verification of industrial parts,” *Procedia CIRP*, vol. 10, pp. 125–132, 2013.

[59] K. Kiekens, F. Welkenhuyzen, Y. Tan, P. Bleys, A. Voet, J. P. Kruth, and W. Dewulf, “A test object for calibration and accuracy assessment in X-ray CT metrology,” in *10th International Symposium on Measurement and Quality Control*, 2010, pp. 528–531.

[60] Joint Committee for Guides in Metrology, *International vocabulary of basic and general terms in metrology (VIM)*. International Organization for

Standardization, 2004.

[61] S. Bell, *Good practice guide No.11 - A beginner's guide to uncertainty of measurement*. NPL Good Practice Guide, 1999.

[62] *ISO 9001 - Quality management systems - Requirements*. International Organization for Standardization, 2008.

[63] *ISO 1:2016 - Geometrical product specifications (GPS) -- Standard reference temperature for the specification of geometrical and dimensional properties*. International Organization for Standardization, 2016.

[64] *ISO 14253-2:2011 - Geometrical product specifications (GPS) -- Inspection by measurement of workpieces and measuring equipment -- Part 2: Guidance for the estimation of uncertainty in GPS measurement, in calibration of measuring equipment and in product v*. International Organization for Standardization, 2011.

[65] K. Birch, *Good practice guide No. 36 - Estimating uncertainties in testing*. NPL Good Practice Guide, 2003.

[66] D. Flack and H. John, *Fundamental good practice in dimensional metrology - No. 80*. NPL Good Practice Guide, 2005.

[67] *ISO/TS 15530-3:2004 - Geometrical Product Specifications (GPS) -- Coordinate measuring machines (CMM): Technique for determining the uncertainty of measurement -- Part 3: Use of calibrated workpieces or standards*, no. Cmm. International Organization for Standardization, 2004.

[68] P. Wenig and S. Kasperl, "Examination of the measurement uncertainty on dimensional measurements by x-ray," in *Proceedings of 9th European Conference on Non-Destructive Testing (ECNDT)*, 2006, p. We. 3.3.1.

[69] *DD ISO/TS 15530-4 - Geometrical Product Specifications (GPS) — Coordinate measuring machines (CMM): Technique for determining the uncertainty of measurement —*. International Organization for Standardization, 2004.

[70] D. Flack, *Good practice guide No. 42 - CMM verification*. NPL Good Practice Guide, 2011.

[71] S. Carmignato, A. Pierobon, P. Rampazzo, M. Parisatto, and E. Savio, “CT for industrial metrology – accuracy and structural resolution of CT dimensional measurements,” in *Conference on Industrial Computed Tomography (ICT)*, 2012, pp. 161–172.

[72] V. Andreu, B. Georgi, H. Lettenbauer, and J. A. Yague, “Analysis of the error sources of a computer tomography machine,” in *Proc. Lamdamap conference*, 2009, pp. 462–471.

[73] C. Heinzl, J. Kastner, A. Amirkhamov, E. Gröller, and C. Gusenbauer, “Optimal specimen placement in cone beam x-ray computed tomography,” *NDT E Int.*, vol. 50, pp. 42–49, 2012.

[74] M. V Yester and G. T. Barnes., “Geometrical limitations of computed tomography (CT) scanner resolution,” *Appl. Opt. Instrum. Med. VI*, vol. 127, pp. 296–303, 1977.

[75] P. Müller, J. Hiller, A. Cantatore, and L. De Chiffre, “Investigation of measuring strategies in computed tomography,” in *Proceedings of the International conference on Advanced Manufacturing Engineering.*, 2011, pp. 31–42.

[76] *BS EN 16016-3 - Non destructive testing — Radiation methods — Computed Tomography Part 3: Operation and interpretation*, no. September 2011. British Standards Institue, 2011.

[77] F. Welkenhuyzen, B. Boeckmans, Y. Tan, K. Kiekens, and W. Dewulf, “Investigation of the kinematic system of a 450 kV CT scanner and its influence on dimensional CT metrology applications,” in *5th Conference on Industrial Computed Tomography (ICT)*, 2014, pp. 217–225.

[78] Y. Pan, F. De Carlo, and X. Xiao., “Automatic detection of rotational centers using GPU from projection data for micro-tomography in synchrotron radiation.,” *Med. Imaging*, vol. 8313, p. 831328, 2012.

[79] D. Gürsoy, F. De Carlo, X. Xiao., and C. Jacobsen, “TomoPy: a framework for the analysis of synchrotron tomographic data,” *J. Synchrotron Radiat.*, vol. 21, no. 5, pp. 1188–1193, 2014.

[80] P. Joseph and R. Spital, “The effects of scatter in x-ray computed tomography,” *Med. Phys.*, vol. 9, no. 4, pp. 464–472, 1982.

[81] S. Kasperl and J. Hiller, “Artefact correction at coordinate measuring with industrial X-ray computed tomography,” *TM. Tech. Mess.*, vol. 76, no. 9, pp. 401–409, 2009.

[82] G. Van Gompel, K. Van Slambrouck, M. Defrise, K. J. Batenburg, J. de Mey, J. Sijbers, and J. Nuyts, “Iterative correction of beam hardening artifacts in CT,” *Med. Phys.*, vol. 38, no. S1, pp. S36–S49, 2011.

[83] P. Krämer and A. Weckenmann, “Multi-energy image stack fusion in computed tomography,” *Meas. Sci. Technol.*, vol. 21, no. 4, p. 045105, 2010.

[84] J. Seibert, O. Nalcioglu, and W. Roeck, “Removal of image intensifier veiling glare by mathematical deconvolution techniques,” *Med. Phys.*, vol. 12, no. 3, pp. 281–288, 1985.

[85] J. Seibert and J. Boone, “X-ray scatter removal by deconvolution,” *Med. Phys.*, vol. 15, no. 4, pp. 567–575, 1988.

[86] U. Neitzel, “Grids or air gaps for scatter reduction in digital radiography: A model calculation,” *Medical Physics*, vol. 19, no. 2. pp. 475–481, 1992.

[87] Y. Kyriakou, T. Riedel, and W. A. Kalender, “Combining deterministic and Monte Carlo calculations for fast estimation of scatter intensities in CT,” *Phys. Med. Biol.*, vol. 51, no. 18, pp. 4567–4586, 2006.

[88] J. J. Lifton, A. A. Malcolm, J. W. Mcbride, and K. J. Cross, “The application of voxel size correction in x-ray computed tomography for dimensional metrology,” in *Singapore international NDT conference & exhibition*, 2013, p. [Online]. Available: http://www.ndt.net/?id=14606.

[89] J. Hiller, S. Kasperl, T. Schön, S. Schröpfer, and D. Weiss, “Comparison of probing error in dimensional measurement by means of 3D computed tomography with circular and helical sampling,” in *2nd International Symposium on NDT in Aerospace 2010*, 2010, p. [online]. Available: http://www.ndt.net/?id=10437.

[90] J. Muders, J. Hesser, A. Lachner, and C. Reinhart, “Accuracy evaluation and exploration of measurement uncertainty for exact helical cone beam reconstruction using katsevich filtered backprojection in comparison to circular feldkamp reconstruction with respect to industrial CT metrology,” in *International Symposium on Digital Industrial Radiology and Computed Tomography*, 2011, p. [Online]. Available:http://www.ndt.net/?id=11123.

[91] J. J. Lifton, “The influence of scatter and beam hardening in x-ray computed tomography for dimensional metrology,” University of Southampton, Southampton, [Doctoral Thesis], 2015.

[92] N. Otsu, “A threshold selection method from gray-level histograms,” *IEEE Trans. Syst. Man. Cybern.*, vol. 9, no. 1, pp. 62–66, 1979.

[93] J. Canny, “A computational approach to edge detection.,” *IEEE Trans. Pattern Anal. Mach. Intell.*, vol. 8, no. 6, pp. 679–698, 1986.

[94] Y. Tan, K. Kiekens, J. Kruth, A. Voet, and W. Dewulf, “Material dependent thresholding for dimensional x-ray computed tomography,” *Int. Symp. Digit. Ind. Radiol. Comput. Tomogr. - Mo.4.3 Mater.*, pp. 3–10, 2011.

[95] C. Heinzl, J. Kastner, B. Georgi, and H. Lettenbauer, “Comparison of surface detection methods to evaluate cone beam computed tomography data for three dimensional metrology,” in *International symposium on digital industrial radiology and computed tomography*, 2007, pp. 25–27.

[96] J. A. Yagüe-Fabra, S. Ontiveros, R. Jiménez, S. Chitchian, G. Tosello, and S. Carmignato, “A 3D edge detection technique for surface extraction in computed tomography for dimensional metrology applications,” *CIRP Ann. - Manuf. Technol.*, vol. 62, no. 1, pp. 531–534, 2013.

[97] B. Nielsen, *Resolution, unsharpness and MTF*. Linköping university, 1980.

[98] A. Schuster, *An introduction to the theory of optics*. London, E. Arnold, 1904.

[99] R. Halmshaw, *Industrial radiology: theory and practice*. Springer Science & Business Media, 2012.

[100] N. Flay and R. K. Leach, "Application of the optical transfer function in X-ray computed tomography – a review," *NPL Rep. ENG 41*, 2012.

[101] T. Williams, *The optical transfer function of imaging systems*. CRC Press, 1998.

[102] L. Townsend, A., Pagani, L., Scott, P. and Blunt, "Areal surface texture data extraction from x-ray computed tomography reconstructions of metal additively manufactured parts," *Precis. Eng.*, vol. 48, pp. 254–264, 2017.

[103] G. Kerckhofs, G. Pyka, M. Moesen, and J. Schrooten, "High-resolution micro-CT as a tool for 3D surface roughness measurement of 3D additive manufactured porous structures," *Proc. iCT*, pp. 77–83, 2012.

[104] A. Thompson, L. Korner, N. Senin, S. Lawes, I. Maskery, and R. Leach, "Measurement of the internal surface texture of additively manufactured parts by X-ray computed tomography," in *Conference on Industrial Computed Tomography (iCT)*, 2017, no. iCT, p. [Online]. Available: http://www.ndt.net/?id=20810.

[105] J. Kumar, A. Attridge, P. K. C. Wood, and M. A. Williams, "Analysis of the effect of cone-beam geometry and test object configuration on the measurement accuracy of a computed tomography scanner used for dimensional measurement," *Meas. Sci. Technol.*, vol. 22, no. 3, p. 035105, 2011.

[106] S. Carmignato, D. Dreossi, L. Mancini, F. Marinello, G. Tromba, and E. Savio, "Testing of x-ray microtomography systems using a traceable geometrical standard," *Meas. Sci. Technol.*, vol. 20, no. 8, p. 084021, 2009.

[107] W. Dewulf, K. Kiekens, Y. Tan, F. Welkenhuyzen, and J. P. Kruth, "Uncertainty determination and quantification for dimensional measurements with industrial

computed tomography," *CIRP Ann. - Manuf. Technol.*, vol. 62, no. 1, pp. 535–538, 2013.

[108] J. Hiller, M. Maisl, and L. M. Reindl, "Physical characterization and performance evaluation of an x-ray micro-computed tomography system for dimensional metrology applications," *Meas. Sci. Technol.*, vol. 23, no. 8, p. 085404, 2012.

[109] F. Vogeler, W. Verheecke, A. Voet, and J. Kruth, "Positional stability of 2D X-ray images for computer tomography," in *International Symposium on Digital Industrial Radiology and Computed Tomography*, 2011, p. Mon. 3.3.

[110] D. Weiß, R. Lonardoni, A. Deffner, and C. Kuhn, "Geometric image distortion in flat-panel X-ray detectors and its influence on the accuracy of CT-based dimensional measurements," in *th Conference on Industrial Computed Tomography (iCT)*, 2012, pp. 173–181.

[111] J. F. Barrett and N. Keat, "Artifacts in CT: Recognition and avoidance," *RadioGraphics*, vol. 24, no. 6, pp. 1679–1691, 2004.

[112] R. Popilock, K. Sandrasagaren, L. Harris, and K. A. Kaser, "CT artifact recognition for the nuclear technologist," *J. Nucl. Med. Technol.*, vol. 36, no. 2, pp. 79–81, 2008.

[113] X. Zhang, L. Li, F. Zhang, X. Xi, L. Deng, and B. Yan, "Improving the accuracy of CT dimensional metrology by a novel beam hardening correction method," *Meas. Sci. Technol.*, vol. 26, p. 015007, 2015.

[114] Y. Tan, K. Kiekens, F. Welkenhuyzen, J. Angel, L. De Chiffre, J.-P. Kruth, and W. Dewulf, "Simulation-aided investigation of beam hardening induced errors in CT dimensional metrology," *Meas. Sci. Technol.*, vol. 25, no. 6, p. 064014, 2014.

[115] S. Kasperl, R. Schielein, F. Sukowski, P. Hornberger, and A. Gruber, "CT simulation study to demonstrate material impact using hole plates," in *11th European Conference on Non-Destructive Testing, Prague, Czech Republic.*, 2014, p. [Online]. Available:http://www.ndt.net/?id=16598.

[116] A. K. Hunter and W. D. McDavid, “Characterization and correction of cupping effect artefacts in cone beam CT,” *Dentomaxillofacial Radiol.*, vol. 41, no. 3, pp. 217–223, 2012.

[117] Y. Tan, K. Kiekens, F. Welkenhuyzen, J. Kruth, and W. Dewulf, “Beam hardening correction and its influence on the measurement accuracy and repeatability for CT dimensional metrology applications,” in *Conference on Industrial Computed Tomography*, 2012, pp. 355–362.

[118] W. Dewulf, Y. Tan, and K. Kiekens, “Sense and non-sense of beam hardening correction in CT metrology,” *CIRP Ann. - Manuf. Technol.*, vol. 61, no. 1, pp. 495–498, 2012.

[119] J. J. Lifton, A. A. Malcolm, and J. W. McBride, “An experimental study on the influence of scatter and beam hardening in x-ray CT for dimensional metrology,” *Meas. Sci. Technol.*, vol. 27, no. 1, p. 015007, 2016.

[120] M. Krumm, S. Kasperl, and M. Franz, “Referenceless beam hardening correction in 3D computed tomography images of multi-material objects,” in *17th World Conference on Non-destructive Testing*, 2008, pp. 25–28.

[121] M. Kachelrieß, K. Sourbelle, and W. A. Kalender, “Empirical cupping correction: A first-order raw data precorrection for cone-beam computed tomography,” *Med. Phys.*, vol. 33, no. 5, pp. 1269–1274, 2006.

[122] L. Brabant, E. Pauwels, M. Dierick, D. Van Loo, M. A. Boone, and L. Van Hoorebeke, “A novel beam hardening correction method requiring no prior knowledge, incorporated in an iterative reconstruction algorithm,” *NDT E Int.*, vol. 51, pp. 68–73, 2012.

[123] P. Müller, J. Hiller, A. Cantatore, M. Bartscher, and L. De Chiffre, “Investigation on the influence of image quality in x-ray CT metrology,” in *Conference on Industrial Computed Tomography (ICT)*, 2012, pp. 229–238.

[124] M. Bartscher, M. Neukamm, U. Hilpert, U. Neuschaefer-Rube, F. Härtig, K. Kniel, K. Ehrig, A. Staude, and J. Goebbels, “Achieving traceability of industrial

computed tomography," *Key Eng. Mater.*, vol. 437, pp. 79–83, 2010.

[125] J. Hiller and L. M. Reindl, "A computer simulation platform for the estimation of measurement uncertainties in dimensional X-ray computed tomography," *Meas. J. Int. Meas. Confed.*, vol. 45, no. 8, pp. 2166–2182, 2012.

[126] U. Hilpert, M. Bartscher, and M. Neugebauer, "Simulation-aided computed tomography (CT) for dimensional measurements," in *International Symposium on Digital Industrial Radiology and Computed Tomography*, 2007, p. [Online]. Available: http://www.ndt.net/?id=4911.

[127] R. Schmitt and C. Niggemann, "Uncertainty in measurement for x-ray-computed tomography using calibrated work pieces," *Meas. Sci. Technol.*, vol. 21, no. 5, p. 054008, 2010.

[128] P. Muller, J. Hiller, Y. Dai, J. L. Andreasen, H. N. Hansen, and L. De Chiffre, "Estimation of measurement uncertainties in X-ray computed tomography metrology using the substitution method," *CIRP J. Manuf. Sci. Technol.*, vol. 7, no. 3, pp. 222–232, 2014.

[129] J. Angel and L. De Chiffre, "Comparison on computed tomography using industrial items," *CIRP Ann. - Manuf. Technol.*, vol. 63, no. 1, pp. 473–476, 2014.

[130] K. Kiekens, F. Welkenhuyzen, Y. Tan, P. Bleys, A. Voet, J.-P. Kruth, and W. Dewulf, "A test object with parallel grooves for calibration and accuracy assessment of industrial computed tomography (CT) metrology," *Meas. Sci. Technol.*, vol. 22, no. 11, p. 115502, 2011.

[131] M. Bartscher, M. Neukamm, M. Koch, U. Neuschaefer-Rube, A. Staude, J. Goebbels, K. Ehrig, C. Kuhn, A. Deffner, and A. Knoch, "Performance assessment of geometry measurements with micro-CT using a dismountable work-piece-near reference standard," in *10th European Conference on Non-Destructive Testing*, 2010, p. [Online]. Available: http://www.ndt.net/?id=9218.

[132] S. Carmignato, "Accuracy of industrial computed tomography measurements: Experimental results from an international comparison," *CIRP Ann. - Manuf.*

Technol., vol. 61, no. 1, pp. 491–494, 2012.

[133] H. Lettenbauer, B. Georgi, and D. Weiß, “Means to verify the accuracy of CT systems for metrology applications (in the absence of established international standards),” in *International Symposium on Digital Industrial Radiology and Computed Tomography*, 2007, p. [Online]. Available: http://www.ndt.net/?id=4913.

[134] ISO, *ISO/CD 10360-11 Geometrical product specifications (GPS) -- Acceptance and reverification tests for coordinate measuring machines (CMM) -- Part 11: CMMs using the principle of computed tomography (CT)*. International Organization for Standardization.

[135] F. Léonard, S. B. Brown, P. J. Withers, P. M. Mummery, and M. B. McCarthy, “A new method of performance verification for x-ray computed tomography measurements,” *Meas. Sci. Technol.*, vol. 25, no. 6, p. 065401, 2014.

[136] Baker Hughes, “GE Scatter|Correct,” 2020. [Online]. Available: https://www.bakerhughesds.com/inspection-technologies/radiography-ct/x-ray-computed-tomography/scattercorrect. [Accessed: 11-Apr-2020].

[137] Nikon Metrology, “XT H 450,” 2018. [Online]. Available: https://www.nikonmetrology.com/en-gb/product/xt-h-450. [Accessed: 08-Sep-2018].

[138] “aRTist-analytical RT inspection simulation tool.” BAM, 2007.

[139] N. Flay, “An investigation of the factors associated with the x-ray tube and their influence on dimensional measurement in micro-focus cane-beam industrial x-ray computed tomography systems,” University of Southampton, Southampton, [Doctoral Thesis], 2016.

[140] N. Wiener, *Extrapolation, interpolation, and smoothing of stationary time series*. MIT Press Cambridge, 1949.